Magnetic Core-Shell Silica Colloids

Universiteit Utrecht

ISBN 978-90-393-4559-7

Subject headings: Colloids/silica/magnetic particles/composite particles/complex magnetic susceptibility/magnetization measurements/catalyst support/core-shell particles.

Cover: Scanning electron microscopy pictures of silica spheres covered with magnetic nanoparticles.

Magnetic Core-Shell Silica Colloids

Magnetische Kern-Schil Silica Colloïden

(met een samenvatting in het Nederlands)

Proefschrift

ter verkrijging van de graad van doctor aan de
Universiteit Utrecht op gezag van de rector magnificus,
prof. dr. W.H. Gispen, ingevolge het besluit van het
college voor promoties in het openbaar te verdedigen
op 11 juni 2007 des morgens te 10.30 uur

door

Eva Maria Claesson

geboren op 3 januari 1978 te Mölndal, Zweden

Promotor: Prof. dr. A.P. Philipse

Co-promotor: Dr. B.H. Erné

Dit proefschrift werd (mede) mogelijk gemaakt met financiële steun van OCÉ Technologies, Venlo, The Netherlands.

Ingenting är omöjligt, bara olika svårt

(Gunde Svan)

Contents

1

General Introduction

1.1. Colloids

Colloids are particles with at least one dimension in the size range 1-1000 nm. Just like atoms and molecules, colloidal particles diffuse due to thermal motion. For colloids such diffusive displacement is usually referred to as 'Brownian motion'. For the fundamental study of phenomena such as gas-liquid-crystal phase transitions, 'colloidal atoms' constitute an important model system [1, 2]. Compared to the much smaller atoms, colloids have the advantage of diffusing orders of magnitude slower and being observable on a single-particle level using electron or light microscopy. Moreover, colloidal particles with various sizes, shapes and chemical properties [3–5] can be synthesized, and their interactions can be tuned, for instance by variation of solvent composition or by controlled addition of salt or non-adsorbing polymers. Studies of nearly monodisperse colloidal systems provide new insight into the effects of interactions and parameters such as particle shape and size on the macroscopic behaviour of a dispersion, including stability, phase separation and rheology.

In fundamental studies as well as commercial applications of colloids, it is desirable to control the stability of colloidal dispersions. To prevent single particles from aggregating, attractive forces must be counteracted by repulsive forces, a topic explained in more detail in any textbook on colloids [6, 7]. Attractive forces are for instance the van der Waals interactions, also known as London or dispersion forces, which arise from coupled fluctuations of instantaneous atomic dipoles. The strength of the van der Waals forces between colloidal particles increases with the difference in refractive index between the particles and the surrounding medium. Therefore, one way of diminishing these attractive forces is optical matching, *i.e.*, choosing a solvent with a refractive index close to

that of the particles. Magnetic particles experience attractive dipole-dipole interactions that can lead to formation of anisotropic, chain-like aggregates [8, 9]. Repulsive forces can be due to an electrical double-layer repulsion between charged particles, provided that their charges have equal signs. Charges on a surface will attract oppositely charged ions (counter-ions) from the surroundings, creating an electrostatic diffuse double layer that screens the surface charge of the colloids. The characteristic distance from the particle at which the repulsion is screened by the counter-ions is often referred to as the Debye screening length, κ^{-1}. By controlled addition of salt, the Debye length in a system can be gradually decreased to minimize the effect of repulsion. Another way to stabilize colloidal dispersions is by adsorption or covalent bonding of polymers to the particle surface. When the polymer chains start to overlap, they cause steric repulsion between the colloidal particles.

This thesis focuses mainly on one particular type of colloids, namely magnetic core-shell silica colloids. The silica in such composite particles can for instance be optically matched with common solvents or labelled with a fluorescent dye. In combination with their anisotropic interactions, they provide a colloidal model system for interactions between dipoles in a dipolar fluid. Magnetic colloids also have many technological applications as described in more detail in section 1.3.

1.2. Magnetic colloids

The mineral magnetite (Fe_3O_4) is a typical example of a ferromagnetic material. Strong, long-range coupling between its atomic dipoles leads to permanently magnetic domains within the material, with all atomic dipoles oriented in the same direction. When the direction of the magnetization of such domains is random, the net magnetization is zero for a large material volume. Other examples of ferromagnetic materials are iron, nickel, cobalt and some of their alloys [10]. Some other materials, such as aluminium and oxygen, are so-called paramagnetic, which means that they have permanent atomic dipoles due to unpaired electrons which can only be aligned in a strong magnetic field, inducing a weak magnetization of the material.

When a ferromagnetic material is divided into nanoparticles, smaller than the magnetic domains in the bulk material (on the order of 30 nm for iron oxides), these nanoparticles have a single domain and hence, a permanent dipole moment. In the 1960's, Papell and co-workers [11] succeeded in grinding magnetite into very fine, single domain particles ($\sim$ 10 nm). They also managed to obtain a stable colloidal dispersion of these particles in kerosene by coating them with oleic acid [10,12]. This was one of the first so-called ferrofluids, *i.e.*, stable dispersions of magnetic nanoparticles. Since then, colloids of other magnetic substances have been developed and synthesis methods have been improved to yield lower polydispersity and better control of the average particle size [9, 13–19]. Magnetic single-domain particles in dispersion are sometimes referred

to as superparamagnetic, since the particles themselves have a permanent magnetic moment, but the net magnetization of the ferrofluid is zero due to the random orientation of the individual particle dipole moments, similar to the situation in paramagnetic substances. However, in an external magnetic field, alignment of these dipole moments will cause a net magnetization of the sample which is several orders of magnitude higher than for paramagnetic substances.

The properties of magnetic particles depend on their crystalline structure. Metallic iron and cobalt, for instance, have a high saturation magnetization per unit volume. However, a serious drawback of these materials, in particular when dispersed as nanoparticles, is that they oxidize to non-magnetic oxides almost instantaneously when exposed to air. Certain iron and cobalt oxides, such as maghemite ($\gamma - Fe_2O_3$) and cobalt ferrite ($CoFe_2O_4$), have a lower saturation magnetization, but the advantage is that they are already in their most oxidized state. This makes synthesis and characterization as well as further experimental studies practically easier.

The saturation magnetization in a dispersion of magnetic particles is reached when the external magnetic field is strong enough to align all individual particle magnetic dipoles (see Figure 1.1). An important feature of magnetic particles is how the orientation of the dipoles relaxes after the magnetic field has been turned off. As illustrated in Figure 1.1, there are two possible mechanisms for this relaxation: either via free dipole rotation within the particle, so-called Néel relaxation, or via thermal rotation of the entire particle in the solvent, also known as Brownian rotation. The relaxation times for these mechanisms, τ_N and τ_B respectively, are given by:

$$\tau_N = \frac{1}{f_0} exp\left[\frac{KV_m}{k_BT}\right] \tag{1.1}$$

and

$$\tau_B = \frac{3V_h\eta_0}{k_BT}, \tag{1.2}$$

where f_0 is the so-called Larmor frequency ($\sim 10^9\ s^{-1}$), K the anisotropy constant of the particle material, k_BT the thermal energy and η_0 is the viscosity of the solvent. V_m and V_h are respectively the magnetic and the hydrodynamic volume of the particle. Consequently, for particles with a large anisotropy constant (such as cobalt ferrite, $CoFe_2O_4$) and a sufficiently large volume, the dipole moment can be regarded as thermally blocked inside the nanoparticles. Magnetic materials such as magnetite (Fe_3O_4) and maghemite ($\gamma - Fe_2O_3$) have a much lower anisotropy constant and the relaxation of dipole moments is usually dominated by Néel relaxation.

At the Van't Hoff laboratory in Utrecht, research on magnetic colloids started with magnetite ferrofluids and synthesis of silica spheres with encapsulated magnetite nanoparticles [20]. Subsequent studies were performed on for instance dipolar interactions [21]

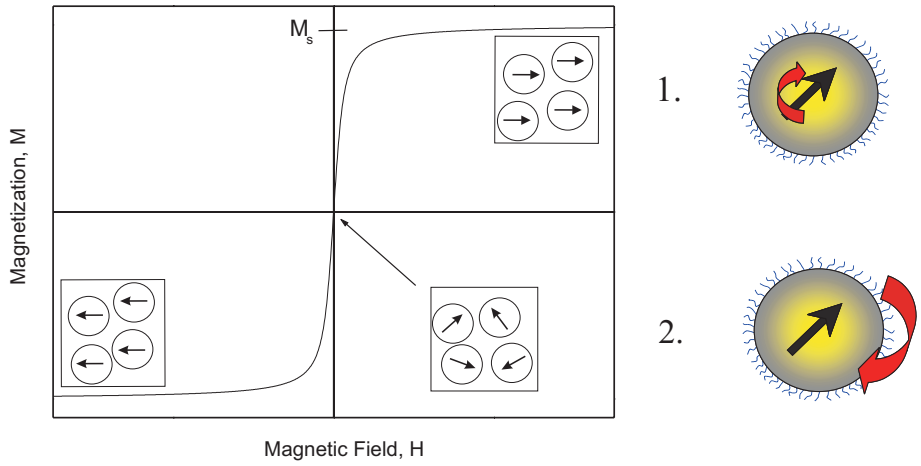

Figure 1.1. Left: Sketch of the magnetization curve ($M(H)$) of superparamagnetic particles in dispersion. The saturation magnetization, M_s, is reached when the applied magnetic field is strong enough to align all individual particle dipoles with the field. After the magnetic field has been turned off, the dipoles will again be randomly oriented, and there is no net magnetization. Right: The re-orientation of dipoles occurs either via rotation within the particle, so-called Néel relaxation (1) or via thermal rotation of the entire particle, so-called Brownian rotation (2).

and phase behaviour, the latter in particular in the presence of non-adsorbing polymer [22, 23]. Later, the palette of magnetic colloids was extended to metallic cobalt [24, 25] and iron [14, 26]. Valuable results have been obtained with these colloids, such as the first *in situ* observation of spontaneous dipolar chain formation in zero field [8]. However, further optimisation and control of particle properties is desirable. For example, iron and cobalt particles are susceptible to oxidation and the shape, size and magnetic moment of the nanoparticles are often very polydisperse.

Several strategies have been adopted in our laboratory to obtain improved magnetic model colloids. One is the development of monodisperse magnetic nanoparticles via thermolysis of organometallic precursors in high-boiling organic solvents [9, 27]. Another route, presented in this thesis, is the preparation of monodisperse silica spheres with a shell of magnetic nanoparticles. The motivation for developing such composite particles is that the silica cores can be prepared with a low polydispersity using well-known synthesis methods and that the amount of magnetic material per particle remains limited in a way that optical techniques, including confocal laser microscopy, can be used to study the particles.

1.3. Applications of magnetic colloids

Magnetic colloids can be manipulated with an external field, a feature that is not only of interest for fundamental studies, but that is also important for many industrial and biomedical applications [28–30], a few examples of which are discussed below.

Functionalised magnetic colloids can serve as carrier particles for transport of, among other things, molecules, cells and drugs, by means of an applied magnetic field gradient [28]. The magnetic force acting on a magnetic particle is proportional to the magnetic field gradient and the net particle dipole moment. Consequently, for magnetic carrier particles, a large induced or permanent dipole moment is needed for rapid transport in an external magnetic field.

One example of a commercial application of magnetic colloids is the use of magnetic toners in the Direct Imaging Printing (DIP) technique applied by printer manufacturer Océ [31,32]. The toner particles used in this technique are both charged and magnetic. During the printing process, toner particles are transported from the toner reservoir by a magnetic force. A digital image is converted to a voltage pattern on an imaging unit, to which the toner particles are attracted when the electrical force exceeds the magnetic force acting on the toner particle. In this way a toner image is created directly from a digital image. The toner image is subsequently transferred from the imaging unit onto the receiving medium (usually paper). To meet the requirements of this printing technique, toner particles are made with embedded magnetic particles with a high saturation magnetization and low remanence. The toner particles are also supplied with a surface coating of a conductive doped metal oxide. Moreover, for colour toners, light absorption of the magnetic particles must be reduced. This is achieved by the use of fluorescent dye mixtures.

Another possible application is the use of magnetic composites particles in catalysis [26, 33]. Colloidal particles with magnetic properties can be used as supports for catalytic molecules to combine the efficiency of homogeneous catalysts (catalyst homogeneously mixed with the reactants) and the convenient recycling of heterogeneous catalysts (catalyst on a solid support). A demonstration of this application is given in Chapter 4 of this thesis, where magnetic particles are coated with a PCP-pincer palladium complex and used in an aldol condensation reaction. The large induced dipole moment in these magnetic silica particles allows for manual magnetic separation with a small magnet.

Other possible applications receiving much attention involve the use of magnetic colloids in medical diagnostics and treatments. There is a trend towards more local treatment of diseases in the body with more target-specific delivery of drugs [34]. If the drug is tethered to a magnetic carrier particle, it can be guided with a magnet, in order to concentrate the drug near the target, which can be for instance a blood

clot [35] or a tumour [36, 37]. This minimizes the amount of drug released where it is not needed, which means that the total dosage can be reduced and less of the healthy tissue is affected, thereby limiting the side effects.

The assisted translation of particles with an external, inhomogeneous magnetic field is not the only useful property of magnetic colloids. Magnetic particles, in particular particles with a high crystalline anisotropy, are heated up when exposed to a high-frequency alternating magnetic field [38]. Consequently, via magnetic particles magnetic work can be converted into heat. By using magnetic particles with affinity for certain cancer cells, these cells can be heated selectively by an external alternating magnetic field upon which the cancer cells die (so-called hyperthermia) whereas the healthy cells, not containing magnetic particles, are not affected [39, 40]. With such target-specific heating, well-known side effects of chemotherapy such as loss of hair can be avoided. The same principle of "magnetic heating" can be employed as a trigger to release drugs from an implant. The drug can then be contained in a thermo-responsive polymer, which releases the drug-molecules upon increasing the temperature [41] applying an external AC magnetic field.

The realization of these applications requires, among other things, the development of new magnetic composite colloids. Such particles should have a low polydispersity since many of the physical properties depend on particle size. A broad size distribution could for instance in magnetic hyperthermia lead to less effective heating because the frequency at which the most efficient heating occurs is a strong function of particle size (see (1.1) and (1.2)) [38]. Furthermore, knowledge of the colloidal stability of the particles both in and outside the human body is essential to avoid unwanted effects due to cluster formation. For biomedical applications, the particles must also be bio-compatible and functionalised with target-specific surface groups.

1.4. Magnetic silica composite colloids

The research in this thesis is focussed on the synthesis and characterization of magnetic silica composite particles, prepared by covering the surface of colloidal silica spheres with magnetic nanoparticles from aqueous ferrofluids of maghemite [42–44] and cobalt ferrite [45]. Via functionalization of the silica spheres with thiol-groups, the magnetic particles are chemically bound to the surface and the resulting core-shell particles can be coated with an outer silica shell (see Chapter 2) [46]. The use of silica has several advantages:

- The synthesis as well as physical and chemical properties of colloidal silica are well-documented (see references in Chapter 2).
- The size of the silica cores can easily be controlled during their synthesis.
- Fluorescent dyes can be incorporated via covalent bonds in the silica structure [47].
- Silica is chemically stable in most solvents and can be exposed to high temperatures.

• The refractive index of silica can be well matched with that of many common solvents, which reduces van der Waals forces and facilitates imaging with confocal microscopy.
• The surface chemistry of silica allows covalent attachment of a wide spectrum of chemical functionalities via so-called silane coupling agents, which is important for applications as carrier particles (see section 1.3) as well as for dispersing the particles in apolar solvents [48].

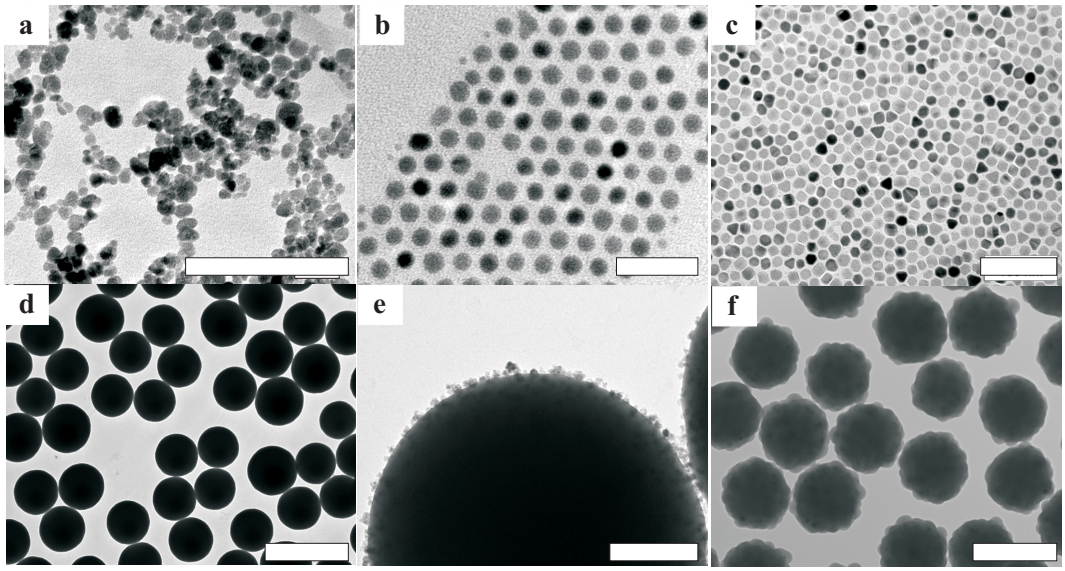

Figure 1.2. TEM pictures of a) cobalt ferrite particles from an aqueous ferrofluid prepared in a coprecipitation step (scale bar: 50 nm), b) surfactant stabilized cobalt particles from thermal decomposition of $Co_2(CO)_8$ [15, 49] (scale bar: 50 nm), c) surfactant stabilized magnetite particles [9] (scale bar: 100 nm), d) Stöber-silica (scale bar: 1 μm), e) cobalt ferrite particles attached to the surface of Stöber-silica [50] (see Chapter 2 of this thesis) (scale bar: 200 nm) and f) the silica-cobalt ferrite particles coated with silica (see Chapter 2) (scale bar: 500 nm).

Aqueous dispersions of cobalt ferrite and maghemite were synthesized by coprecipitation of iron and cobalt chloride salts in an alkaline solution, yielding particles with a radius typically in the range of 5-10 nm. In Figure 1.2 a, a transmission electron microscopy (TEM) picture of a typical cobalt ferrite powder is shown, illustrating the polydispersity and irregular particle shape characteristic for particles prepared by coprecipitation. Other methods of preparing ferrofluids of, for instance, magnetite or metallic cobalt (see Figure 1.2 b) yield particles with a much better defined size and shape. These are usually synthesized via thermal decomposition of organometallic precursors in the presence of a surfactant in high boiling solvents. However, the presence of surfactant on the particle surface obstructs transfer to polar solvents and chemical bonding to other inorganic surfaces. Therefore, the choice was made to use particles

prepared in aqueous medium with the coprecipitation method to cover much larger monodisperse silica cores.

1.5. Outline of this thesis

The outline of this thesis is as follows: **Chapter 2** describes the synthesis of magnetic maghemite and cobalt ferrite nanoparticles that are subsequently attached to thiol-functionalised silica particles and encapsulated in an outer silica shell of variable thickness. The magnetic interactions between the resulting magnetic core-shell colloids are discussed based on magnetization measurements and electron microscopy pictures made of these particles dried before, after and during exposure to a homogeneous magnetic field. Furthermore, images are presented of magnetic core-shell colloids with larger, fluorescent silica cores, made *in situ* using a confocal microscope in a homogeneous magnetic field. In **Chapter 3**, the thiol-functionalization approach is extended to other types of silica, such as commercially available silica nanoparticles and porous silica grains. As a probe for the presence of thiol surface groups and also to demonstrate how other metallic nanoparticles can be chemically attached to silica surfaces as well via thiol-groups, gold particles were used instead of magnetic oxides. In **Chapter 4** it is demonstrated how silica-maghemite with catalyst molecules anchored to the silica surface can be employed as a heterogeneous catalyst. Due to the small size of the magnetic particles and their large surface-to-volume ratio, the catalyst can be homogeneously dispersed for efficient catalysis; the large induced magnetic moment enables recycling of the catalyst after use. An extensive analysis of the magnetic properties of the composite particles from Chapter 2 is presented in **Chapter 5**, including direct measurements of the particle dipole moment in zero field before and after treatment in a saturating magnetic field using complex magnetic susceptibility spectroscopy. The same experimental technique is used in **Chapter 6** to investigate the rotational diffusion coefficient as a function of volume fraction for silica particles with a permanent dipole moment. Here we exploit the possibility to vary the zero-field magnetic dipole moment and, consequently, the magnetic attractive interactions in the system, keeping all other parameters constant. In **Chapter 7**, results are presented of static light scattering measurements on the magnetic core-shell particles described in this thesis. The applicability of the theory for contrast variation in the Rayleigh-Gans-Debye approximation is explored with the aim to obtain the particle radius and average refractive index.

2

Monodisperse Magnetizable Composite Silica Spheres with Tunable Dipolar Interactions

Abstract

We demonstrate that magnetic particles of maghemite ($\gamma - Fe_2O_3$) and cobalt ferrite ($CoFe_2O_4$) can be irreversibly attached to (fluorescent) colloidal silica grafted with 3-mercaptopropyl(trimethoxy)silane, followed by the controlled growth of a silica layer, to obtain stable dispersions of monodisperse colloidal silica spheres that contain a shell of ferrite particles at an adjustable distance from the sphere surface. Magnetization of the ferrite shell induces a large dipole moment and adjusting the thickness of the outer silica layer enables one to tune the contact interaction. This novel type of magnetizable silica colloids exhibits structure formation in a homogeneous field that varies from isotropic distributions to elongated dipolar chains as observed with TEM and confocal microscopy.

2.1. Introduction

Magnetic particles can be used as colloidal model systems for studying dipole-dipole interactions and should, ideally, consist of monodisperse particles with adjustable dipole moments. Dispersions of magnetic colloids of various ferrites prepared with a classic coprecipitation method [42, 43, 45] contain particles in the size range of 10-20 nm with a significant polydispersity both in size and in shape. Moreover, controlling the size during the coprecipitation is nearly impossible by this approach, although size fractionation can be carried out on the synthesized dispersion to decrease the polydispersity [44, 51, 52]. With recently developed synthesis methods [19], ferrite particles with a low polydispersity can be obtained with size control up to a diameter of 21 nm [9]. Coating single magnetic particles with a magnetic layer of silica enables one to tune the dipole-dipole interactions by controlling the thickness of the silica shell and thereby the distance of closest approach between the magnetic cores [20]. A drawback of this system is the inherently weak magnetic interaction due to the small magnetic core volume: the decay of the dipole-dipole interaction potential between single magnetic particles is such that even a silica shell of only a few nanometres screens these interactions, as further discussed in section 2.2.

Here we report on the synthesis of well-defined, monodisperse magnetic silica composite particles in the colloidal size range, with a large induced dipole moment, such that the presence of a silica layer, in contrast to the particles described in the work of Philipse *et al.* [20], still allows substantial magnetic attractions between the cores at contact. The well-known chemistry of silica makes it possible to incorporate fluorescent dye [47] and to modify the particle surface with functional groups [48, 53]. Thus the single-particle magnetic core in reference [20] is replaced by a magnetic composite particle consisting of many single-domain magnetic particles that are irreversibly attached to the surface of a silica core. When a homogeneous magnetic field is applied, a large magnetic dipole moment is induced in such composites, as the dipole moments of the individual magnetic particles align with the field. The size of the silica core can easily be varied, which enables one to tune the maximum strength of the magnetic dipole moment and varying the silica shell thickness allows tuning the dipole-dipole interactions at particle contact.

With this possibility in mind, particles of hard magnetic cobalt ferrite ($CoFe_2O_4$) and soft magnetic maghemite ($\gamma - Fe_2O_3$) were adsorbed onto monodisperse cores of colloidal silica and encapsulated in an outer silica shell. The synthesis of the silica cores as well as the growth of an outer silica layer were carried out using the well-known Stöber method [50, 54] in alkaline mixtures of ethanol and water. For the final silica deposition step, it is therefore crucial that the silica-ferrite composite particles are stable under these conditions. Composites consisting of small magnetic particles adsorbed onto large

spherical non-magnetic colloids have previously been achieved by mixing dispersions of oppositely charged particles [55,56]. However, using this method we observed desorption of magnetic particles in a wide range of pH, which would obstruct the formation of uniform silica-ferrite spheres with an outer layer of amorphous silica.

To avoid the desorption of magnetic particles during the growth of a silica shell, the magnetic particles were attached to the silica surface via a silane coupling agent: a molecule with the general formula $R_nSiX_{(4-n)}$ that contains hydrolyzable groups, X, which can react with the surface of the silica particle and one non-hydrolyzable group, R. This non-hydrolyzable group should contain a functional group that can bind to the surface of the maghemite and cobalt ferrite particles to link them to the silica surface. One possibility in this case is a thiol group. Thiols are known for their high affinity for metals [57, 58] and thiol-functionalized organic molecules have previously been used to bind cadmium sulfide particles [59,60] and heavy metal ions [61] to inorganic substrates but, to our knowledge, they have not yet been applied to ferrite particles. We therefore investigated whether the thiol-functionalized silane coupling agent 3-mercaptopropyl(trimethoxy)silane (MPTMS) could be used to bind maghemite and cobalt ferrite covalently to the surface of silica particles.

The size, polydispersity and internal morphology of the synthesized composite particles were studied using scanning (SEM) and transmission (TEM) electron microscopy. The size and polydispersity of the silica cores were obtained with static light scattering (SLS) and TEM. The magnetic radii of the magnetite and cobalt ferrite particles were obtained from magnetization measurements as well as TEM. The influence of the silica shell thickness on the magnitude of the dipolar contact attraction was studied by imaging the structure formation of silica-ferrite spheres in a homogeneous magnetic field.

2.2. Interaction model

First a simple model is introduced to estimate the magnetic dipole-dipole interaction between two silica spheres with embedded magnetic particles. We consider two single magnetic particles with a magnetic radius, a_m, embedded inside silica spheres at a centre-to-centre distance, $r = 2(a_m + \Delta)$ (see Figure 2.1B). Here 2Δ is the surface-to-surface distance between the magnetic cores of two particles at contact, such that Δ equals the thickness of the silica shell around the magnetic particles. Assuming two equal dipole moments, μ_{mp}, that are aligned in the head-to-tail configuration, the interaction energy, $u(r)$, in units of k_BT can be written as:

$$\frac{u(r)}{k_BT} = -2\frac{\lambda_r}{r^3} \qquad r \geq 2a_m \tag{2.1}$$

with the r being the centre-to-centre distance. The interaction parameter λ_r is a function of the magnetic moment of one magnetic particle:

$$\lambda_r = \frac{\mu_0 \mu_{mp}^2}{4\pi k_B T} = \frac{4}{9}\frac{\mu_0 m_s^2 \pi}{k_B T} a_m^6 \tag{2.2}$$

in which a_m is calculated from magnetization curves via:

$$a_m = \sqrt[3]{(\frac{\chi_i}{M_s}\frac{9k_B T}{4\pi\mu_0 m_s})} \tag{2.3}$$

Here, χ_i is the initial susceptibility, M_s the measured saturation magnetization, and $\mu_0 = 4\pi \times 10^{-7}\ JA^{-2}m^{-1}$ is the vacuum permeability. The bulk saturation magnetization per volume, m_s, is a material constant, which at T= 298.15 K is 414 kA/m for maghemite and 425 kA/m for cobalt ferrite [10]. Here, the bulk value for maghemite and cobalt ferrite respectively is used for the magnetic particles. However, the saturation magnetization of the magnetic particles will be lowered because of pinning of the spins at the particle surface. Consequently, using the bulk saturation magnetization results in a slightly overestimated magnetic radius. The dipole moment of one spherical magnetic particle can be written as:

$$\mu_{mp} = \frac{4\pi a_m^3}{3} m_s = \frac{3k_B T}{\mu_0}\frac{\chi_i}{M_s} \tag{2.4}$$

In Figure 2.1A, the interaction potential from Eq. 2.1 is shown as a function of Δ, using experimental values for the a_m of cobalt ferrite (a_m= 8.4 nm) and maghemite (a_m =5.8 nm) particles, which were prepared with classic coprecipitation methods [42, 43, 45]. Figure 2.1A shows that the dipole-dipole interaction between two single magnetic particles prepared with this method will in general not be strong enough to allow for the formation of dipolar chains for values of Δ larger than 2 nm for maghemite or 6 nm for cobalt ferrite ($-u < 2\ k_B T$). As a consequence, the thickness of a silica layer around these single ferrite particles should not be larger than a few nanometres to avoid total screening of the dipolar interactions. Such a thin silica layer, however, is experimentally difficult to obtain.

For composite particles, as shown in Figure 2.1B, the interaction energy depends on the number of magnetic particles, N, adsorbed per silica sphere. Assuming that the total magnetic moment of a composite particle, μ_{cp}, in a saturating magnetic field, is the sum of all individual magnetic moments ($\mu_{cp} = N\mu_{mp}$) the interaction energy $U(r)$ between two composite particles can be estimated from:

$$\frac{U(r)}{k_B T} = N^2 \frac{u(r)}{k_B T} \qquad r \geq 2(R + 2a_m), \tag{2.5}$$

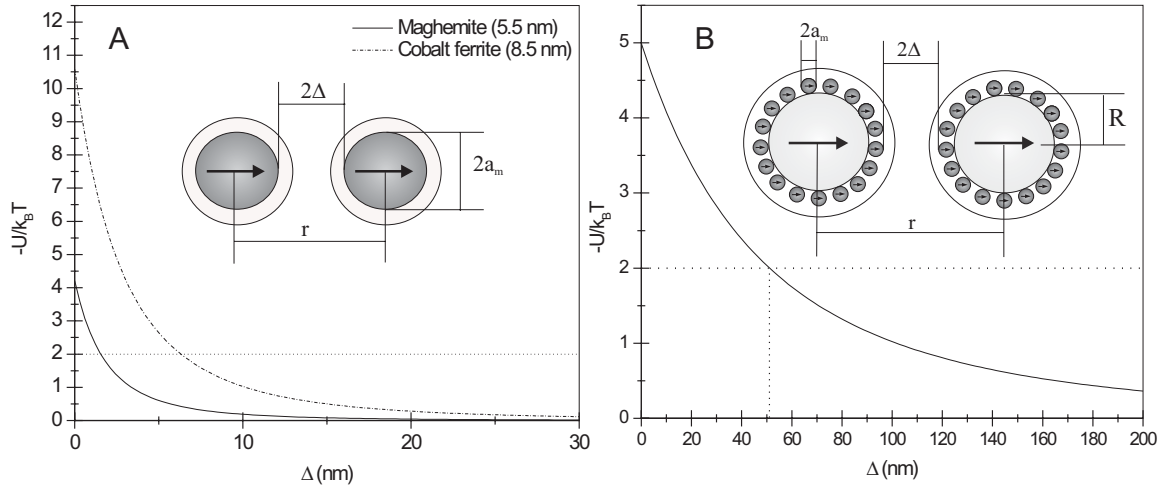

Figure 2.1. Interaction potentials for two single magnetic particles of cobalt ferrite and of maghemite (A) and two composite particles with cobalt ferrite (B) as a function of Δ when all dipoles are aligned in the head-to-tail configuration.

with the centre-to-centre distance now given by:

$$r = 2(R + 2a_m + \Delta) \tag{2.6}$$

In Figure 2.1 B, the interaction potential is shown as a function of Δ for silica cores with a radius of $R = 135$ nm with 50 adsorbed cobalt ferrite particles for which a_m= 8.4 nm. Figure 2.1 predicts that the silica layer can be made considerably thicker around composite particles (provided that N is large enough) than around single ferrite particles while still allowing the formation of dipolar chains. Although Eqs. 2.1 and 2.5 apply to a pair of spherical dipoles, they also provide a reasonable estimate of the interaction between one dipolar sphere and a chain of dipolar spheres. In the latter case, the attraction between the dipole and the chain at contact will be somewhat larger, although not more than 20 % of the attraction between two dipolar spheres [62].

2.3. Experimental section

Materials

The following chemicals were used as received: tetraethoxysilane (TEOS, Merck), ethanol (Merck), ammonia solution (Merck), iron(II) chloride tetrahydrate (Fluka), iron(III) chloride hexahydrate(Fluka), nitric acid (65%, Merck), iron(III) nitrate nonahydrate (Merck), cobalt(II) chloride hexahydrate (Fluka), sodium hydroxide pellets

(Acros), 3-mercaptopropyl(trimethoxy)silane (MPTMS, Fluka) and aqueous tetramethylammonium hydroxide (TMAH) solution, (25%, Aldrich). Only demineralized water was used.

Synthesis of silica dispersions

Dispersions of silica particles were prepared according to the Stöber method [50,54], by the hydrolysis and condensation polymerisation of TEOS in a mixture of ethanol, water and ammonia. Glassware for the Stöber synthesis was carefully cleaned with detergent, rinsed extensively with demineralized water and dried prior to use. Distilled TEOS (75 mL) was added rapidly to a mixture of 1770 mL distilled ethanol and 152 mL ammonia (25%) under the liquid surface via a funnel while the mixture was stirred vigorously. After a few minutes, the mixture became turbid white, indicating the formation of silica particles. The dispersion was labelled SiA. Two other silica dispersions (SiB and SiC), were previously prepared in the same way, but with different ammonia concentrations. The particle size and polydispersity were obtained with TEM and SLS.

Synthesis of maghemite particles

Magnetite (Fe_3O_4) particles were prepared in a coprecipitation step based on the procedure of Massart *et al.* [23,42,43], followed by the subsequent oxidation to maghemite ($\gamma - Fe_2O_3$). Iron chloride salts ($FeCl_2 \cdot 4H_2O$, 3.29 g and $FeCl_3 \cdot 6H_2O$, 8.68 g) were dissolved in 380 mL water. Next, 25 mL of ammonia solution (25%) was added rapidly to the iron chloride solution under vigorous stirring upon which a black precipitate was formed. This black precipitate was collected with a permanent magnet under the reaction flask and the supernatant was decanted. The sediment was redispersed in 40 mL of 2.0 M HNO_3. The magnetite particles were thereafter oxidized to maghemite by adding 60 mL of 0.35 M $Fe(NO_3)_3 \cdot 9H_2O$ and letting the mixture reflux for 1 h. After being cooled to room temperature, the maghemite particles were sedimented on a magnet and rinsed twice with 100 mL of 2.0 M HNO_3 before redispersing them in 80 mL of water. The dispersion was labelled FFM3.

Synthesis of cobalt ferrite particles

Cobalt ferrite ($CoFe_2O_4$) was prepared by the coprecipitation of iron chloride salts and cobalt chloride salts according to the procedure developed by Tourinho *et al.* [45] with some modifications [63]. First, 2.38 g (0.01 mol) $CoCl_2 \cdot 6H_2O$ was dissolved in a solution of 1 mL of HCl (37%) in 4 mL of water and 5.406 g (0.02 mol) $FeCl_3 \cdot 6H_2O$ was dissolved in 40 mL of water. Second, the two separate solutions were both heated to 50 °C and thereafter mixed before being quickly added to 200 mL of boiling 1.0 M NaOH under vigorous stirring, upon which a black precipitate was formed instantly, indicating the formation of cobalt ferrite particles. In the method of Tourinho *et al.* [45], the boiling NaOH-solution is poured into a boiling solution of the two metal salts, which

prolongs the addition time (leading to a broader particle size distribution) and is less safe to handle. The reaction mixture was stirred for 30 minutes at 100 °C before being cooled to room temperature. The resulting black sediment was held to the glass wall with a magnet while the clear supernatant was decanted. In this way, the sediment was rinsed four times with 100 mL of water. After redispersing the sediment in 30 mL of 2.0 M HNO_3 and stirring for 5 minutes, 30 mL of 0.35 M $Fe(NO_3)_3 \cdot 9H_2O$ was added and the mixture was refluxed for 45 minutes. Subsequently, the reaction mixture was cooled to room temperature and left to sediment on a magnet overnight. The resulting black magnetic sediment was isolated by decanting the brownish, clear supernatant. The sediment was redispersed in water and labelled CoF12. The synthesis was repeated, and the new product was labelled CoF13.

Synthesis of silica-ferrite composite particles

Electrostatic attachment. To induce attraction between negatively charged silica particles and positively charged ferrite particles, the silica particles were transferred from the Stöber mixture to an aqueous solution and the pH was adjusted with nitric acid. When very little or no ferrite was adsorbed, a white layer of sedimented silica particles with a dark layer of ferrite particles on top was observed. The adsorption of ferrite particles was also monitored with TEM. For cobalt ferrite, a maximal attraction was found at pH = 4.0-4.3, and for maghemite, although this was not studied in great detail, it was found in the range of pH = 3-4, as also observed by Smids and van Ewijk [64]. Stable dispersions of silica and ferrite particles were mixed and shaken for $\sim$ 10 minutes. After being mixed, the core-shell particles that were obtained flocculated immediately, and the sediment was rinsed with HNO_3-solutions with appropriate pH values to maintain the electrostatic attraction while the non-adsorbed ferrite particles were being removed. A serious drawback of the electrostatic adsorption method was found to be the desorption of magnetic particles from the silica surface upon changing the pH, a change that is necessary for the deposition of an outer silica layer onto the composite particles.

Chemical attachment via a silane coupling agent. To avoid the desorption of the magnetic particles, the silica particles were first grafted with the thiol-functionalized silane coupling agent, mercaptopropyl(trimethoxy)silane (MPTMS) which, as it turns out, irreversibly binds the magnetic particles to the silica surface. The methoxy groups of MPTMS are first hydrolysed in the presence of ammonia, upon which oligomers are formed, which bind to the silanol groups on the surface of the silica particles through a condensation reaction [48, 65].

The MPTMS-coated silica was prepared as follows. The silica dispersions were diluted with a factor of 1.5 with ethanol. After this, ammonia solution (29%) was added (in the case of more freshly prepared silica dispersions, no additional ammonia was

needed) together with MPTMS while the mixture was being stirred (for synthesis details, see Table 2.1). After the mixture was stirred for approximately 45 minutes, the temperature was raised to 80 °C and approximately one third of the total volume of the stable dispersion was slowly distilled at ambient pressure. After being cooled to room temperature, the particles were washed twice by sedimentation and redispersion in ethanol to remove any unreacted MPTMS. The silica particles were sedimented at 1500 rpm (513 g) using a bench-top centrifuge. Thereafter the particles were transferred from ethanol to water by the same procedure, redispersing the sediment three times in water. The MPTMS-coated silica particles form stable dispersions in ethanol as well as in water. Ferrofluid of either maghemite or cobalt ferrite was added to the aqueous dispersion of MPTMS-coated silica particles, and the mixture was gently shaken for ~ 1 hour with an orbital shaker and subsequently left to settle without centrifugation. After addition of cobalt ferrite to the first silica dispersion (SiM1) the sample was divided into two parts. One half was stirred for 5 minutes and the other half was stirred for several hours before purifying the mixtures from free cobalt ferrite. The sediments of composite particles that were formed were washed several times with water to remove non-adsorbed maghemite or cobalt ferrite. The composite particles that were prepared in this way were dispersed in a mixture of ethanol and ammonia and ultrasonicated for 30 minutes to verify whether the magnetic particles would desorb or not under these conditions, which were similar to the conditions under which a silica layer was grown onto the particles.

The MPTMS-coated silica particles were coded as SiM followed by a batch number and a letter indicating whether maghemite or cobalt ferrite had been added (e.g. SiM10C).

Table 2.1. Amounts of solutions used for grafting the silica particles with MPTMS.

Silica dispersion	V_{SiO_2-disp} (mL)	V_{EtOH} (mL)	$V_{NH_3,29\%}$ (mL)	V_{MPTMS} (mL) (mol MPTMS/m^2 SiO_2)
SiM1 (SiC)	20	10	0.5	0.0075 ($7.6 \cdot 10^{-6}$)
SiM2 (SiC)	20	10	0.5	0.075 ($7.6 \cdot 10^{-5}$)
SiM4 (SiB)	100	50	2.5	4.0 ($5.2 \cdot 10^{-4}$)
SiM5 (SiB)	100	50	2.5	0.4 ($5.2 \cdot 10^{-5}$)
SiM6 (SiB)	200	100	5.0	0.4 ($2.6 \cdot 10^{-4}$)
SiM9 (SiA)	200	100	- [a]	0.7 ($1.3 \cdot 10^{-4}$)
SiM10 (SiA)	200	100	- [a]	1.4 ($2.6 \cdot 10^{-4}$)
SiM12 (SiA)	200	100	- [a]	1.4 ($2.6 \cdot 10^{-4}$)

[a] Dispersion SiA was prepared < 4 months before being grafted with MPTMS and it was assumed that enough ammonia was still present.

Silica deposition onto silica-ferrite composite particles

The Stöber method used for the synthesis of silica particles was also employed for precipitating a silica layer onto the composite particles. To prevent aggregation during the coating procedure, it was necessary to work with a diluted dispersion of core-shell particles that was subjected to ultrasonication and mechanical stirring. In addition to this, to prevent the formation of new silica particles, the glassware was cleaned carefully. Adding too much TEOS at once may result in the secondary nucleation of silica particles; consequently, TEOS was added, at first, in small portions with a pipet. In later coating experiments, the pipet was replaced by a Gilson peristaltic pump for the dropwise addition of TEOS [66, 67] until a desired silica shell thickness had been obtained. The growth of the silica layer was monitored with TEM.

In the first growth experiment, 0.02 g of dispersion SiM1C in 5 mL of water was added to a mixture of 90 mL of ethanol and 3.6 mL of NH_3(29%). Five portions of 10 μL TEOS (1 vol % in ethanol) were added to this mixture with a pipet in 10 minutes intervals. The ultrasonication and stirring of the reaction mixture was continued for 4 hours after the last addition of TEOS. After the mixture was centrifuged, the particles were again redispersed in a mixture of 5 mL of water, 90 mL of ethanol and 3.6 mL of NH_3(29%). The addition and cleaning procedure was repeated four times, adding portions of (1) $5 \times 10\mu$L, (2) $5 \times 20\mu$L, (3) $3 \times 100\mu$L and (4) $4 \times 100\mu$L of TEOS (1 vol % in ethanol).

In later experiments, aqueous dispersions (20 mL) of the silica maghemite/cobalt ferrite composite particles were mixed with ethanol and a base with a total volume of 1000 mL in a 3000 mL round-bottom flask equipped with a mechanical stirrer (for synthesis details, see Table 2.2). The flask was inserted into a 25 °C ultrasonic bath. TEOS (1 vol % in ethanol) was added dropwise at a rate of $\sim 4.5 \cdot 10^{-4}$ mol TEOS/hour using a peristaltic pump. Prior to use, the PVC tubings of the pump were rinsed with 10 mL of pure ethanol to remove any impurities that might act as seeds for new silica particles. Nitrogen flow around the inlet of TEOS/ethanol into the reaction flask was applied to prevent polymerisation inside the droplets before reaching the dispersion of composite particles.

The first coating attempts were performed using ammonia (0.6 M) as base. However, the evaporation of ammonia retards or may even stop the silica growth. Therefore, an attempt was made to use 0.01 vol% TMAH (10 mL, 1 vol % in water added to 1000 mL of reaction mixture) in the reaction mixture instead of ammonia to avoid this problem [68]. For silica growth on cobalt ferrite composites this approach worked well. However, in the case of maghemite composites, TMAH prohibits silica growth for reasons that are not yet clear. For silica growth on maghemite composites, ammonia was used again, but with a higher initial concentration of ammonia (0.8 M) than that used in the first experiments.

Table 2.2. Synthesis details for silica deposition onto the composite particles.

sample code*)	composite particles (g)	TEOS addition rate (mol/h)	base
SiM5Cs	0.107	$4.5 \cdot 10^{-4}$	NH_3
SiM6Cs	0.158	$4.5 \cdot 10^{-4}$	TMAH
SiM9Ms	0.096	$4.5 \cdot 10^{-4}$	TMAH
SiM10Cs	0.196	$2.3 \cdot 10^{-4}$	TMAH
SiM10Ms	0.110	$2.3 \cdot 10^{-4}$	TMAH
SiM12Ms	0.189	$1.2 \cdot 10^{-4}$	NH_3

The coating procedures were continued for several days. After stopping the TEOS addition, the ultrasonication and stirring of the reaction mixture were maintained for at least four hours to make sure that all of the TEOS had reacted to avoid the formation of dumbbell-shaped particles. The silica-coated samples were labelled by adding an "s" to the code of the starting dispersion (e.g. SiM10Cs).

Characterization methods

TEM was performed with a Philips Tecnai12 microscope using formvar-coated copper grids on which a droplet of dilute particle dispersion had been placed and from which the solvent had been evaporated. For each dispersion of composite particles, three TEM grids were prepared: the first one was dried at room temperature, the second was exposed to a homogeneous magnetic field of 1.0-1.3 T between the poles of a Bruker electromagnet for 15 minutes before it was left to dry and the third grid was left to dry completely in the magnetic field. Particle size and polydispersity were determined from analysis of TEM pictures. Magnetization curves of dry particles were measured with a Micromag 2900 alternating gradient magnetometer (Princeton Measurements Cooperation). From the obtained magnetization curves, the remanence magnetization divided by the saturation magnetization, M_r/M_s, was calculated as an indication of the fraction of thermally blocked dipole moments in the sample.

2.4. Results & discussion

Starting dispersions

TEM pictures of the silica dispersions show spherical particles with a low polydispersity. Radii obtained from TEM pictures (see Table 2.3) are usually smaller than radii obtained with static light scattering, which is due to the shrinkage of the particles due to the vacuum applied in the electron microscope and that a volume-averaged radius is measured with SLS compared to the number-averaged sphere radius from image analysis of TEM pictures.

Table 2.3. Radii of the silica cores.

Sample Code	R_{TEM} (nm)	R_{SLS} (nm)
SiA	135 ± 9	152
SiB	121 ± 6	155
SiC	173 ± 7	204

The maghemite and the cobalt ferrite particles are irregular in shape and polydisperse, which is usual for particles prepared with a coprecipitation method [43,45]. Estimates of particle radii obtained from TEM pictures and magnetization curves are listed in Table 2.4. It should be noted that the TEM-radii are difficult to obtain accurately due to the irregular shape of the particles and particle overlap. At the same time, the magnetic radii are overestimated since these are calculated from magnetization curves, assuming monodisperse particles.

Table 2.4. Properties of the maghemite and cobalt ferrite dispersions.

sample code	R_{TEM} (nm)	polydispersity (%)	a_m (nm)
FFM3	∼ 3	29	5.8
CoF12	∼ 8	34	9.6
CoF13	∼ 7	30	8.4

Silica-ferrite composite particles

Electrostatic attachment. Both the silica and the cobalt ferrite particles form stable dispersions in the pH range of 3.0-5.0. After mixing the silica and cobalt ferrite particles, the insufficient attraction between silica and ferrite particles typically results in a white sediment (silica) and a dark (cobalt ferrite) supernatant. Furthermore, strong adsorption or the lack thereof can be observed with electron microscopy (see Figure 2.2). For cobalt ferrite, we found the maximum attraction at pH = 4.0-4.3, and for maghemite, the maximum attraction to the silica surface is expected to be in the range of pH = 3-4 [64]. Because of this pH sensitivity, core-shell particles that are prepared with this method cannot be redispersed in a Stöber mixture for silica coating because it results in the desorption of the ferrite particles from the silica surface.

Chemical attachment. Cobalt ferrite and maghemite can be attached to silica spheres coated with MPTMS without desorption when the pH or the solvent is changed. Compared to the composite particles prepared with the electrostatic adsorption method, the layer of adsorbed ferrite particles is clearly more homogeneous and is usually forming a monolayer when the coupling agent is used. In Figure 2.4, TEM and SEM pictures of the dispersion SiM6 are shown after a very small amount of cobalt ferrite particles was added and after an additional, larger amount of cobalt ferrite was added. In the first

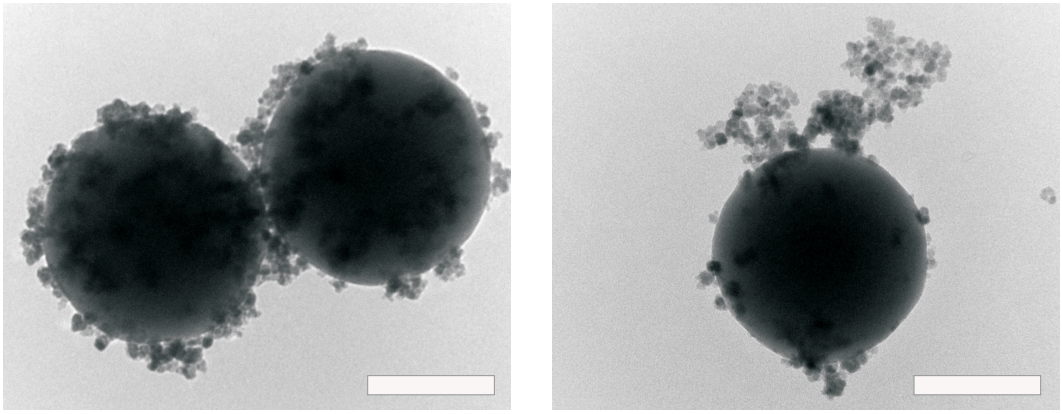

Figure 2.2. Adsorption of cobalt ferrite particles onto silica spheres via electrostatic attraction. The TEM pictures show the result of mixing the silica- and cobalt ferrite dispersions at pH = 4.0 (left) and at pH = 4.5 (right). The scale bars correspond to 200 nm.

case, inhomogeneously covered silica particles are observed, but as more cobalt ferrite is added, the silica particles become fully covered with cobalt ferrite. However, an insufficient amount of the coupling agent on the surface of the silica particles results in little or even no cobalt ferrite/maghemite attaching to the silica particles, even after a large excess of magnetic particles had been added to the silica dispersion. TEM studies also indicate that the duration of stirring after mixing the silica and magnetic particle dispersions influences the number of adsorbed magnetic particles. Furthermore, it is observed that more MPTMS has to be used for maghemite than for cobalt ferrite particles to obtain silica particles fully covered with magnetic particles. At low concentrations of MPTMS, the silica surface can be fully covered with cobalt ferrite, whereas on the same surface, only a few maghemite particles can be attached.

Silica-ferrite composite particles coated with silica

Silica-cobalt ferrite particles. The deposition of silica onto the silica-ferrite composite particles results in homogeneously coated particles with an irregular surface that smoothes out as the silica layer grows (see Figures 2.3 and 2.5). The silica growth on SiM2Co took place in several steps, which allowed us to observe the growth of the silica layer (see Figure 2.3) using electron microscopy. However, growth in several steps including purification in between each step inevitably results in the loss of particles, which reduces the yield of coated particles.

Using a peristaltic pump for the continuous addition of TEOS results in homogeneously coated particles. However, with this coating method (which is continued for several days), the evaporation of ammonia during the growth eventually stops the silica growth. This was observed for the dispersion SiM5C, in which only a thin silica layer precipitated on the particles, which was hardly visible with electron microscopy. The

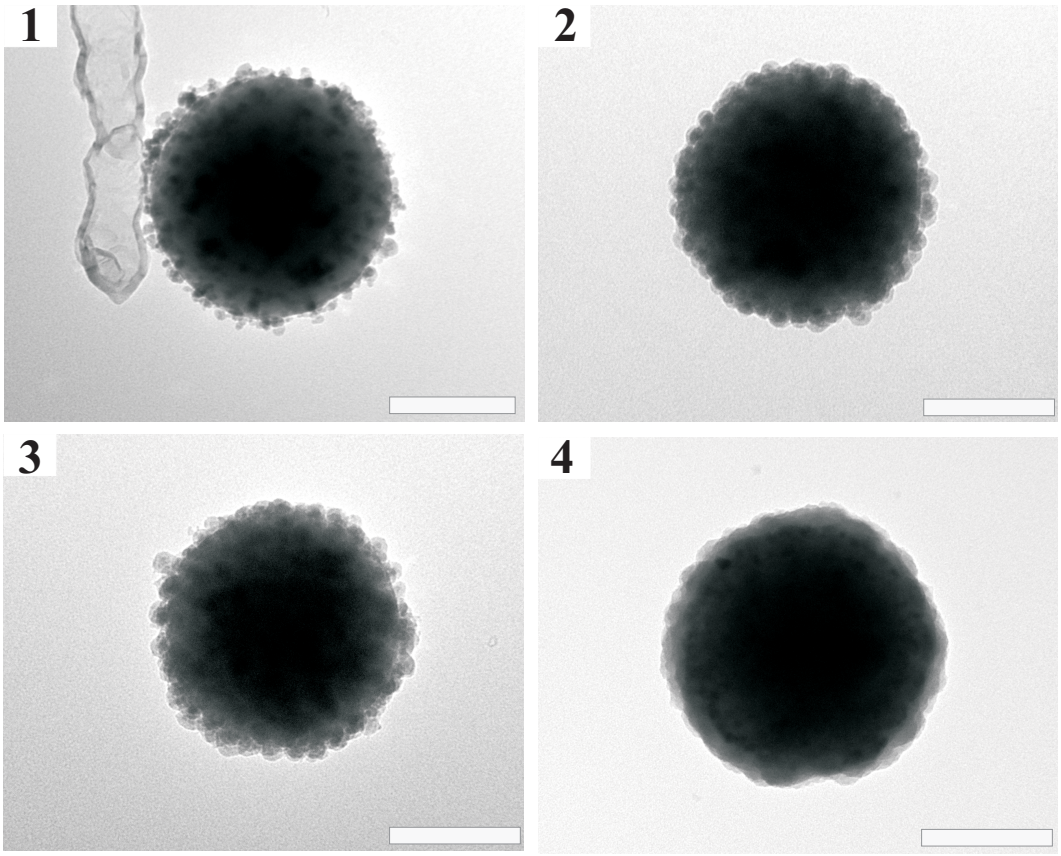

Figure 2.3. Silica growth onto composite particles of SiM2Co monitored by TEM, which shows the gradually increasing silica layer thickness from no silica present in picture 1 to a fully grown silica layer in picture 4. The scale bars correspond to 200 nm.

addition of more TEOS did not increase the thickness of the silica layer, nor had any new silica particles been formed. The silica growth on SiM6C and SiM10C shows that this problem can be solved by replacing the ammonia with TMAH, which does not evaporate and allows the silica growth to be continued for days without adding more TMAH.

The silica growth on the SiM6C composite particles resulted in a final radius of 200 ± 10 nm and for SiM10Cs the final radius was 168 ± 9 nm. This corresponds to silica layers of approximately 65 and 20 nm, respectively. The cobalt ferrite particles are still visible through the silica layer in the electron microscope. Despite the dilution and ultrasonication, however, some aggregates are formed during the coating procedure, resulting in dumbbells and larger clusters coated with silica. Free cobalt ferrite particles were present in the reaction mixture as well, acting as seeds for silica growth. Purification of the dispersions is possible, but this inevitably leads to a loss of material. With a silica layer present, the composite particles become stable in ethanol as well as

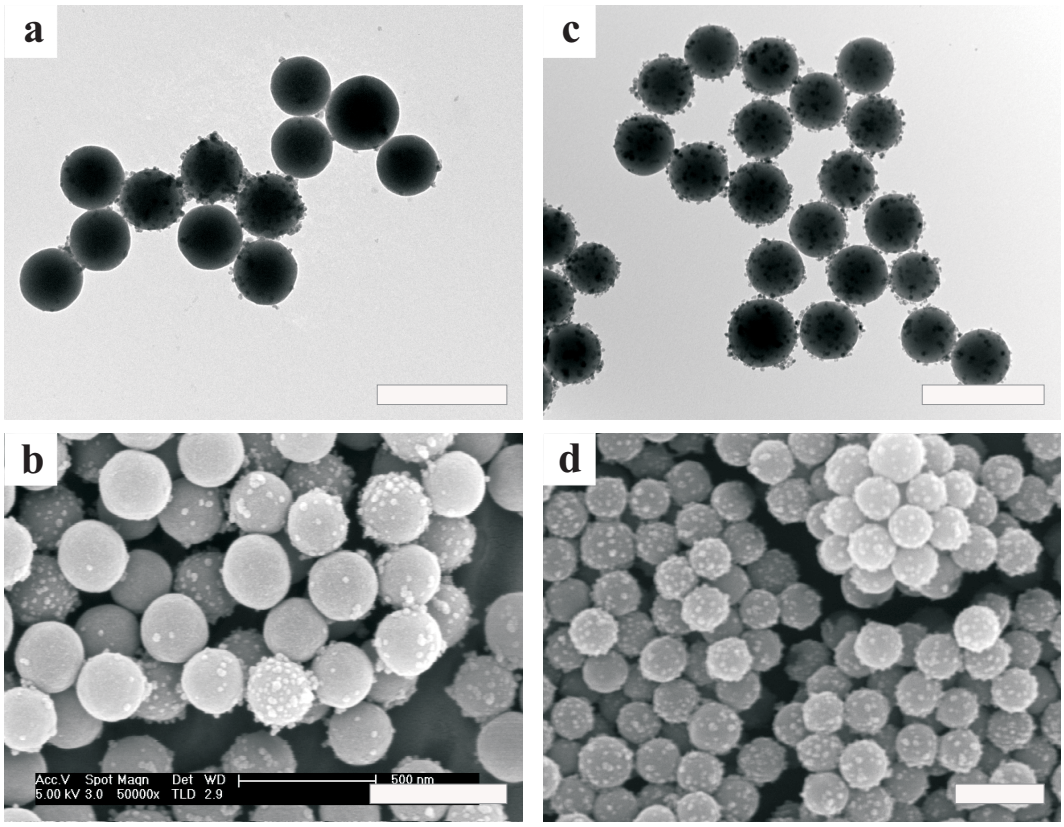

Figure 2.4. TEM and corresponding SEM picture of SiM6C after a small amount of cobalt ferrite was added (a-b) and after an excess of cobalt ferrite was added, which was followed by subsequent purification from free cobalt ferrite particles (c-d). The scale bars correspond to 500 nm.

in water and DMSO. For example, the sedimentation rate of SiM6Cs in ethanol is 0.4 mm/h compared to the starting dispersion, which flocculates immediately.

Silica-maghemite particles. In the first two attempts to grow a silica shell around the particles with maghemite (SiM9M and SiM10M), TMAH was used. However, the TEM pictures showed that silica is formed but is not deposited on the core-shell particles. Instead, a large number of new silica particles are formed. However, when using ammonia with a higher concentration compared to that used in the initial experiments (SiM5C), enough silica deposits before too much ammonia has evaporated. The successfully coated particles SiM12Ms, with a silica layer thickness of roughly 15 nm, are shown in Figure 2.5 C and F.

Magnetic properties

TEM pictures of the dispersions that were dried either in a homogeneous magnetic field or after being exposed to a homogeneous magnetic field of 1.0-1.3 T for 15 minutes were compared to the pictures of the dispersions that had not been exposed to a field (see Figures 2.5 - 2.7).

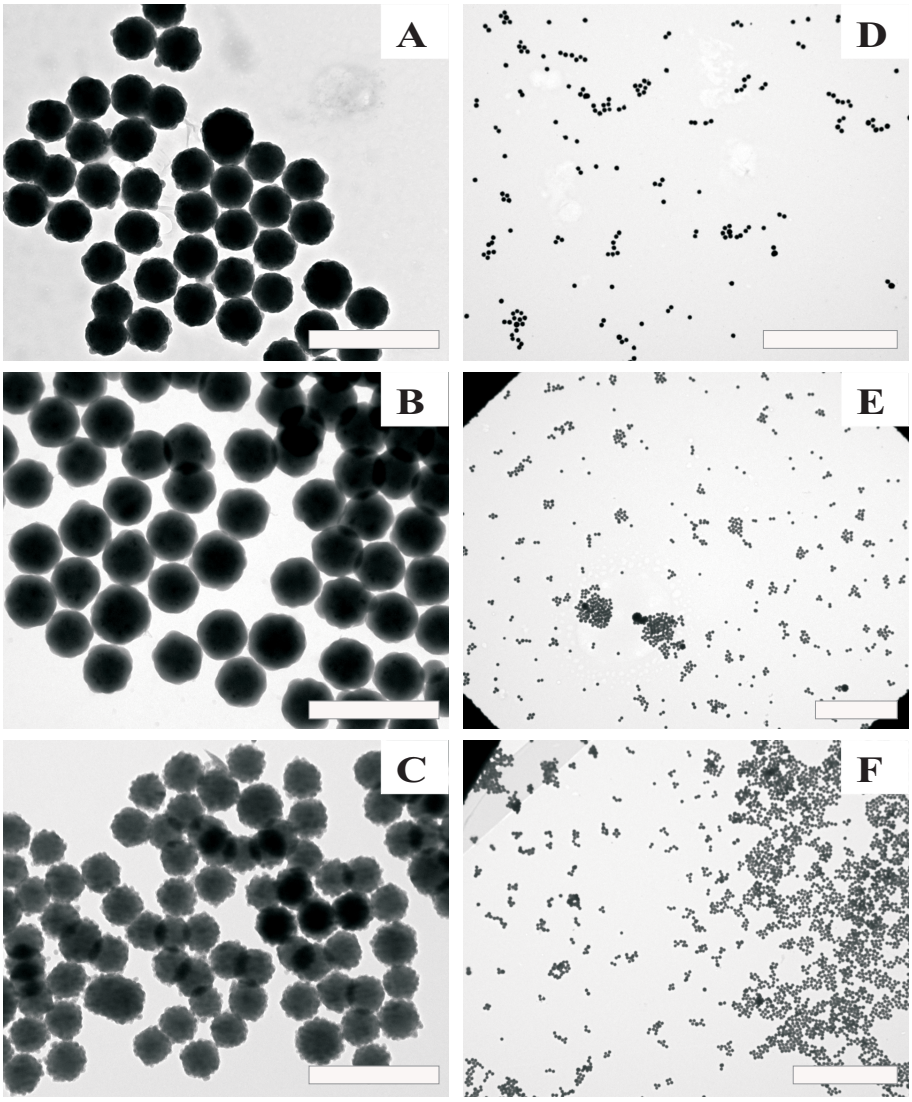

Figure 2.5. Dispersions of silica-coated composite particles SiM10Cs (A and D), SiM6Cs (B and E) and SiM12Ms (C and F). The dispersions were dried on the TEM grids without being exposed to a magnetic field. The scale bars correspond to 1 μm (A-C) and 10 μm (D-E).

The silica composites with either cobalt ferrite or maghemite without an outer silica shell all form extensive anisotropic structures which align with the magnetic field. When a silica layer is present there is a clear difference between the particles with a shell thickness of 20 nm (SiM10Cs), for which the structures align with the field when dried in a homogeneous magnetic field, and the particles with 65 nm shell thickness (SiM6Cs), for which no significant difference is observed whether or not the dispersion had been dried in a field.

In all cases, when the dispersions had been exposed to a field for 15 minutes before being dried, no extensive structures were observed, which indicates that the large dipole

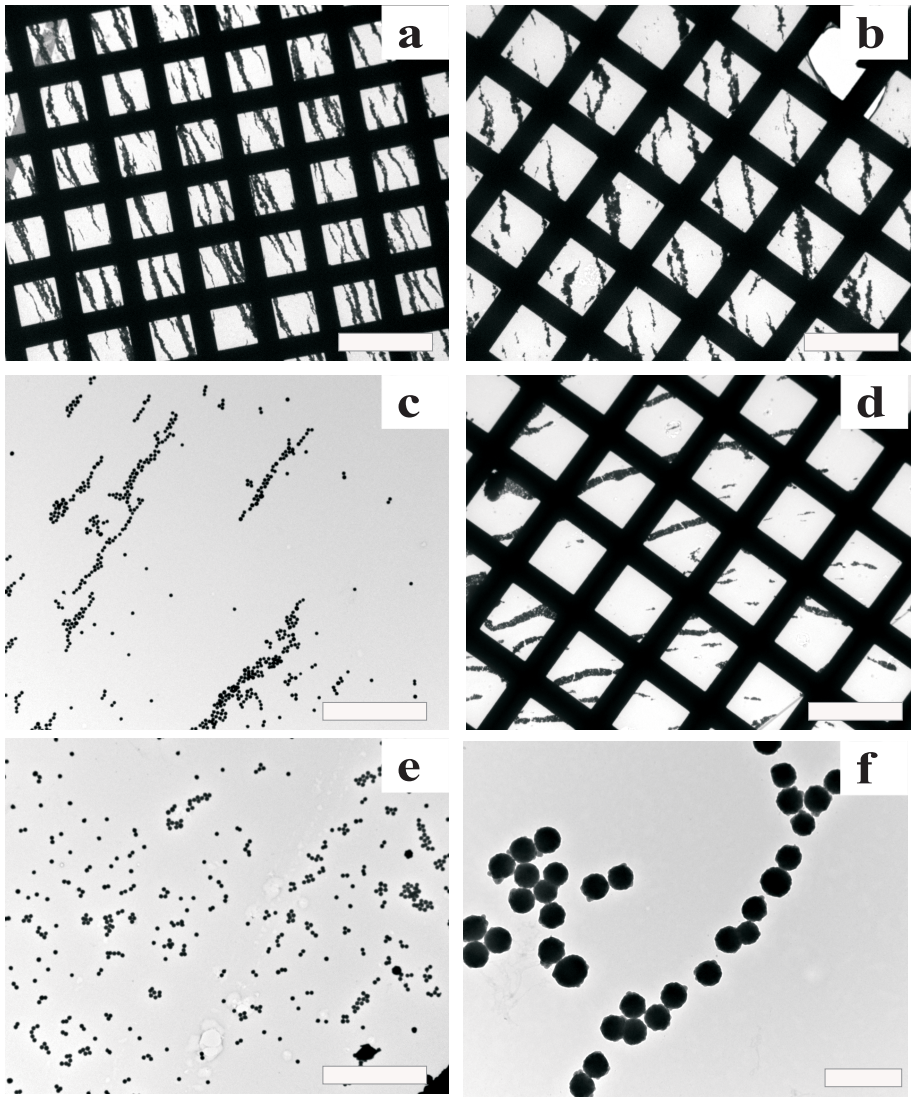

Figure 2.6. Dispersions of composite particles, all dried on a TEM grid in a homogeneous magnetic field of 2 T. (a) SiM10C without silica coating (scale bar 100 μm); (b) SiM12M without silica coating (scale bar 100 μm); (c) SiM10Cs with a 20-nm silica layer (scale bar 10 μm); (d) SiM12Ms with a 15-nm silica layer (scale bar 100 μm); (e) SiM6Cs with a 65-nm silica layer (scale bar 10 μm); (f) magnified TEM-picture of SiM10Cs (scale bar 1 μm). It can clearly be seen how the presence of a silica layer screens the dipole moments of the magnetic composite particles and how the extensive anisotropic structures of non-coated particles gradually disappear as the thickness of the silica layer increases.

moment induced by the external field either partially or completely decays after switching off the field. This finding is supported by the magnetization curves of dry samples of SiM10C, SiM12M, CoF13, and FFM3, which are shown in Figure 2.7 and Table 2.5. For dry SiM10C $M_r/M_s = 0.24$, which implies that only 24% of the individual moments

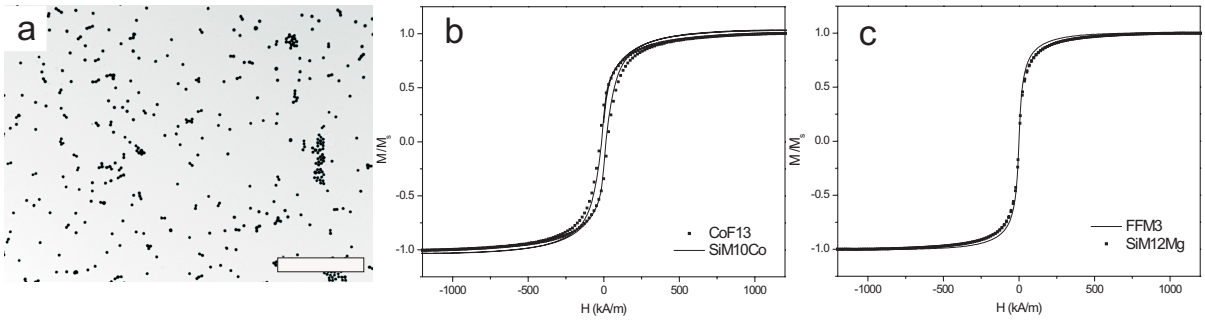

Figure 2.7. Dispersion of composite particles with SiM10Cs dried on a TEM grid after a 15 minutes exposure to a homogeneous magnetic field of 2 T (a) together with magnetization curves of CoF13 and SiM10C (b) and of FFM3 and SiM12M (c). The scale bar corresponds to 10 μm.

stay aligned after the external field has been removed. This means that the magnetic interaction between the particles, after switching off the field, is only about 6% of the interaction potential when all the dipole moments are aligned with a field according to Eqn 2.1. For the maghemite particles, this effect is even lower (see Table 2.5), which is expected for a soft magnetic material.

Table 2.5. Remanence magnetization divided by the saturation magnetization for the nanoparticles and composite particles.

Sample Code	M_r/M_s
FFM3	0.011
CoF13	0.293
SiM12M	0.007
SiM10C	0.236
SiM10C[a]	0.243

[a] The sample was left for 1 h at 2 T before the magnetization curve was measured.

The number of adsorbed magnetic particles per silica sphere calculated from M_s corresponds to a dipolar interaction potential of 5 k_BT (see section 2.2) and is roughly the number of adsorbed magnetic particles as found from the SEM pictures of SiM6C (see Figure 2.4). Furthermore, the calculated decay of the interaction potential in Figure 2.1B is in agreement with the observations made here for the silica-cobalt ferrite particles: anisotropic structures can still be observed for a silica layer thickness of 20 nm but not when the silica layer thickness is 65 nm, which means that the interaction potential exceeds 2 k_BT in the first case and is lower than 2 k_BT in the latter case.

2.5. Conclusions

We have demonstrated that well-defined, monodisperse magnetic silica particles can be prepared by irreversible adsorption of maghemite or cobalt ferrite particles onto colloidal silica spheres grafted with the thiol-functionalized silane coupling agent 3-mercaptopropyl(trimethoxy)silane. We have also shown that it is possible to electrostatically adsorb ferrite particles onto silica particles, but with the drawback that the method is strongly pH-sensitive, leading to desorption of the magnetic particles at alkaline pH. This problem is avoided when silica-ferrite composites are prepared using a silane coupling agent, which yields composite particles that can be subjected to a change in solvent, strongly alkaline media and ultrasonication without the ferrite particles desorbing from the silica surface. Moreover, the silica-ferrite composite particles can be coated with silica by following the Stöber method, in which the composite particles are introduced as seeds in a seeded growth step. Aggregation of the composite particles during the growth can be avoided by using ultrasonication, and once a silica coating is present, the particles form stable dispersions in ethanol, water and DMSO.

In a homogeneous magnetic field, a large magnetic dipole moment is induced inside the silica-ferrite composite particles, which leads to the formation of extensive anisotropic structures aligned with the external field. When these composite particles have been coated with a relatively thin silica layer of 20 nm, such structures can be observed. However, as the thickness of the silica layer is increased to 65 nm, anisotropic structures can no longer be observed, which is in agreement with the interaction model from section 2.2. The possibility of tuning the interactions by controlling the thickness of the silica layer and the size of the silica core provides a suitable colloidal model system for future microscopy studies of dipolar structure formation.

Appendix: Composite particles with a fluorescent silica core

For direct imaging of colloids with confocal scanning laser microscopy, particles must be labelled with a fluorescent core with a radius $R \geq 200$ nm. The magnetic silica particles described in this chapter were labelled with the fluorescent dye fluorescein isothiocyanate (FITC) using a slightly modified synthesis route with respect to what was previously described in this chapter.

First, 0.47 g (1.2 mmol) FITC was dissolved in 2.77 g (12.5 mmol) of the silane coupling agent 3-(aminopropyl)triethoxysilane (APS) and 18 mL of ethanol was added to promote covalent bonding of the dye molecules into the silica particles [47, 69]. The mixture was stirred magnetically overnight while kept under nitrogen atmosphere in the dark. Second, fluorescent silica cores were prepared with the Stöber method as described in Section 2.3, by quickly adding 75 mL TES and 1 mL FITC-APS to a mixture of 1770 mL ethanol and 230 mL 25% ammonia solution. After 4 h, another portion of TES (25 mL) was added. The particles were purified from excess dye by repeated centrifugation and redipersion in ethanol. After thorough purification, the particles were redispersed in a fresh Stöber mixture and 25 mL of TES was added to grow an outer silica shell, free of dye molecules. We observed that this purification step and growth of a thin non-fluorescent silica layer is crucial for the surface reaction with MPTMS, probably due to a change of the surface properties caused by the use of APS [70]. The resulting fluorescent silica particles with a radius $R_{TEM} = 378 \pm 14$ nm were coated with MPTMS and covered with cobalt ferrite and an outer silica shell in the same way as the non-fluorescent silica cores. The total radius of the silica coated composite particles was $R_{TEM} = 409 \pm 9$ nm, which means that the thickness of the outer silica shell was approximately 15 nm. For long-term stability, the particles were grafted with 3-(Trimethoxysilyl)propyl methacrylate (TPM) following the same procedure as for the MPTMS-grafting described in Section 2.3 [48].

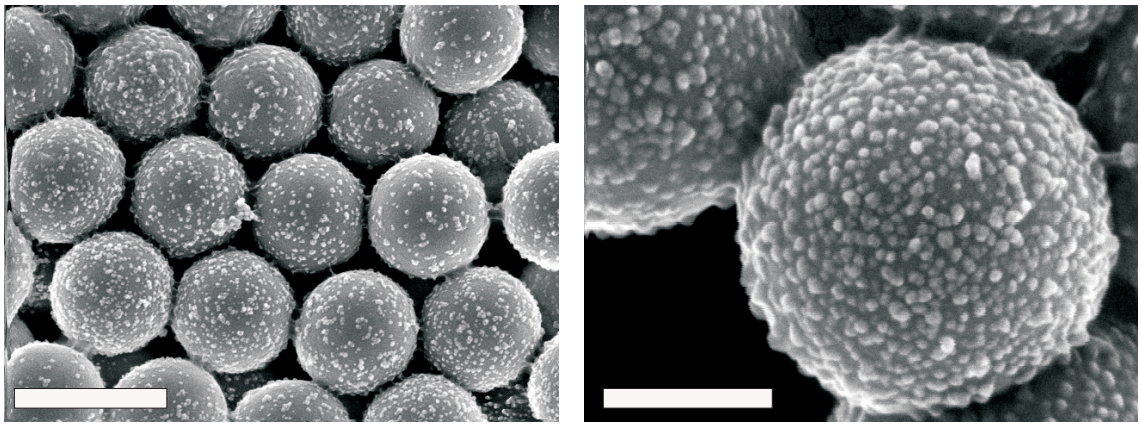

Figure 2.8. SEM pictures of silica-coated cobalt ferrite-silica composite particles with a fluorescent core. The scale bars represents 1 μm and 300 nm.

Direct imaging of magnetic silica particles with confocal microscopy

The fluorescent magnetic silica particles were dispersed in a solvent mixture of DMSO and ethanol with a refractive index $n = 1.455$, close to that of silica [71]. The particles were imaged using a Nikon TU 2000U inverted microscope with a Nikon C1 scanning head, a Nikon 100 × CFI Plan Apochromat, NA 1.4 oil-immersion lens and an Ar ion laser ($\lambda = 488$ nm). The objective of the microscope was placed between the poles of a homebuilt electromagnet with a variable field up to 90 mT. In Figure 2.9, confocal images of fluorescent magnetic silica particles are shown before (left) and during (right) exposure to a homogeneous magnetic field of 90 mT. Without the exposure to an external field, the particles are isotropically distributed. When a magnetic field is applied, the particles form anisotropic structures within a few seconds. As the field is switched off, these long strings of particles start to break up within about one second, in agreement with the results presented in section 2.4. When all individual cobalt ferrite dipoles are aligned in an external magnetic field, the induced dipole moment is large enough for the composite particles to form dipolar structures. However, the remanent dipole moment after field exposure is not, and consequently the structures are dissolved. From magnetization curves of this system, the ratio M_r/M_s was found to be 0.27.

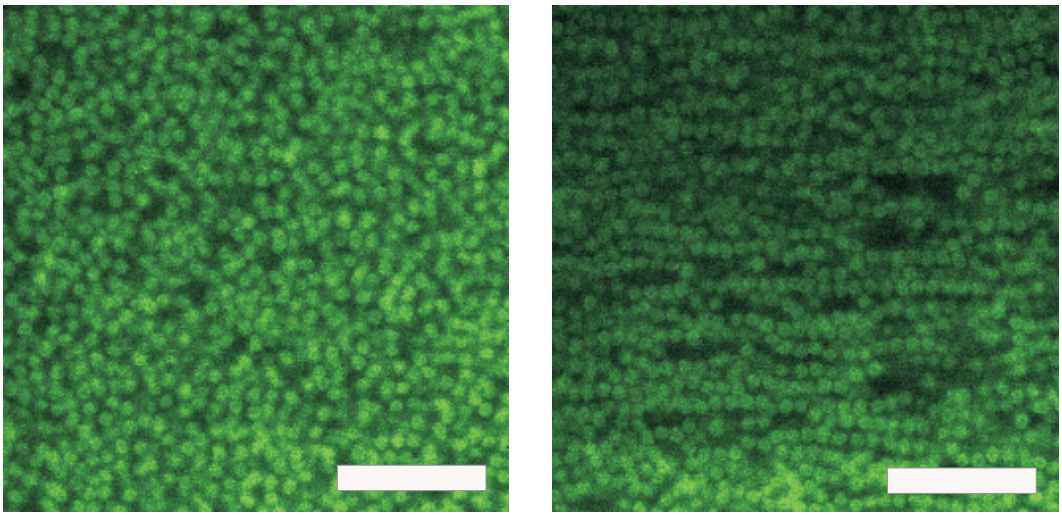

Figure 2.9. Confocal microscopy images ($34 \times 34\ \mu m^2$) of TPM-coated magnetic silica particles with FITC-labelled cores in DMSO/ethanol. Left: The particles in zero field. Right: The particles when exposed to a homogeneous field of 90 mT.

Acknowledgements

Gerard van Ewijk and Jilles Smids are acknowledged for their exploration of adsorption of ferrite particles onto colloidal silica, which formed the starting point for the work presented in this chapter. We thank Judith Wijnhoven, Dominique Thies-Weesie and Chantal Vonk for many helpful discussions about silica particles, silica coatings and coupling agents. The SEM pictures were made by Stefano Sacanna. The work on fluorescent silica particles was done together with Bob Luigjes. Bonny Kuipers and Emile Bakelaar equipped the confocal microscope with an electromagnet.

3

Thiol-Functionalized Silica Colloids, Grains, and Membranes for Irreversible Adsorption of Metal(oxide) Nanoparticles

Abstract

Thiol-functionalization is described for silica surfaces from diverse origins, including commercial silica nanoparticles and Stöber silica as well as silica structures provided by porous glasses and novel polymer-templated silica membranes. The functionalization allows in all cases for the irreversible binding of metal(oxide) particles from a solution. Examples are the adsorption of $CoFe_2O_4$ particles for the preparation of magnetizable silica colloids and silica structures, and gold nanoparticles that directly nucleate and grow on thiol-functionalized silica in a solution of $HAuCl_4$ upon addition of a reducing agent.

3.1. Introduction

For many technical applications, it is desirable to chemically modify the surface of nanostructured materials, such as colloidal particles, porous micron sized grains and membranes [72–75]. Such materials provide large surface-to-volume ratios and at the same time they can readily be separated from a dispersion medium either by sedimentation, removal by a membrane or - when having magnetic properties - with an external magnetic field, making them suitable for separation purposes. Arakaki *et al.* [61], for instance, have reported on thiol-functionalized silica gel as adsorbent to remove toxic metal species such as mercury from aqueous solutions. Moreover, chemical adsorption of metals to particles and grains might also be interesting for applications in for instance decorative coatings due to their color properties.

A large variety of nanostructured materials are made of, or can be coated with silica [20, 50, 76–80]. An important advantage of silica is its well-known surface chemistry and the broad spectrum of organosilanes available to modify the silica surface with functional groups to give it desired properties [48, 65]. This type of modification has for instance been used to stabilize colloidal silica in organic solvents [48] but also to chemically bind magnetic metal oxide particles [46] or other metal nanoparticles to silica particles [**?**, **?**, 75, 82] to give them different magnetic or optical properties.

In this work, we have investigated the functionalization of a variety of silica nanostructures with thiol-groups as a general method for chemical binding of various metal or metal oxide particles to silica. Gold nanoparticles were used as a probe for the presence of thiol-coating, since it is well-known that gold has a high affinity for thiols [57,81,82]. These gold particles, synthesized by reduction of gold chloride hydrate ($HAuCl_4$) with sodium borohydride ($NaBH_4$) are small ($R \sim 2$ nm) and have a high electron density which makes them easy to distinguish from the silica during electron microscopy characterization. The following four types of silica structures were investigated:

1) Commercially available small silica particles (Bindzil, $R \sim 6$ nm), for which thiol-functionalization and metal adsorption, as far as we know, have only been described for gelated particles [83] but not for silica particles of this size while they remain in a stable dispersion.

2) Larger silica colloids prepared with the Stöber method [50, 54] (R = 158 nm), as well as magnetic Stöber silica with embedded cobalt ferrite ($CoFe_2O_4$) (R = 217 nm) [46].

3) Micron-sized porous silica grains, such as so-called CPG's (controlled porous glasses, see for instance refs. [77, 78]) and the mesoporous silica structure SBA-15 [76].

4) Polyethersulfone (PES) filter membranes, which were coated with the same method, after that these membranes had first been embedded in a silica crust.

Polymeric materials cannot as easily be chemically modified as silica, but it was recently shown that PES membranes can be encapsulated in silica by performing Stöber synthesis directly onto the polymer [84]. Here, we show that the addition of Bindzil silica nanoparticles results in a smooth, complete coverage of the membranes, leaving a large silica surface available for functionalization with organosilanes.

The size, shape and gold particle coverage of the various silica particles were characterized with transmission and scanning electron microscopy. In addition, the presence of thiol-groups on the smallest silica particles was investigated with infrared spectroscopy.

3.2. Experimental

Materials

The chemicals used were: tetraethoxysilane (TES, Fluka), ethanol (technical grade), ammonium solution (28.6 %, Merck), gold chloride hydrate (Fluka), 3-mercaptopropyl trimethoxysilane (MPTMS, 97 %, Fluka), sodium borohydride(Aldrich), commercial silica dispersion (Bindzil 30/360, Eka Chemicals AB), controlled porous glass (CPG0300C, Controlled Pore Glass Inc.), AG 501-X8 and Bio-Rex MSZ 501 (D) mixed bed resin (Bio Rad) and Millipore Express PLUS Membrane (polyethersulfone, hydrophilic, 0.22 μm, 47 mm, Millipore Corporation). For synthesis of silica particles, the ethanol and TES were distilled prior to use. In all other cases, the chemicals were used as received. A stock solution of 100 mL of approximately 0.02 M $HAuCl_4$ was prepared by dissolving 0.90 g $HAuCl_4 \cdot 6H_2O$ (Fluka) in doubly distilled water. This stock solution of $HAuCl_4$ was used throughout all experiments. The sodium borohydride solutions were prepared less than 30 minutes before each experiment due to the rapid oxidation of $NaBH_4$ in water.

Functionalization of Bindzil silica nanoparticles

Surface modification of Bindzil. Bindzil silica nanoparticles were received as alkaline (pH = 10) aqueous dispersions and had to be transferred to ethanol for the MPTMS grafting procedure. However, the dispersion contained soluble silicates that precipitate and cause gelation when adding ethanol. Therefore, the first step was to remove these silicates by adding 10 g of AG501-X8 and Bio-Rex MSZ 501 (D) mixed bed ion exchange resin (Bio Rad) in 100 mL Bindzil-dispersion diluted to 200 mL with doubly distilled water. The resin was left in the dispersion for several weeks [85]. After two weeks, the pH had decreased from 10 to 7, indicating that all ions initially present in the solution had been exchanged for H^+ or OH^-. The resin was filtered out and the dispersion was dialyzed for one week against ethanol in Spectra/Por Type F polyvinylidene difluoride (PVDF) dialysis membranes, refreshing the ethanol reservoir once per day. The hydrodynamic radius, $R_h = 9.5$ nm of the particles was determined by dynamic light

scattering. This hydrodynamic radius corresponds to a number averaged radius, R, of approximately 6 nm, for a polydispersity of 35 % [4].

To a mixture of 10 mL of the Bindzil dispersion in ethanol ($\phi_m = 0.167$ g/mL), 1 mL NH_3 and 90 mL ethanol (pH = 8.5), 5 mL MPTMS was added and the mixture was stirred for 40 minutes before heating it to $\sim 80°C$. Slowly, approximately 100 mL of ethanol and ammonia was removed by distillation at ambient pressure. Tests with various concentrations of ammonia showed that higher ammonia concentrations (pH > 8.5) caused the Bindzil dispersion to gel. The reaction mixture was purified from unreacted MPTMS via dialysis for 2 days against ethanol. After these two days and after refreshing the ethanol 4 times, the strong, characteristic smell of MPTMS was gone. The thiol-functionalized Bindzil particles were transferred back to (doubly distilled) water by transferring the dialysis tubes into a water reservoir. Due to the difference in density between ethanol and water, the tubes were floating at the beginning of the dialysis and slowly sinking as the ethanol content inside the tubes was reduced. The dialysis was continued for one week, refreshing the water reservoir twice per day. The dialysis was stopped when the refractive index of the reservoir was the same as that of pure doubly distilled water. The resulting aqueous dispersion of 9.5 mg/mL functionalized Bindzil particles was labeled Bindzil-SH.

Synthesis of gold particles onto Bindzil particles. The gold-silica particles were prepared by reducing $HAuCl_4$ in the presence of MPTMS-coated silica spheres. Solutions (0.1 M) of the reducing agent, $NaBH_4$, were prepared less than 30 minutes before each synthesis. In the gold particle synthesis step, $HAuCl_4$ stock solution was added first, followed by an equal volume of $NaBH_4$-solution. Immediately after adding the reducing agent, gas bubbles due to evolving H_2 (g) and a change in color, typically pink to purple, could be observed in the reaction mixture. The experiment was repeated for a certain amount of Bindzil-SH dispersion (2 mL, $\phi_m = 0.01$ g/mL, in 50 mL doubly distilled water) with various amounts of $HAuCl_4$ and reducing agent. Also the effect of stirring and the $NaBH_4$ concentration on the final product was investigated. For comparison, a blank sample was prepared using Bindzil which had not been treated with MPTMS but adding the same amount of reagents for the synthesis of gold.

Functionalization of PES-membranes covered with a silica crust

To provide the PES filter membranes with a silica layer for further functionalization, two approaches were tested. In the first method, amorphous silica was synthesized directly onto the membranes. The PES-membranes were soaked in an ammonia solution (10 mL 25% in 40mL ethanol) for approximately 1 h before placing them in between two filter papers soaked in TEOS (10 vol% in ethanol) [84]. To allow the reagents to be homogeneously absorbed, the PES-membranes were carefully blotted and left for 4h in a covered Petri dish. After that, the membranes were put into pure ethanol for at least

one day to remove any free silica particles. The membranes prepared in this way were labelled PESSt. In a second approach, it was investigated whether the Bindzil particles could be adsorbed directly onto the membranes and in this way create a silica crust on the polymer. The PES membranes were left overnight in dispersions of Bindzil particles in water (label: PESBiW) as well as in ethanol (label: PESBiEt). Additionally, some membranes were pre-treated by soaking these in an ammonia solution to investigate if the attraction between the polymer and silica particles could be due to electrostatic attraction between the silica and the PES-membrane (label: PESBiEt2).

After rinsing the presumably silica covered membranes carefully, they were transferred to a mixture of 120 mL ethanol and 1 mL 25% ammonia solution. Under slow agitation, 0.4 mL (2.1 mmol) MPTMS was added and the mixture was heated to 50 °C for 15 h. Subsequently, they were rinsed with ethanol and immersed in deionized water. We noted that the PESSt and PESBiEt2-membranes had clearly become much more hydrophilic after the treatment with MPTMS compared to the pure PES membranes. When a water droplet was placed on the surface with a pipet, the water was immediately absorbed, although at some parts of the PESSt membrane water stayed longer on the surface.

The functionalized membranes were left overnight in an aqueous dispersion of gold nanoparticles, prepared in the same way as described in section 3.2.

Functionalization of Stöber silica

A stock-solution of silica particles ($R_{TEM} = 158$ nm) was prepared by rapidly adding freshly distilled tetraethoxysilane (TES) to a mixture of 152 mL ammonia solution diluted to 25 % and 1770 mL distilled ethanol according to the method of Stöber *et al.* [50]. 400 mL of the obtained silica dispersion was diluted to 600 mL with ethanol. 2.8 mL 3-mercaptopropyl trimethoxysilane was added and the mixture was stirred for 40 minutes. Subsequently, the reaction mixture was heated to 80°C and the total volume was reduced to approximately two thirds by distillation of ethanol and ammonia at ambient pressure [46, 48] (see Chapter 2). The amount of MPTMS was chosen to be $2.6 \cdot 10^{-4}$ mol/m^2 silica surface [46] (see Chapter 2), assuming a density of 1.8 g/cm^3 for the silica particles. The mixture was left to cool down to room temperature and was subsequently washed 3 times with 150 mL ethanol (by centrifugation at 513 g) to remove any unreacted MPTMS. The thiol-functionalized particles were stored in ethanol to prevent hydrolysis of the MPTMS-silica bond.

Gold nanoparticles were synthesized in the presence of the thiol-functionalized silica particles following the same procedure as described for the Bindzil particles in section 3.2, using typically 5 mL 0.02 M $HAuCl_4$ and 0.1 M $NaBH_4$ respectively. One day before an experiment, the functionalized silica particles were transferred to doubly distilled

water by centrifugation and redispersion. In the gold nanoparticle synthesis, $HAuCl_4$-solution was added first, followed by an equal volume of $NaBH_4$-solution. All reaction mixtures were centrifuged at 228 g to remove free gold particles. The sedimentation and redispersion procedure was repeated until the supernatant had become colorless.

The silica colloids covered with small gold particles were -without any further modification- coated with an outer shell of silica in a seeded growth step. 3 mL (0.018 g) of the silica-gold dispersion Sg41 ($\phi_{\mathrm{m}} = 0.006\ g/m\mathrm{L}$) in water was added to a mixture of 5 mL ammonia solution and 95 mL ethanol and stirred vigorously while adding 0.01 mL TES. The reaction mixture was stirred for 4 hours. The experiment was repeated using 1.0 mL TES for a thicker silica layer.

Functionalization of magnetic silica particles

MPTMS-functionalized silica particles were covered with magnetic cobalt ferrite particles and subsequently coated with an outer layer of silica according to ref. [46] (Chapter 2). After purification and transfer of the thiol-functionalized particles to demineralized water, 5 mL cobalt ferrite dispersion was added and the mixture was gently shaken overnight. Free cobalt ferrite particles were removed by repeated sedimentation and redispersion and 30 mL of cobalt ferrite-silica dispersion (0.04 g/mL) was transferred to 920 mL ethanol and 50 mL ammonia solution. Small portions of TES were added every 15 minutes to obtain a silica layer around the magnetic particles. The coated particles were sedimented by centrifugation 1 h at 100 g and redispersed three times in technical ethanol to remove any free cobalt ferrite or newly formed silica particles. The dispersion was labeled SibCs.

In the following step, 30 mL (0.002 g/mL) of the SibCs particles ($R_{\mathrm{TEM}} = 217$ nm), was diluted with 10 mL of ethanol, mixed with 5 mL ammonia solution and 0.5 mL MPTMS in a round bottom flask and stirred for 40 minutes. Subsequently, 20 mL of the solvent was removed by distillation. The functionalized magnetic silica particles were purified from unreacted MPTMS by repeated centrifugation 1h at 57 g. The sediment was redispersed three times in ethanol and three times in doubly distilled water, resulting in a stable light brown dispersion. While gently shaking, 0.4 mL $HAuCl_4$ stock solution and 0.4 mL 0.1 M $NaBH_4$ was added to the thiol-functionalized magnetic silica dispersion, giving the reaction mixture a dark brown color. The particles were centrifuged 1h at 57 g and the red supernatant containing excess of gold particles was removed. Due to the initial brown color of the magnetic silica, no clear difference could be observed in the color of the sediment compared to the starting dispersion.

Functionalization of porous silica grains

Silica grains of micron-size porous glasses (see Figure 3.8a) with a mean pore size of 367 nm and a surface area of 7.1 m^2/g (data provided by supplier) were first coated with thiol-groups following the same procedure as described for Stöber silica. 3 g of

CPG0300C was added to a mixture of 90 mL ethanol and 10 mL ammonia solution. To this mixture, 1.04 mL (5.5 mmol) 3-mercaptopropyl trimethoxysilane was added and the mixture was stirred magnetically for 40 minutes, before removing approximately one third of the ethanol and ammonia by distillation. The remaining white sediment was rinsed several times with pure ethanol to remove unreacted 3-mercaptopropyl trimethoxysilane. Subsequently, the CPG-grains were transferred to doubly distilled water and 2.5 mL of the 0.02 M $HAuCl_4$-solution was added while stirring. After 10 minutes, the stirring rate was increased and 2.5 mL 0.1 M $NaBH_4$ was added, upon which the color turned purple. The grains were subsequently sedimented and rinsed several times with doubly distilled water until the supernatant became colorless and transparent. The color of the resulting sediment was light brown. The synthesis of gold nanoparticles was repeated -with the same amounts- for 3 g CPG0300C which had not been coated with MPTMS. After rinsing the sediment with water, it had regained its original white color.

The procedure was repeated for SBA-15 mesoporous silica (see Figure 3.8c). Also this resulted in a pink-colored sediment, which remained colored after several rinsing steps.

Characterization techniques

Transmission electron microscopy was performed on a Philips Tecnai 12 microscope operating at 120 kV. TEM-samples were prepared by depositing drops of diluted dispersion on formvar-coated copper grids. Scanning electron microscopy was carried out on a Philips SEM XL30SFEG microscope operating at 30 kV. Dynamic light scattering was performed on a homebuilt setup measuring at $\lambda = 514.5$ nm. Infrared spectroscopy was performed on a Perkin Elmer System 2000 FT-IR spectrometer. Since the MPTMS is only present at the particle surface, the volume of MPTMS present in a sample is only a tiny fraction of the SiO_2 volume. The samples were therefore measured on a self-supporting pellet, consisting of compressed silica particles only instead of being diluted with KBr. Additionally, the sample was heated to 120°C under vacuum while measuring to remove water and thereby reducing the O-H peak in the spectrum. With the self-supporting pellets, the MPTMS signal was increased, but with the drawback of having zero transmittance at wavenumbers were the silica absorbs. However, since the peak of interest, the S-H stretching vibration, falls outside the range where silica absorbs this is not a problem.

3.3. Results & Discussion

Functionalization of Bindzil particles

The experiments with the Bindzil dispersion show that the procedure for grafting Stöber silica particles with MPTMS, as previously described [46, 48] (see also Chapter

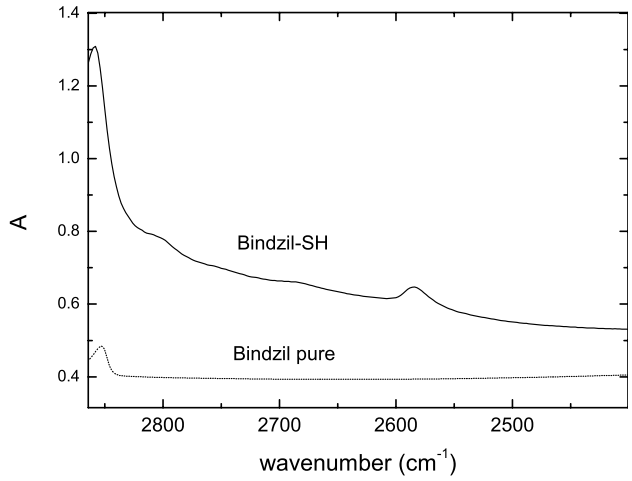

Figure 3.1. IR-spectra of Bindzil particles before and after thiol-functionalization. In the spectrum of thiol-functionalized (Bindzil-SH), a weak, but clear S-H stretch band can be found around $\nu = 2585$ cm^{-1}, which cannot be observed in the spectrum of the pure Bindzil. Since the IR-spectra were made after thorough purification from free MPTMS, it can be concluded that the MPTMS is indeed bound to the silica particles.

2), can be applied also to commercial aqueous silica sols. However, the very small particle size and the presence of soluble silicates in the aqueous phase required a few modifications of the thiol grafting procedure: firstly, the silica sol as received had to be purified from soluble silicates with a mixed bed ion-exchange resin to avoid gelation when adding ethanol. After treatment with the resin, the small silica particles could be transferred to ethanol without gelation. Secondly, to avoid centrifugation at high speed for a long time, which would have been required to sediment particles of this size, dialysis was employed to change the solvent from water to ethanol and vice versa when necessary. Finally, the pH of the ethanol/ammonia mixture should not be higher than 8.5 to avoid gelation. This repeatedly observed gelation is not likely to be due to an increase in ionic strength upon adding ammonia. This conclusion follows from the observation that even a concentration of 10 mM $LiNO_3$ in the Bindzil dispersion does not produce a gel. Possibly too much ammonia promotes condensation of surface silanol groups from different particles. Note in this respect that the number concentration of the small Bindzil particles is very high. After treatment with MPTMS, the Bindzil particles were stable in water as well as in ethanol. FT-IR spectra of Bindzil particles before and after treatment with MPTMS are shown in Fig. 3.1. In the spectrum of Bindzil-SH a weak, but clear S-H stretch band can be found around $\nu = 2585$ cm^{-1}, which cannot be observed in the spectrum of the pure Bindzil. Since the IR-spectra were made after thorough purification from free MPTMS, it can be concluded that the MPTMS is indeed chemically bound to the silica particles.

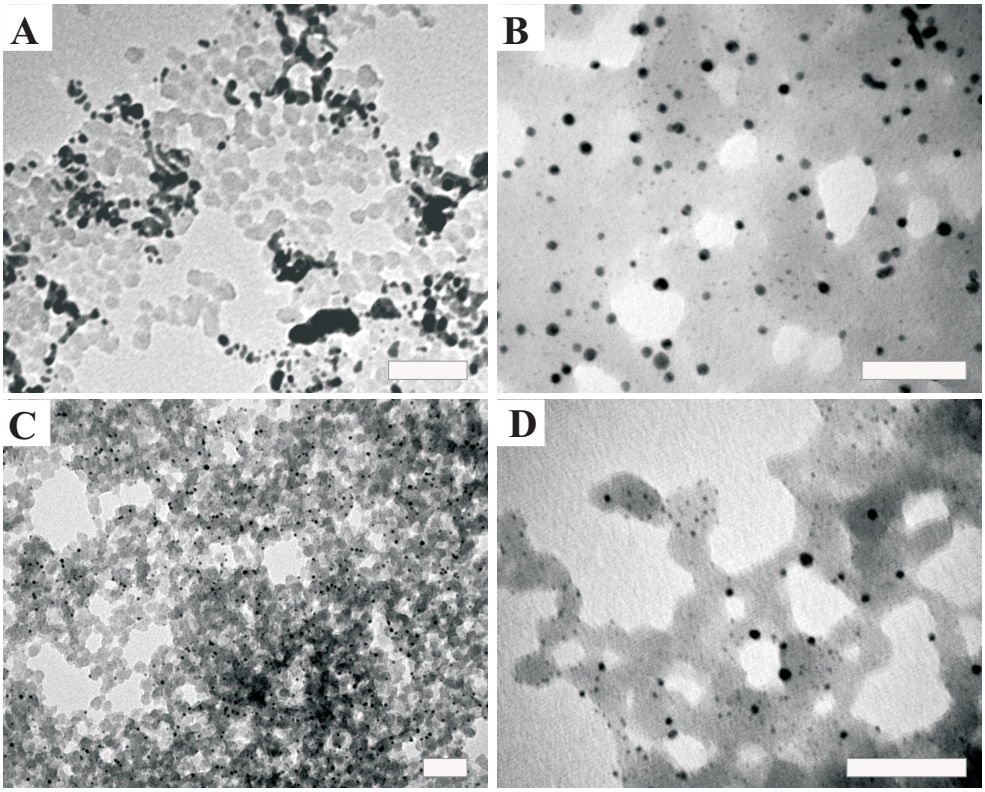

Figure 3.2. TEM pictures showing the results of direct synthesis of gold particles in the presence of Bindzil particles: (A) without prior treatment with MPTMS and (B-D) after treatment with MPTMS. Although the silica particles are melting rapidly in the electron beam of the microscope, it can be observed that in the sample where MPTMS is present discrete gold nanoparticles are surrounding the particles, whereas the gold particles in the sample where no MPTMS had been added, the gold particles coalesce into large clusters. The scale bars correspond to 50 nm.

After performing the reduction of $HAuCl_4$ in the presence of MPTMS-grafted Bindzil particles, the resulting brightly red-colored dispersions were stable without any gelation or flocculation for at least 3 months. Unfortunately, the 6 nm silica particles melt in the electron beam when performing TEM (see Fig. 3.2B) so that direct confirmation of gold particles being attached to the silica particles is hindered. Nevertheless, several observations clearly confirm the (covalent) attachment of gold particles to the Bindzil-particles: without the MPTMS present, the gold particles coalesce and large gold clusters can be found on the silica melt (see Fig. 3.2A). When using MPTMS-grafted Bindzil particles, discrete gold particles are found almost exclusively in and around the melt of silica particles (see Fig. 3.2B-D). This observation, together with the S-H peak found in the IR-spectrum of the MPTMS-treated Bindzil particles confirm the presence of thiol-groups on the silica surface. The gold particles vary in size, but we were not able to assess a clear relation between experimental conditions such as the

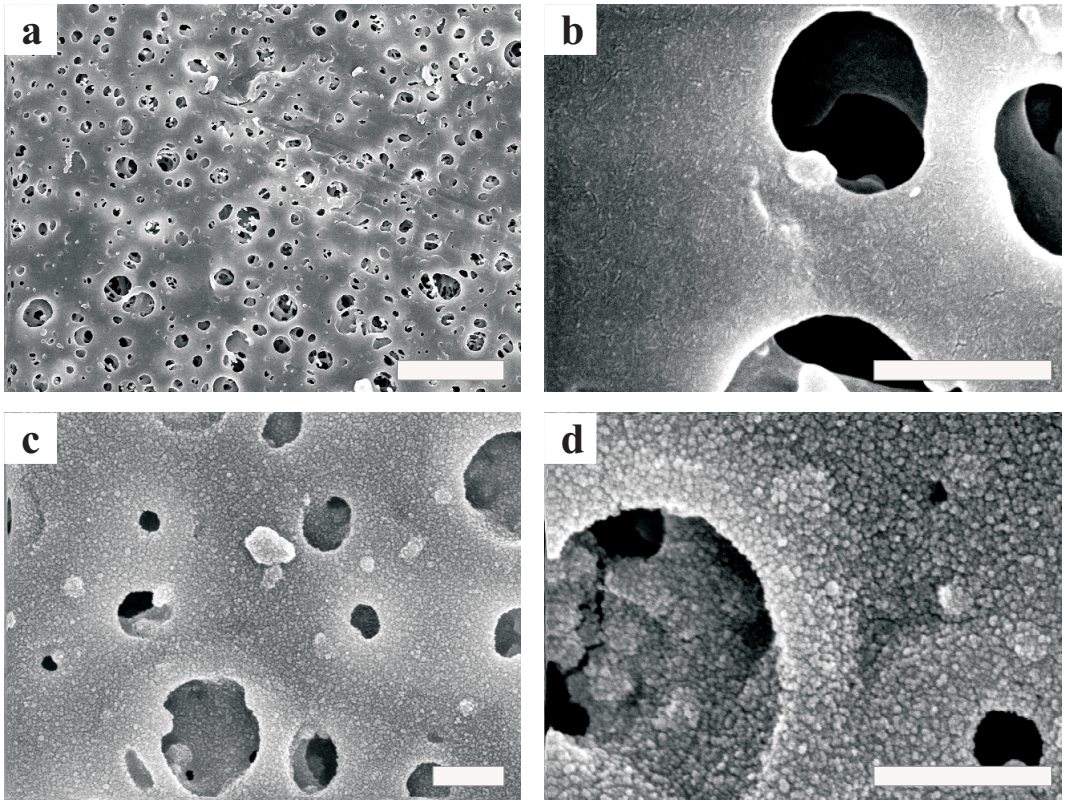

Figure 3.3. SEM pictures of (a)-(b) PES-membranes as received and (c)-(d) PES-membrane PESBiEt2 completely covered in a crust of Bindzil silica nanoparticles. The scale bars correspond to 5 μm (a) and 500 nm (c-d).

stirring and concentration of $NaBH_4$ on the size or polydispersity of the gold particles. However, the amount of $HAuCl_4$ was optimized around 50 mL per gram Bindzil. When more $HAuCl_4$ was used, free gold nanoparticles could be observed on the TEM-grid.

Functionalization of PES-Membranes Covered with a Silica Crust. PES membranes immersed in a Bindzil dispersion in ethanol, in particular the ones which had been soaked in ammonia solution prior to exposure to Bindzil (PESBiEt2) showed complete coverage of the polymer with silica nanoparticles, even inside the pores (see Figure 3.3c-d). Membranes that had not been soaked in ammonia first had a less homogeneous coverage of Bindzil particles. Moreover, the Bindzil particle crust remained intact even after exposure to ultrasonication, which suggests that attraction between silica and PES is unlikely to be due to electrostatic forces only. Deposition of Bindzil from water (PESBiW) resulted in clusters of Bindzil particles inside the pore cavities rather than at the polymer surface. The PES-membranes, where silica growth had taken place directly onto the membranes (PESSt), were only partially covered with a silica crust as observed with SEM (see Figure 3.4).

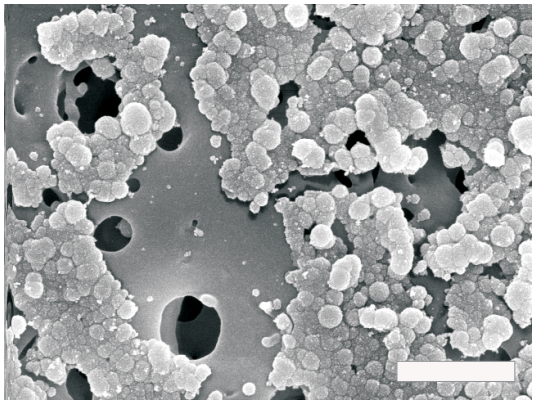

Figure 3.4. SEM picture of PES membrane PESSt. The membrane is only partially covered silica, which has been grown directly onto the membrane. The scale bar corresponds to 1 μm.

After thiol-functionalization and addition of gold particles, the color of the PES-BiEt2 membrane had become homogeneously purple whereas the PESSt membrane was indeed purple, but the color was less homogeneous, which can be explained by the less homogeneous silica layer and therefore empty regions without SH-groups. In both cases, the color of the membrane remained the same after several days in continuously refreshed water. The TEM-picture in Figure 3.5 show the PESBiEt2 full of single gold particles attached to the Bindzil crust.

It should be noted that the reaction time for MPTMS with the silica covered filters had to be longer than for the other particles and grains mentioned in this paper. The fast method to let MPTMS react with the silica surface by partial removal of ammonia and solvent was not applicable for the filters.

Functionalization of Stöber-silica

The reduction of $HAuCl_4$ in the presence of MPTMS-coated silica spheres resulted in silica spheres covered with gold particles with a diameter of 5-10 nm (see Figure 3.6). We observed that using 0.1 M $NaBH_4$ resulted in gold nanoparticles which were smaller and less polydisperse than when lowering the concentration of $NaBH_4$ to 0.01 M.

After several cleaning steps, the homogeneous sediment of particles remained colored, in contrast to the sample with non-modified silica, for which the sediment became white again as the free gold particles were removed. The silica-gold particles form colored, stable dispersions, which crystallize upon sedimentation. All dispersions remained stable for a long period of time and sedimented particles could easily be redispersed at least 6 months after preparation. Surprisingly, the gold covered silica particles can be coated with silica by using them as seeds in a Stöber synthesis (see Fig. 3.6), something which is not possible on pure gold surfaces, due to gold's low affinity for silica [86, 87]. Very

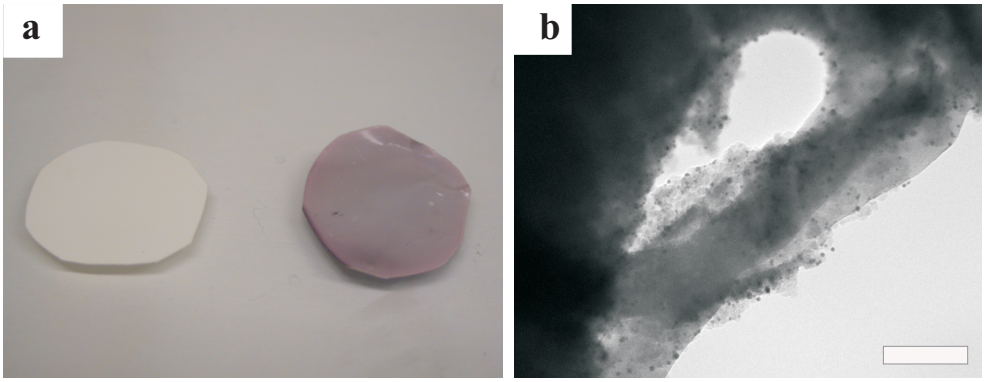

Figure 3.5. (a) Photograph showing pieces of the thiol-functionalized Bindzil-covered PES-membrane ($d \sim 2$ cm) before (left) and after (right) being soaked in a gold dispersion. (b) TEM picture of the thiol-functionalized Bindzil-covered PES membrane clearly showing the silica nanoparticles covering the polymer branches and the gold nanoparticles (higher contrast) attached to the silica. The scale bar corresponds to 100 nm.

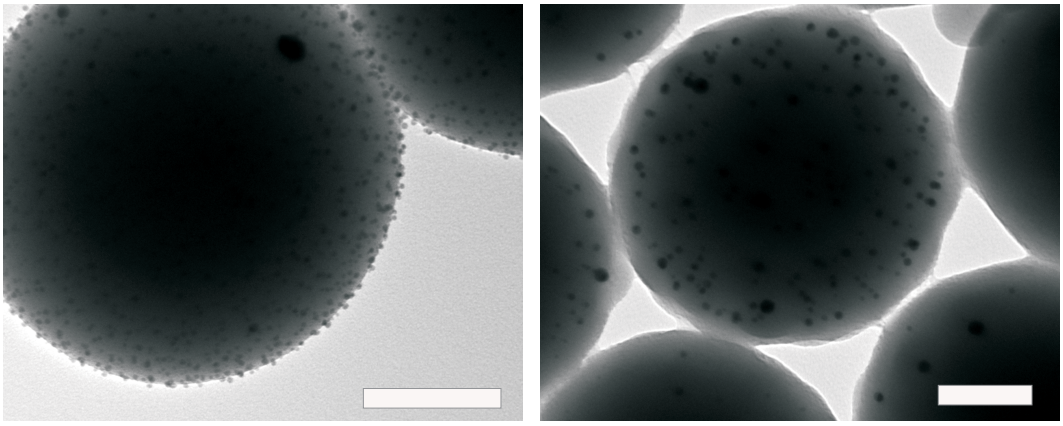

Figure 3.6. TEM pictures of silica-gold composite particles prepared via nucleation and growth of gold nanoparticles in the presence of thiol-functionalized Stöber silica (left) and after coating these composites with a 20 nm silica layer (right). The scale bars correspond to 100 nm.

likely, newly formed silica nucleates on the silica surface in between the gold particles such that these are eventually capped by further deposition of silica.

We have previously shown that magnetic particles of cobalt ferrite and maghemite can be irreversibly attached to thiol-functionalized silica particles and subsequently coated with a silica layer [46] (see also Chapter 2). Here it is shown how multilayer-structure type of composite particles can be prepared, by functionalizing the outer silica shell of such magnetic silica colloids and using it as seeds for synthesis of gold nanoparticles. The resulting gold decorated magnetic silica particles are shown in Fig. 3.7.

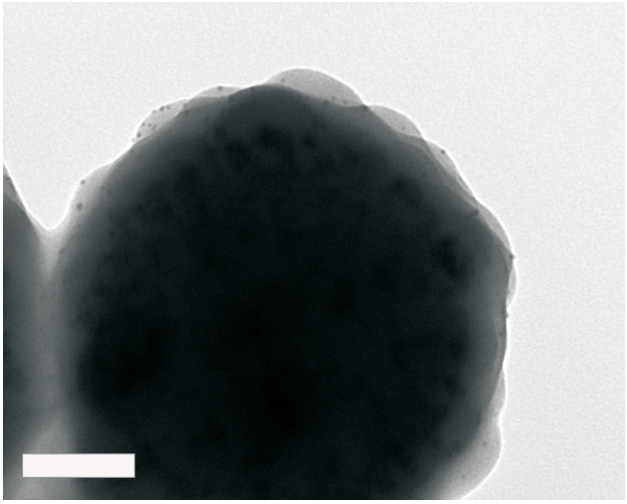

Figure 3.7. TEM picture of the magnetic silica particles (SibCs, $R = 217$ nm) coated with MPTMS and covered with gold particles. The rough silica surface is due to the embedded cobalt ferrite particles, around which new silica has nucleated and grown. The scale bar corresponds to 100 nm.

Functionalization of porous silica grains

The procedure for grafting Stöber-silica with MPTMS could be applied to porous glass grains as well as to SBA-15 without any additional modification. After synthesizing gold nanoparticles in the presence of the silica grains and subsequent rinsing, a clear difference could be seen between the grains that had and the grains that had not been grafted with thiol groups. The thiol-functionalized grains remained colored, while the non-modified grains became white again after rinsing with water. TEM pictures (see Fig. 3.8) show that also the surface of the pores in the modified CPG grains is covered with small ($R \sim$ 1-2 nm) gold particles.

3.4. Conclusions

We have demonstrated that the method described in Chapter 2 to functionalize silica colloids with thiol groups can be applied to a variety of silica particles and structures, including commercial silica nanoparticles and (magnetizable) Stöber silica as well as silica structures provided by porous glasses and novel polymer-templated silica membranes. Commercially available membranes of polyethersulfone can be encapsulated in a crust of silica, obtained by addition of colloidal silica particles, which can form a dense layer around the polymer. The functionalization of silica particles and structures with thiol-groups allows for irreversible binding of metal(oxide) particles from a solution, as demonstrated here for gold as well as $CoFe_2O_4$ nanoparticles. The functionalization step generally includes transfer of the particles or grains to a mixture of ethanol and ammonia and addition of MPTMS followed by heating and removal of solvent for a

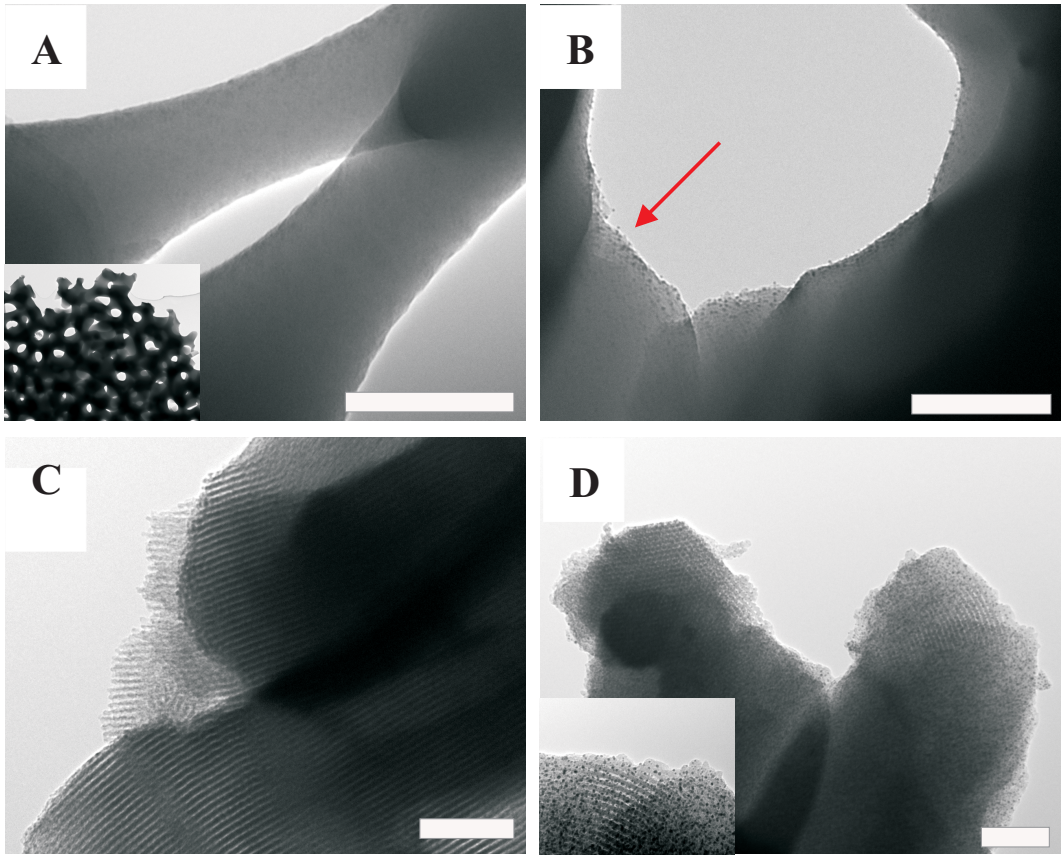

Figure 3.8. TEM pictures showing the results of synthesis of gold particles in the presence of thiol-functionalized (a-b) and not thiol-functionalized (c-d) controlled porous glasses. In the presence of thiol groups, the surface of the pores are covered with small (R ∼1 nm) gold particles. The scale bars correspond to 100 nm.

fast reaction. For the smallest ($R \sim 6$ nm) silica particles, the grafting procedure must be slightly modified to avoid gelation. This includes purification from soluble silicates before transferring the particles from water to ethanol and thereafter not exceeding pH ∼8.5. Moreover, for the silica covered polymer membranes, longer reaction time is needed during the functionalization step. The reaction is in this case slowed down by lowering the temperature from 80°C to 50°C and not removing solvent. Gold nanoparticles can be synthesized directly onto the surface of the various types of functionalized silica in a convenient one-pot synthesis step to obtain a wide range of silica-gold composites. It is worth noticing here that the silica colloids remain stable in dispersion throughout this step, resulting in a dispersion of single gold-decorated particles. Since these silica systems all have a large surface-to-volume ratio, surface modification of such materials with -SH groups and chemical adsorption of metals and metal oxides can be useful in for instance separation processes.

Acknowledgements

Eka Chemicals are acknowledged for providing the Bindzil silica sols. Fouad Soulimani is thanked for assistance with the IR-measurements, Stefano Sacanna for making SEM-pictures and Johanna Schütz-Widoniak and Ana Ürmenyi for many helpful discussions. TEM pictures were made at the EMU (Electron Microscopy Utrecht) facility.

4

Magnetic Silica Particles for Catalysis

Abstract

Monodisperse magnetizable colloidal silica particles in a stable dispersion have been functionalized with a homogeneous catalyst: a PCP-pincer Pd-complex. In a proof-of-principle experiment we demonstrate the catalytic activity of the colloids in a C-C bond formation reaction. Advantages of the magnetic silica carriers are the large surface-to-volume ratio and the easy recovery by magnetic separation. After magnetic separation, the catalyst-loaded particles are readily redispersed for further use.

4.1. Introduction

Colloidal silica is widely used in industrial applications as well as for fundamental research purposes. The preparation of monodisperse silica particles and the silica coating of other inorganic colloids are well-documented and the silica particle surface is well suitable for chemical surface modification (see for instance [3, 48, 50]). Catalysis is an indispensable process in the chemical industry both from an economical and an environmental point of view. Production of various chemicals ranging from pharmaceuticals to polymers involves the use of transition metal catalysts [88, 89]. These catalytic systems are generally divided into two groups: homogeneous (catalyst in the same phase as the reactants) and heterogeneous (catalyst on a solid support) catalysts. Heterogeneous catalytic systems have the advantage that the catalyst can be recovered after completion of the reaction. On the other hand, a homogeneous catalytic system has a higher reactivity and selectivity. To combine these advantages, homogeneous catalysts are usually immobilized on supports such as mesoporous silica [90–93]. Silica has the advantage that it is inert and hence chemically and thermally stable under most of the conditions under which catalysts are operating, and it can be readily separated from the reaction mixture. Depending on the surface area and pore size of the silica, it can have a restricted approach of the reactant molecules to the catalyst, thereby reducing the reactivity and altering the selectivity. By using colloidal particles (which have a high surface-to-volume ratio) as a support, homogeneous catalysts can be dispersed in a reaction mixture and at the same time be separated from a solution by sedimentation [94, 95]. By introducing support particles with induced magnetic properties, the separation can be improved and the magnetic support particles can be fixed at the wall of the reaction vessel while the solution is decanted by applying a magnetic field [26,33]. For efficient recycling of the catalyst, the support particles should be magnetic enough to be collected with a small permanent magnet and easily be redispersed in the reaction medium after removing the magnet so that the catalysis can be continued. Moreover, the support particles must be chemically inert under the conditions where the catalysis takes place. Magnetic particles have previously been immobilized on mesoporous silica structures for catalytic purposes [96]. Single magnetic particles with a silica shell have also been reported on as support particles in catalysis [26,95], but such particles require high fields for efficient magnetic separation from solution, which is a severe drawback. Here we report on the preparation of magnetic silica particles (150 nm radius) consisting of monodisperse silica cores covered with maghemite nanoparticles and an outer silica shell (see Figure 4.1), grafted with a modified organometallic catalyst based on a PCP-pincer palladium complex [97, 98]. This complex is known to catalyze the aldol condensation reaction between benzaldehyde and methyl isocyanoacetate to produce oxazolines (see Figure 4.5) [99].

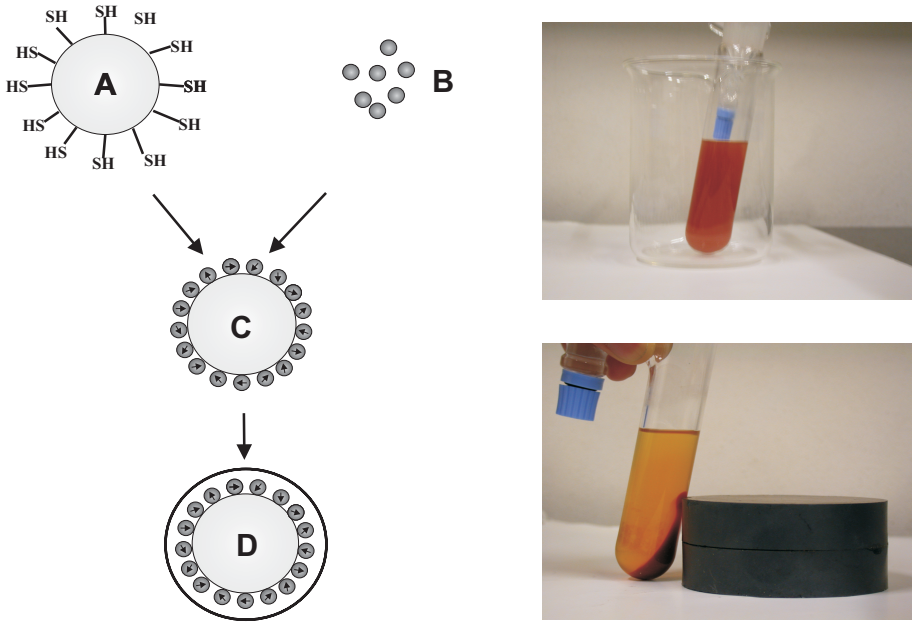

Figure 4.1. 1 Left: The stepwise synthesis of magnetic silica: Thiol-functionalized Stöber silica (A) is mixed with maghemite (B) to obtain silica cores with magnetic particles (C) onto which silica can be precipitated to form magnetic core-shell particles with an outer silica shell (D). Right: The particles in dispersion after surface modification with the PCP-Pd complex (top) and collected with a magnet during the purification from unreacted PCP-Pd complex (bottom).

4.2. Experimental

Synthesis of magnetic silica colloids

The magnetic silica particles used in this work were prepared according to the scheme in Figure 4.1, following the procedure which was described in more detail in Chapter 2 [46]. Silica cores ($R_{TEM} = 135$ nm, $R_{SLS} = 152$ nm) were prepared by hydrolysis and condensation polymerization of tetraethoxysilane [1] and grafted with a thiol-containing silane coupling agent [48]. Maghemite particles were prepared according to the classic coprecipitation method of Massart *et al.* [42, 43] and added to the dispersion of thiol-functionalized silica particles, leaving the mixture gently shaken overnight. Excess maghemite was removed by repeated centrifugation. The silica cores covered with maghemite particles were coated with a thin outer silica layer by applying the same seeded-growth synthesis method as for the silica cores, now using the magnetic core-shell particles as seeds. Small aliquots of tetraethoxysilane were added to the reaction mixture while using ultrasonication to prevent aggregation of particles during the silica growth. The silica-coated magnetic core-shell particles were purified by repeated centrifugation and redispersion in ethanol.

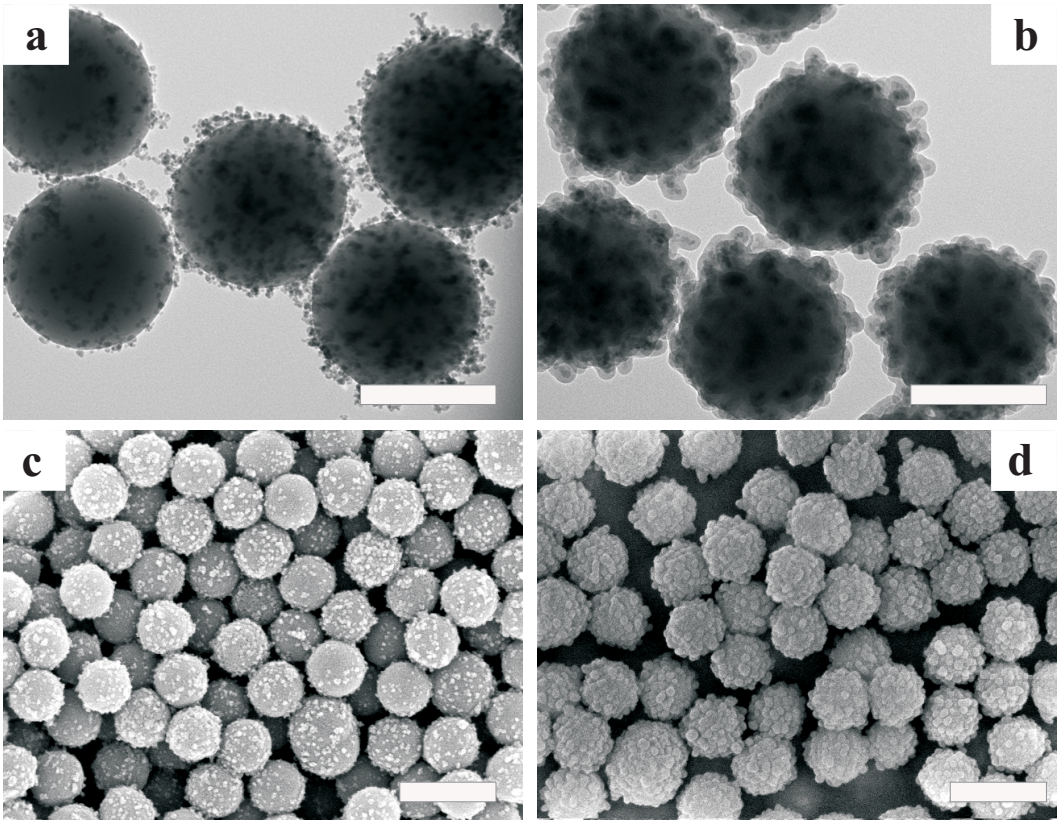

Figure 4.2. TEM (top, scale bar represents 200 nm) and SEM (bottom, scale bar represents 500 nm) pictures of maghemite-covered silica cores before (a,c) and after (b,d) silica coating.

The size as well as the internal morphology of the particles was monitored throughout the stepwise preparation using transmission (TEM) and scanning (SEM) electron microscopy (Figure 4.2). As a complement, static light scattering (SLS) contrast variation experiments were used for size determination (Figure 4.3) [71]. Light scattering measurements are performed directly in dispersion whereas conventional TEM is performed on a substrate with dry particles, which consequently yields an underestimate of the particle size. The intersection point of the angular intensity profiles in Figure 4.3 gives the total radius of the particles from $k_m R = 4.4935$ as known from scattering theory of concentric inhomogeneous particles [71] as discussed in more detail in Chapter 7. Additionally, such a well-defined intersection point confirms the presence of non-aggregated particles in dispersion with a low polydispersity. This is valuable information, which cannot always be obtained from TEM due to drying effects. Finally, magnetization measurements were performed on a sample of dried magnetic silica. The absence of hysteresis confirms that the particles are superparamagnetic.

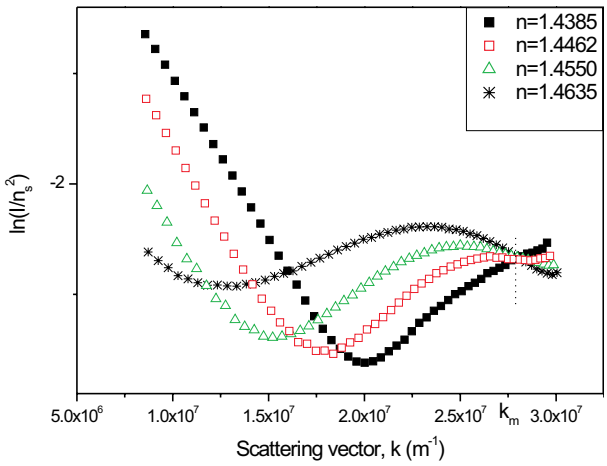

Figure 4.3. Results from static light scattering measurements performed on magnetic silica particles, applying optical contrast variation. From the sharp intersection point at $k_m = 2.77 \times 10^7\ m^{-1}$ a total particle radius of 162 nm is obtained in good agreement with the radius obtained from TEM (153 nm). The sharpness of the intersection point and the agreement with the TEM-radius of the particles indicates monodisperse non-aggregated particles (see Chapter 7).

Immobilization of the PCP-pincer Pd-complex onto magnetic silica particles

PCP-pincer palladium complexes are known for their catalytic activity in C-C bond formation reactions [99]. A modified version of this complex (**1**, see Figure 4.4), which has a triethoxy-silane group useful for tethering it to the silica, was prepared previously [100]. This complex was immobilized onto the magnetic silica by a standard process in which a mixture of the magnetic silica and complex **1** was heated at 90 °C in toluene for 20 h. The modified silica was separated from the solution by using a small permanent magnet as shown in Figure 4.1. The supernatant was removed and the silica was washed with dichloromethane to remove non-immobilized complex **1**. In each washing step, the silica was separated with a magnet. The functionalized silica was then suspended in hexane and treated with 1,1,1,3,3,3-hexamethyldisilazane (HMDS) to cap remaining unreacted surface silanol groups with a trimethylsilyl functionality. The resulting magnetic silica particles, loaded with PCP-Pd complex, will be denoted here as MagSi**3**.

Elemental (ICP) analysis of MagSi**3** showed palladium content was 0.14 wt%, which corresponds to 0.0135 mmol PCP-pincer Pd-complex **1** per gram MagSi**3**. The molar ratio of phosphorus to palladium was found to be about 2.7. It should be noted that the presence of these elements was analyzed after thoroughly rinsing the magnetic silica particles, which would have removed any free molecules. Based on the palladium content, the surface coverage was estimated to be 1.1 PCP-pincer Pd-complex molecules per nm^2 MagSi**3** surface. However, this is likely to be an overestimate, since it was

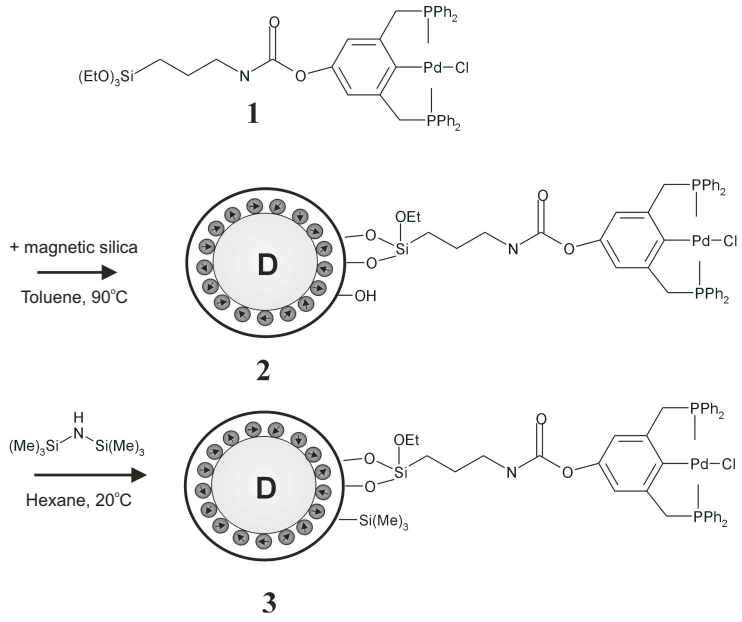

Figure 4.4. Scheme of the immobilization of catalytic PCP-pincer Pd-complex **1** onto magnetic silica particles (D). The resulting catalytic magnetic particles will be denoted here as MagSi**3**.

assumed that the particles are spherical and that the catalyst molecules form a single monolayer on the particle surface.

Subsequently, the MagSi**3** particles were tested in catalysis. As a test reaction, the aldol condensation reaction between benzaldehyde and methyl isocyanoacetate (see Figure 4.5) was chosen.

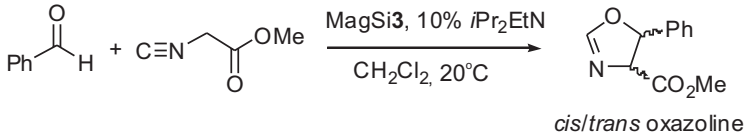

Figure 4.5. Aldol condensation reaction between benzaldehyde and methyl isocyanoacetate to oxazoline catalyzed by MagSi**3**.

In this experiment, 1.6 mmol of each benzaldehyde and methyl isocyanoacetate were reacted in the presence of the base N,N-diisopropylethylamine, *i*Pr2EtN (10%, 0.16 mmol). The amount of MagSi**3** catalyst used was 100 mg, which corresponds to about 1.35 mol of palladium and which gives a catalyst concentration of 0.08 mol%. For comparison, a blank reaction was performed using all the above reagents at the same concentration but without the MagSi**3** catalyst. Results of the catalysis and blank reactions are shown in Figure 4.6. It is clear that the reaction with MagSi**3** has the higher activity (TOF = 16 h^{-1} at 40 % conversion) over the background reaction. When the silica was sedimented using a magnet, the progress of the reaction decreased to

approximately that of the background reaction, whereas the reaction after redispersing the magnetic silica proceeded with the same reaction rate as before removal of the catalyst.

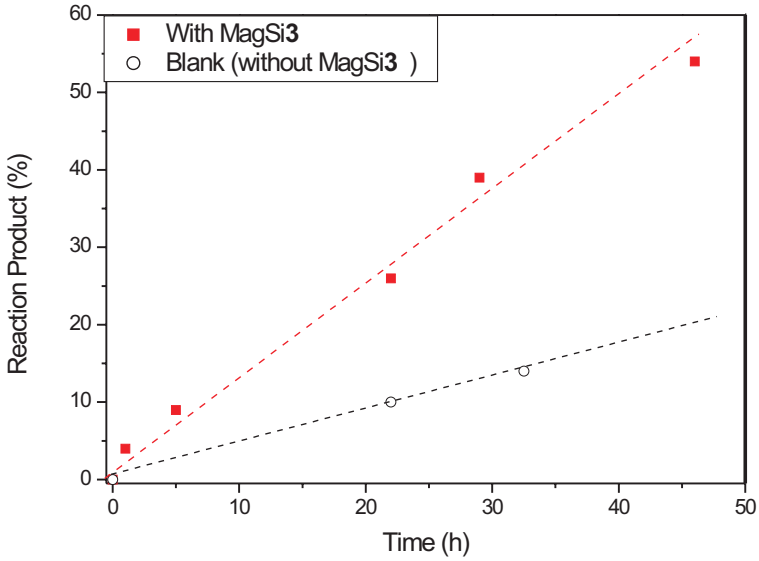

Figure 4.6. Kinetic profiles of the aldol reaction catalyzed by MagSi**3** and the corresponding blank reaction.

These experiments indicate that the observed acceleration is due to the PCP-Pd based activity and that this is associated with the magnetic silica. These results demonstrate the heterogeneous nature of the catalyst. Here the effect on the reaction rate is rather modest and mainly serves as a proof-of-principle. The catalytic activity can be improved by increasing the amount of catalytic particles and/or by decreasing the size of the magnetic silica particles to provide more surface area.

4.3. Conclusions

In summary, monodisperse magnetic silica particles have been prepared and grafted with a homogeneous catalyst, in this case a PCP-pincer Pd-complex. In this way the catalyst can be separated from a reaction mixture in the relatively low magnetic field gradient from a small laboratory magnet. Furthermore, we have provided a proof-of-principle of how these catalyst loaded magnetic silica particles can be used in a versatile C-C bond formation reaction. Moreover, after magnetic recovery, the magnetic silica particles with immobilized catalyst can readily be redispersed for further use. The small size of the support particles provides a large surface-to-volume ratio, which makes a large amount of immobilized catalyst available for catalysis per volume magnetic silica.

The results presented here are promising for future work on particle-supported catalysts. The silica chemistry gives the possibility to attach a large variety of catalytic compounds to these magnetic particles and provides interesting possibilities for use in

cascade reactions [33] in which several reaction steps can be catalyzed by immobilizing several different catalysts onto the magnetic silica. In a more detailed study of the catalytic properties, the particles should be employed in catalysis several times and the structure of the PCP-Pd complex should be investigated prior to and after catalysis to ensure the stability of the catalyst.

Acknowledgements

This work presented in this chapter was performed in cooperation with Nilesh Mehendale, Prof. Dr. Bert Gebbink and Prof. Dr. Gerard van Koten at the Department of Organic Chemistry and Catalysis, Utrecht University. The research was partially financially supported by STW.

5

Measurement of the Particle Magnetic Dipole Moment of Magnetizable Composite Silica Spheres

Abstract

The magnetic properties of magnetic silica microspheres have been investigated by measuring magnetization curves and the complex magnetic susceptibility as a function of frequency and field amplitude. The magnetic moment of the microparticles is compared to the number and magnetic moment of embedded cobalt ferrite nanoparticles. The microspheres would have a permanent magnetic dipole moment even if the nanoparticles were oriented at random, because the average magnitude of the vector sum of randomly oriented unit vectors is non-zero. The magnetic moment increases after treatment in a saturating magnetic field, because once the field is removed, the dipole orientations do not relax to the initial random distribution.

5.1. Introduction

Magnetic microspheres used in biomedical applications generally do not have a permanent magnetic moment [28]. The particles are magnetized in an external magnetic field and lose their magnetization when the field is removed. In Chapter 2 of this thesis, a method was developed to synthesize silica microspheres with embedded cobalt ferrite nanoparticles. At room temperature a large fraction of the magnetic moments of the nanoparticles is blocked and, as a result, the microspheres have a permanent magnetic moment. Such particles can be used in fundamental studies of the rotational diffusion of colloidal spheres by measuring the complex magnetic susceptibility, at alternating fields in strength comparable to the earth magnetic field, *i.e.*, too weak to exert a significant torque on the particles. Here it will be shown that the interaction of the particles with the field is comparable to the thermal energy and that the re-orientation of the particles with the applied magnetic field is diffusive. This magnetic method to study rotational dynamics (see Chapter 6) has several advantages compared to previously used optical methods such as depolarized dynamic light scattering (DDLS) [101], time-resolved phosphorescence anisotropy (TPA) [102] or polarized fluorescence recovery after photobleaching (pFRAP) [103]. The magnetic measurements are not restricted to low particle concentrations or solvents with a specific index of refraction since the particles do not have to be optically matched with the surrounding medium. Moreover, problems such as luminescence-reabsorption effects are avoided [102, 103] and at a particular concentration, it is possible to obtain the distribution of diffusion coefficients directly rather than just one average value.

For a proper interpretation of rotational diffusion experiments using a magnetic technique, as presented in Chapter 6, it is important that the magnetic properties of the colloidal particles can be quantified. The aim of the present work is to provide this quantification for cobalt ferrite-doped silica microparticles by analyzing three types of magnetic measurements: magnetization curves, complex magnetic susceptibility spectra in the low-field limit, and the field-amplitude dependence of the complex magnetic susceptibility in the low-frequency limit. The magnetic dipole moment of microparticles in zero field is determined before and after exposure to a strong magnetic field to investigate whether the dipole moment of the colloids can be permanently increased.

The outline of this chapter is as follows: In Section 5.2, the theoretical background of magnetization measurements and complex magnetic susceptibility spectroscopy is reviewed. In Section 5.3, the technical equipment, preparation of the magnetic particles and the experimental procedures are described, and in Section 5.4, the results of the measurements are presented. In Section 5.5, the magnetic properties of the particles and the dispersions are discussed.

5.2. THEORY

Magnetization curves

The magnetization M measured as a function of the applied magnetic field H is investigated for (a) dispersions and dry powder of cobalt ferrite nanoparticles and (b) dispersions and dry powder of the silica microspheres with embedded cobalt ferrite. The equations involved in the analysis of the magnetization curves are presented below.

The distribution of magnetic dipole moments of the nanoparticles can be determined from the magnetization curve of dilute nanoparticle dispersions, for which dipole-dipole interactions have a negligible effect. In line with size distribution determined with electron microscopy [4], it is assumed that the magnetic diameter, d_m, follows a lognormal distribution:

$$P(d_m) = \frac{1}{\sigma d_m \sqrt{2\pi}} exp[\frac{-ln^2(d_m/d_0)}{2\sigma^2}] \tag{5.1}$$

Here, $P(d_m)$ is the probability density function, σ^2 is the variance, and d_0 is the magnetic diameter at the maximum of the distribution. The dipole moment, μ_{np} of a single magnetic nanoparticle is given by

$$\mu_{np} = \frac{\pi}{6} d_m^3 m_s, \tag{5.2}$$

where m_s is the material-dependent saturation magnetization per unit volume (425 kA/m for cobalt ferrite [10]). It is assumed that all nanoparticles have a single magnetic domain. The shape of the magnetization curve of monodisperse nanoparticles in dispersion is determined by the Langevin equation:

$$M = M_s L(\alpha) = M_s[coth(\alpha) - \frac{1}{\alpha}], \tag{5.3}$$

where M_s is the saturation magnetization and

$$\alpha = \frac{\mu_0 \mu H}{k_B T}. \tag{5.4}$$

Here, $k_B T$ is the thermal energy and $\mu_0 = 4\pi \cdot 10^{-7}$ JA^{-2}m^{-1} the magnetic permeability of vacuum. For nanoparticles with a lognormal distribution at low concentrations where interactions are negligible, the magnetization of the dispersion at field H is given by:

$$M = M_s \frac{\int_0^\infty P(\mu)\mu L(\alpha(\mu, H))d\mu}{\int_0^\infty P(\mu)\mu d\mu}, \tag{5.5}$$

with the function $L(\alpha)$ defined via (5.3); $P(\mu)$ is the probability density function for the particle dipole moment, μ. The mean magnetic diameter and the width of its distribution are obtained from a fit of Equation 5.5 to the magnetization curve of the nanoparticle dispersion. The permanent magnetic moment of microparticles cannot be obtained in the same way, since they also have an induced dipole moment. Alternative approaches are discussed in the next two sections.

If individual magnetic moments are blocked inside the cobalt ferrite nanoparticles, magnetization curves of dry nano- or microparticles will display hysteresis. The time scale for the rotation of the magnetic moment inside the nanoparticles, so-called Néel relaxation, strongly depends on the magnetic particle volume, V_m: [38]

$$\tau_N = \tau_0 \cdot exp[\frac{KV_m}{k_B T}], \tag{5.6}$$

where $\tau_0 = 10^{-9}$ s and K is the anisotropy constant (200 kJm^{-3} for cobalt ferrite [38]).

According to (5.6), cobalt ferrite nanoparticles with a diameter of 10 nm or more have a blocked orientation of the magnetic dipole moment at room temperature ($\tau_{\mathrm{N}} > 100$ s).

Complex magnetic susceptibility spectra in the low-field limit

The permanent magnetic moment as well as the hydrodynamic radius of magnetic microparticles can be determined by measuring the frequency-dependent complex magnetic susceptibility of a dispersion of the particles [104]. If the particles have a permanent magnetic moment, the real part of the magnetic susceptibility will have a plateau value in the low frequency limit and will decrease with increasing frequency when approaching the frequency of Brownian rotation of the microparticles (see Figure 5.1) to finally decrease to zero in the high frequency limit. At the characteristic frequency, the imaginary part of the susceptibility spectrum will have a maximum. With this technique, the permanent magnetic moment of the microparticles is separated from other contributions to the susceptibility, such as the field-induced alignment of nanoparticle dipoles that are not blocked or of free nanoparticles, which are not embedded in microparticles. Néel and Brownian relaxation of single nanoparticles occur at much higher frequencies than the frequency of Brownian rotation of the microspheres.

In the limit of low field and low frequency, the dimensionless magnetic susceptibility $\chi = M/H$ of a colloidal dispersion consists of two contributions:

$$\chi = \chi_{LF} + \chi_{HF} \tag{5.7}$$

The contribution χ_{LF} is present only at frequencies low enough for the orientation of the permanent dipole moment of microspheres to respond to the weak alternating external

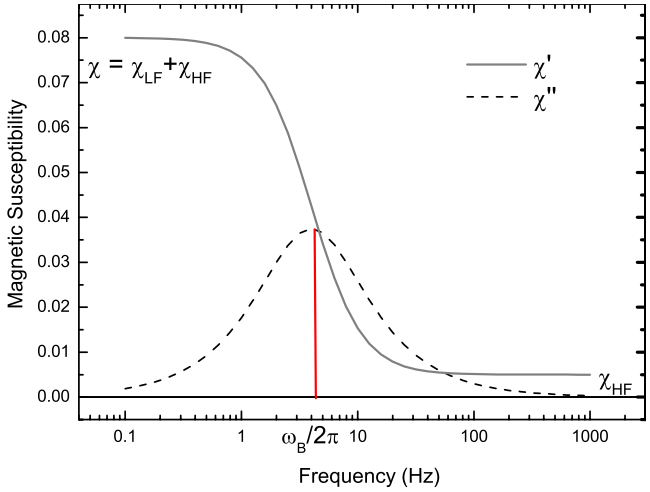

FIGURE 5.1. Calculated complex magnetic susceptibility spectrum for microspheres with a permanent magnetic dipole moment and a hydrodynamic radius, $R_h \sim 200$ nm in ethanol (solvent viscosity $\eta = 1.074$ mPa s at $T = 298.15$ K [105]). At the characteristic frequency for Brownian rotation, ω_B, of these particles, 4 Hz, the real component χ' has the highest frequency dependence and the imaginary component χ" has a maximum (5.10-5.12). The dipole moment of the microspheres can be obtained from the susceptibility in the low frequency limit, χ_{LF} minus the susceptibility in the high-frequency limit, χ_{HF}. The latter is proportional to the number of nanoparticles with non-blocked dipoles.

magnetic field by Brownian rotation:

$$\chi_{LF} = \frac{N_{mp}}{V}\frac{\mu_0(\mu_{mp})^2}{3k_BT} \tag{5.8}$$

Here, N_{mp} is the number of composite microparticles, V is the sample volume, and μ_{mp} is the permanent magnetic moment of the microparticles. Equation 5.8 is obtained by performing a Taylor expansion of (5.3). From (5.8), measurement of the initial susceptibility of a sample with a known concentration N_{mp}/V allows calculation of μ_{mp}. The second contribution, χ_{HF}, is present at higher frequencies too where the contribution χ_{LF} of the microspheres has been lost. This is due to nanoparticles that respond individually, by Néel relaxation or Brownian rotation in the solvent. The characteristic frequency determined by Brownian rotation of particles in a solvent is given by [106, 107]:

$$\omega_B = 2D_r = \frac{k_BT}{4\pi\eta R_h^3}, \tag{5.9}$$

where D_r is the rotational diffusion coefficient, η is the viscosity of the solvent, and R_h is the hydrodynamic radius of the spherical particles. At this frequency, the in-phase, real component χ' of the complex susceptibility has the highest frequency dependence and the out-of-phase, imaginary component χ'' has an extremum [106, 107]:

$$\chi(\omega) = \chi'(\omega) - i\chi''(\omega) \tag{5.10}$$

$$\chi'(\omega) = \chi_0 \frac{\omega_B^2}{\omega_B^2 + \omega^2} \tag{5.11}$$

$$\chi''(\omega) = \chi_0 \frac{\omega_B \omega}{\omega_B^2 + \omega^2} \tag{5.12}$$

Here, $\omega = 2\pi f$ is the angular frequency in s^{-1} with the cycle frequency f in Hz. From (5.9), for a solvent viscosity of $\eta \approx 1$ mPa s at $T = 298$ K, the characteristic frequencies for the Brownian rotation of composite particles with a radius of 100-1000 nm is in the range 0.05-50 Hz, whereas that of nanoparticles of 1-10 nm in radius is in the 0.05-50 MHz range, 3 to 6 orders of magnitude higher. The contributions of microparticles and single nanoparticles dipoles can therefore clearly be separated in a complex magnetic susceptibility spectrum.

Field-amplitude dependence of the magnetic susceptibility in the low-frequency limit

A second approach to determine the permanent magnetic dipole moment of microparticles is from the field-amplitude dependence of the magnetic susceptibility in the low-frequency limit. The dimensionless magnetic susceptibility χ is given by:

$$\chi = \frac{M}{H} \sim \frac{M_s L(\alpha)}{H}. \tag{5.13}$$

noindent In the low-field limit the Langevin equation (5.3) is linear:

$$L(\alpha)_{H \to 0} = \frac{\alpha}{3}, \tag{5.14}$$

and the initial magnetic susceptibility, χ_0, is independent of H. Beyond the low-field limit, χ starts to change. The deviation from χ_0 can be expressed by taking the ratio of M/H with the low-field limit value. Assuming that the field is still too low to change the magnetic moment of the microspheres or to induce dipolar structures, the following expression is obtained:

$$\frac{\chi}{\chi_0} = \frac{L(\alpha)}{\alpha/3} = \frac{3}{\alpha}[coth(\alpha) - \frac{1}{\alpha}] \tag{5.15}$$

When the microspheres have a large permanent magnetic moment, the Langevin equation deviates from the linear approximation in (5.14) at fields well below 1 kA/m. The magnetic moment can be calculated from this deviation from linear behavior by fitting the expression in (5.15) to a plot of χ/χ_0 versus the field amplitude H measured at constant temperature. From the obtained value for α (5.4) the dipole moment μ_{mp} of the microspheres can be calculated without knowing the concentration of particles in the measured dispersion.

5.3. Experimental

Magnetic silica colloids were prepared by adding an aqueous ferrofluid of cobalt ferrite [45] or maghemite [44] nanoparticles to thiol-functionalized colloidal silica spheres (see Chapter 2). The resulting core-shell microspheres were coated with an outer silica shell, and the surface was grafted with 3-(trimethoxysilyl)propyl methacrylate (TPM) to stabilize the particles [48]. The particle dispersions were purified extensively by sedimentation and redispersion in ethanol. Three dispersions of magnetic microspheres were studied (see Table 5.1): two silica-cobalt ferrite dispersions with different microparticle sizes, where a large fraction of the dipole moments of the nanoparticles is blocked, as well as one dispersion of silica-maghemite particles.

Table 5.1. Characterization parameters of the magnetic silica dispersions.

	Sample 1	Sample 2	Sample 3
Nanoparticles	cobalt ferrite	cobalt ferrite	maghemite
R_{TEM} (nm) [a]	187 ± 34	409 ± 9	154 ± 11
ρ_p (g/mL) [b]	2.45	2.14	-
N_{mp}/V (m^{-3}) [c]	$3.53 \cdot 10^{17}$	$1.32 \cdot 10^{17}$	-

[a] Particle radius obtained from analysis of TEM images.
[b] Particle mass density.
[c] Particle number concentration.

The particles were characterized with transmission and scanning electron microscopy (TEM and SEM). The complex magnetic susceptibility of dispersions 1 and 2 was measured before and after the particles had been exposed to a homogeneous field of 2 T for 1 h, using a Bruker BE 25v electromagnet. Magnetization curves of the samples and the corresponding nanoparticles in dispersion as well as in powder form were measured with a Micromag 2900 alternating gradient magnetometer (Princeton measurements corp.). The dispersion samples were contained in rectangular glass sample holders of 4 mm $\times$ 4 mm $\times$ 0.4 mm with the square sides parallel to the magnetic field direction to minimize demagnetization. The dry powders were fixed to a thin glass slide of 7 mm $\times$ 3 mm with adhesive tape.

Complex magnetic susceptibility measurements were performed using a setup described in detail elsewhere [108]. It is a new version of an earlier setup [106] now with higher sensitivity and possibility to measure at lower frequencies. In brief, the setup is a differential transformer with two multilayered cylindrical copper coils: a primary layer through which an applied alternating current flows and a secondary layer in which an alternating voltage is induced. The key idea of the setup is to use secondary coils with a maximized number of layers beyond which the signal would no longer increase but drop due to capacitance and absorption effects. An AC current is applied to the primary coils using a Yokogawa FG120 function generator and the voltage induced in

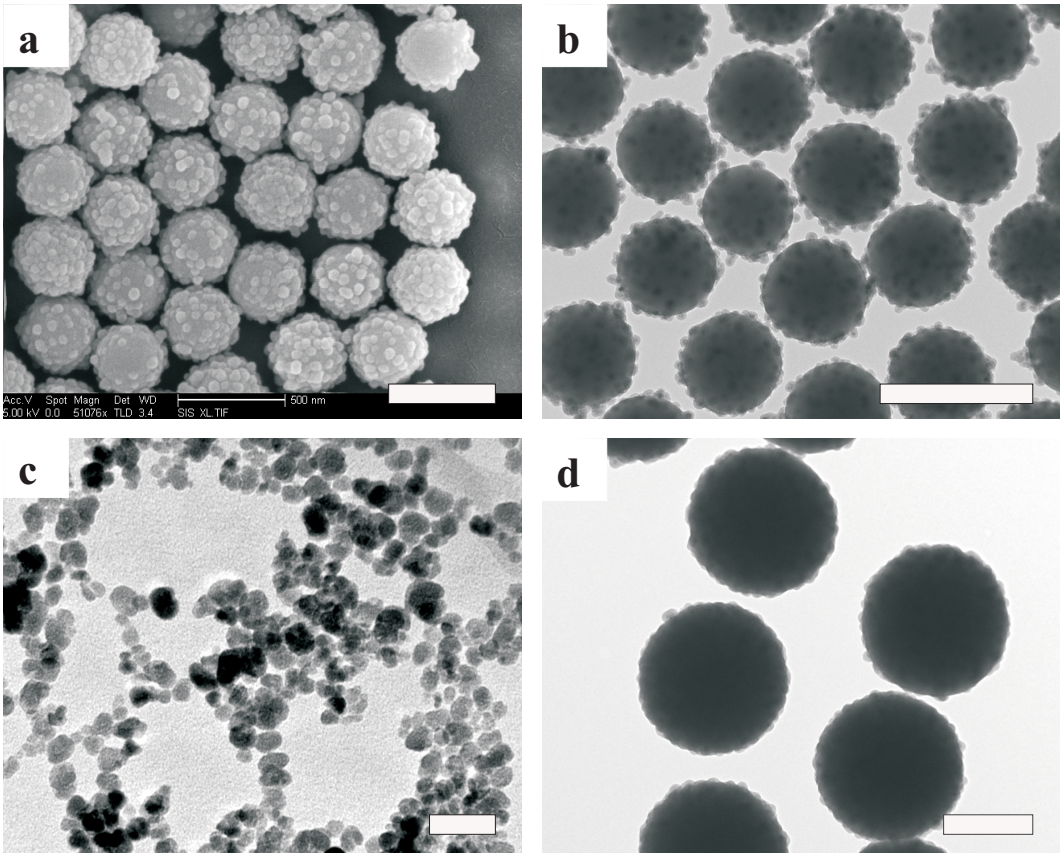

Figure 5.2. Electron microscopy pictures of the studied particles: (a) SEM and (b) TEM picture of $R \sim 200$ nm silica-cobalt ferrite microspheres (Sample 1), (c) TEM picture of the cobalt ferrite nanoparticles and (d) TEM picture of $R \sim 400$ nm silica-cobalt ferrite microspheres (Sample 2). In the TEM pictures, the cobalt ferrite nanoparticles are visible as dark spots inside the silica matrix and in the SEM picture, the silica-covered cobalt ferrite nanoparticles are seen as bright bulges on the surface of the silica core. The scale bars represent 500 nm (a, b, d) and 50 nm (c).

the secondary coils is measured using a 7265 Signal recovery differential lock-in amplifier in the 2 mHz to 1 kHz range. The colloidal dispersion of magnetic microparticles is contained in a cylindrical glass tube. When the magnetic sample is introduced in the coils, the change in the measured alternating voltage is proportional to the complex susceptibility of the sample. The amplitude of the alternating magnetic field used for the experiments presented here was relatively low, 57 A/m if not specified otherwise, to avoid changing the magnetic structure of the samples. Sample and coils were kept at a constant temperature of 295.5 K in a thermostatized and grounded box made of mu-metal for shielding from external low-frequency magnetic interference.

To calculate the magnetic dipole moment of the microspheres according to (5.8), the particle number concentration (N_{mp}/V) must be determined. A small amount of the

measured dispersions 1 and 2 with known weight, m_{disp} and volume, V_{disp} was dried to obtain the weight of dry particles, m_p. V_{disp} was obtained by measuring the height of the dispersion with a cathetometer inside a calibrated tube with a known volume-height relation. Together with the solvent density, $\rho_s = 0.789$ g/mL, the mass density, of the particles, ρ_p was calculated via:

$$\rho_p = \frac{m_p}{V_{disp} - \left(\frac{m_{disp} - m_p}{\rho_s}\right)} \tag{5.16}$$

The sample volume, V_{sample}, of the measured dispersion of sample 1 and 2 was obtained in the same way as described above. The number concentration of particles was obtained from:

$$\frac{N_{mp}}{V} = \frac{3\phi_m m_{disp}}{4\pi (R_{TEM})^3 \rho_p V_{sample}}, \tag{5.17}$$

where $\phi_m = m_p / m_{disp}$ is the mass fraction of particles and R_{TEM} is the physical radius of the particles obtained from TEM images.

5.4. Results

Magnetization curves

The magnetic moment of the cobalt ferrite nanoparticles can be determined from the magnetization curve of the particles in a dilute dispersion (Figure 5.3 a). A fit of the data based on (5.5) gives a magnetic moment of $1.61 \cdot 10^{-19}$ Am^2 with a diameter distribution width given by $\sigma = 0.51$ (Eqn. 5.1). A magnetization curve of the same nanoparticles but dry (Figure 5.3 b) clearly shows hysteresis, with a remanence M_r/M_s of 0.425. For the nanoparticles, a saturation magnetization of m_s= 240 kA/m is found (m = 0.27 mg, ρ_p = 4907 kg m^{-3} [38], M_s =$1.32 \cdot 10^{-19}$ Am^2). This is much lower than the m_s= 425 kA/m for cobalt ferrite as reported in literature [38], likely due to that cobalt ferrite nanoparticles prepared by coprecipitation have a non-magnetic iron oxide shell [45], which still has roughly the same mass density as cobalt ferrite [38,105]. With an average magnetic diameter of about 11 nm, a large fraction of the cobalt ferrite particles has a radius large enough for the dipole moments to be blocked at room temperature.

A practical difficulty when measuring a magnetization curve of the dispersed magnetic silica particles (Figure 5.3 c) is their sedimentation rate. This is already high in zero field (0.22 mm/hour) and is much enhanced in an external magnetic field. This problem is absent in the complex magnetic susceptibility measurements, where the magnetic fields are much lower. Large magnetic aggregates are formed that sediment rapidly while the magnetization curve is being measured. These large structures and the sediment lead to hysteresis, since Brownian relaxation is slowed down significantly. It was also observed that the remanence in the Sample 1 powder, M_r/M_s=0.305, is lower than for the pure

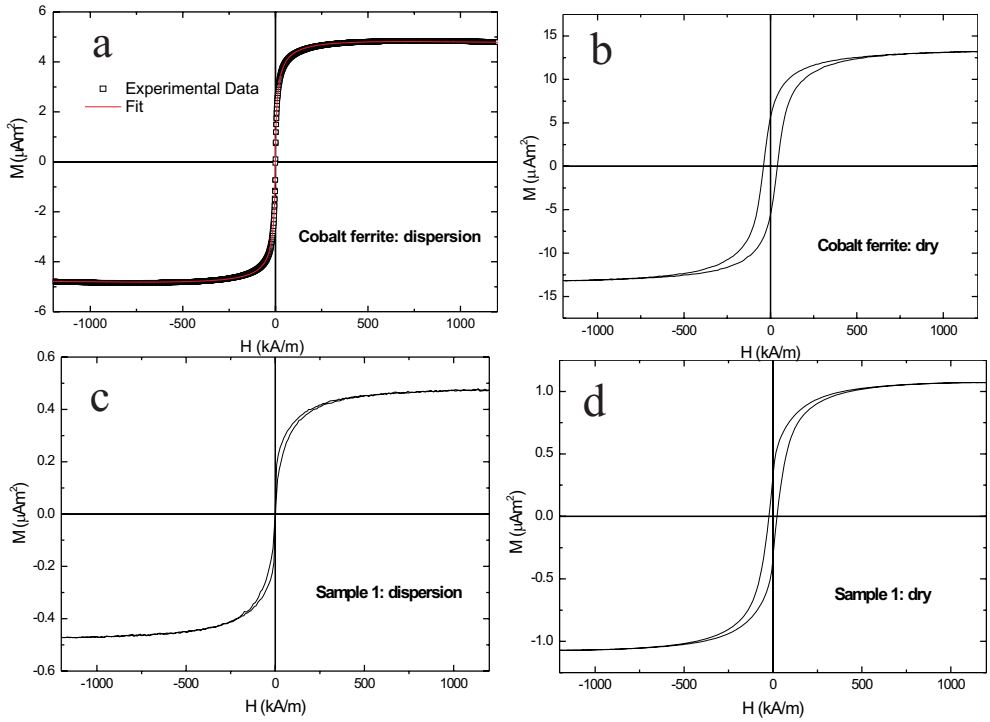

Figure 5.3. Magnetization curves of (a) cobalt ferrite nanoparticles in dispersion, (b) dry powder (0.27 mg) of cobalt ferrite particles, (c) silica-cobalt ferrite microspheres (Sample 1) in dispersion, and (d) dry powder (0.52 mg) of Sample 1.

cobalt ferrite particles in the dry state. However, from the saturation magnetization of dry microparticles ($2.06 \cdot 10^{-3}$ $\mathrm{Am^2g^{-1}}$, Figure 5.3 d), valuable information can still be obtained. The total amount of magnetic material can be calculated based on the weight of microparticles, which for Sample 1 (see Table 5.1) corresponds to 42.1 mg nanoparticles per gram microspheres.

Frequency-dependent complex magnetic susceptibility

In Figure 5.4, a magnetic susceptibility spectrum is shown of silica microparticles doped with maghemite. In that case, Brownian rotation of the microspheres does not determine the characteristic frequency, since the nanoparticle dipoles relax by the Néel mechanism with characteristic frequencies beyond the experimentally accessible range. Complex magnetic susceptibility spectra of cobalt ferrite doped silica microspheres in dispersion are shown in Figures 5.5 and 5.6. When the cobalt ferrite nanoparticles are embedded in silica microparticles, rotational diffusion of the microspheres determines the characteristic frequency, 3.323 Hz for the microspheres in Sample 1 and 0.416 Hz for the microspheres in Sample 2. The curves through the data points in Figures 5.5 and 5.6 are least-squares fits of the spectra based on (5.7), (5.10 -5.12) and a lognormal (5.1) distribution of the characteristic frequency ω_B [109] around a value of $< \omega_B >$ with variance σ^2. From the characteristic frequencies, the hydrodynamic radii the

microparticles in Sample 1 and Sample 2 are obtained (see Table 5.2). The low polydispersity of the hydrodynamic radii is in agreement with the observation of colloidal crystal formation in the particle sediments. The hydrodynamic radii from complex magnetic susceptibility measurements are comparable to the radius of single particles obtained from analysis of electron microscopy pictures (Figure 5.2). The hydrodynamic radius is expected to be larger than the TEM radius for several reasons. First, here a volume-averaged radius is measured instead of the number-averaged sphere radius from image analysis of TEM pictures. Second, the hydrodynamic radius is calculated from the rotational diffusion coefficient (5.9) which decreases as the particle volume fraction increases [110–112], which might lead to an overestimate of R_h as the sample is not infinitely diluted. Moreover, the irregular surface of the microspheres will contribute to a decrease in the rotational diffusion coefficient, resulting in a larger hydrodynamic radius. It should also be noted that the slightly porous silica microparticles tend to shrink under high vacuum in the electron microscope, which leads to an underestimate of the physical radius of the particles.

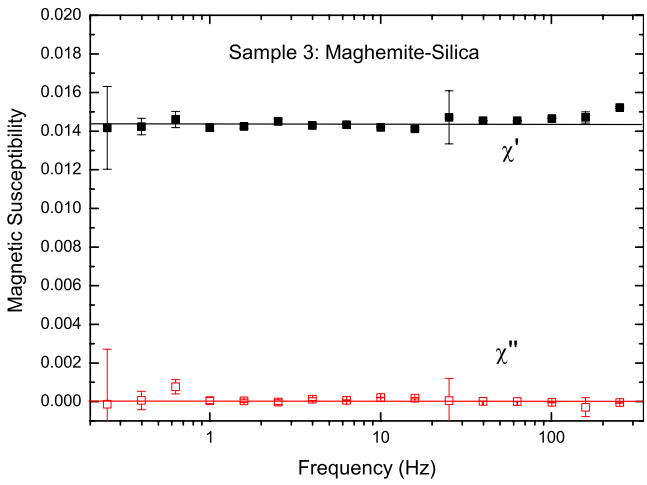

Figure 5.4. Low-field low-frequency complex magnetic susceptibility spectrum of a dispersion of maghemite-doped silica microparticles (Sample 3). The dipole moments inside the nanoparticles are not blocked, as would be the case for cobalt ferrite. Therefore the magnetic susceptibility is constant in the low-frequency range, and the Brownian rotation of such particles, expected around 5 Hz, cannot be detected in the spectrum.

The zero-field magnetic moment of the microparticles can be calculated from the low-frequency limit of the susceptibility spectrum using (5.8) and requires knowing the colloidal concentration N_{mp}/V. In Figures 5.5 and 5.6, the microparticle concentration is $3.53 \cdot 10^{17}$ m^{-3} and $1.32 \cdot 10^{17}$ m^{-3} respectively. This corresponds to permanent magnetic dipole moments $\mu_{\mathrm{mp}} = 3.03 \cdot 10^{-17}$ Am^2 for the particles in Sample 1 and $\mu_{\mathrm{mp}} = 4.19 \cdot 10^{-17}$ Am^2 for the particles in Sample 2. These values are higher than the magnetic moment of a single nanoparticle ($\mu_{\mathrm{np}} = 1.61 \cdot 10^{-19}$ Am^2) but lower than the

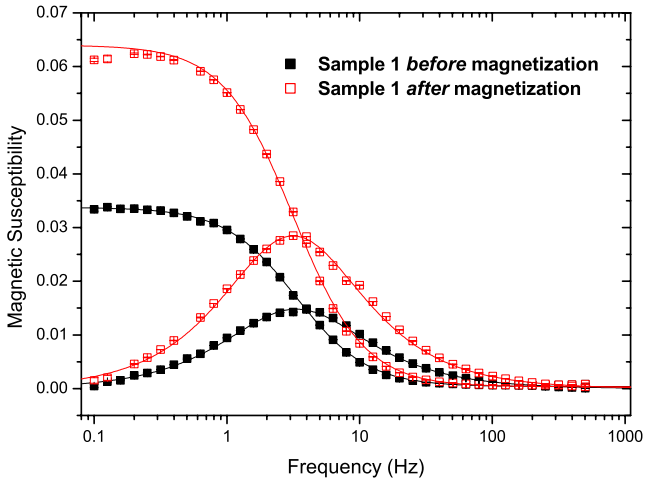

Figure 5.5. Complex magnetic susceptibility spectra of Sample 1 before and after magnetic treatment at 2 T. The value of χ_{LF} increases by a factor 1.9 after magnetic treatment, which corresponds to an increase of the permanent microsphere dipole moment by 38 % (Eqn. 5.8). The theoretical fits are shown as full lines.

magnetic moment of a microparticle in a saturating magnetic field as will be discussed in the previous section.

At 300 Hz, the susceptibility is nearly zero, in line with the fact that all cobalt ferrite nanoparticles are embedded in microspheres (any free nanoparticles were removed during purification steps involving centrifugation) and that the dipole moments of most of the nanoparticles are blocked. In Sample 1, at 1 Hz, Néel relaxation is responsible for only about 1.5 % of the observed signal.

After treatment of Sample 1 and Sample 2 in a magnetic field of 2 T, the magnetic silica particles have a larger magnetic dipole moment than prior to field exposure. This is revealed by the higher value of the low-frequency limit (Figures 5.5 and 5.6). During the particle preparation, care had been taken not to make use of any magnet, to be able to compare the microparticle dipole moment before and after magnetization. In terms of the average magnetic moment of the nanoparticles the magnetic moment of the Sample 1 particles increased from $188 \cdot \mu_{np}$ to $260 \cdot \mu_{np}$, an increase of 38 %. In Sample 2, the dipole moment increased from $355 \cdot \mu_{np}$ to $520 \cdot \mu_{np}$, an increase of 47 %.

Field-amplitude dependent complex magnetic susceptibility

The permanent magnetic moment of the silica particles was also determined from the field-amplitude dependence of the low-frequency magnetic susceptibility. This method does not require a value of the concentration of particles in the dispersion to determine the permanent magnetic moment of the microspheres as with for the frequency-dependent spectra. In that case, the number concentration might have been under- or overestimated due to an under- or overestimation of the density of the slightly porous

Table 5.2. Fit parameters and microsphere dipole moments obtained from the frequency spectra in Figures 5.5 and 5.6.

	Sample 1	Sample 2
	Before magnetization	
$< \omega_B > /2\pi$ (Hz)	3.323 ± 0.009	0.416 ± 0.005
σ	0.5400 ± 0.0003	0.12 ± 0.01
R_h [a] (nm)	244 ± 44	487 ± 20
$\chi_{LF} + \chi_{HF}$	0.03375 ± 0.00003	0.0453 ± 0.0004
χ_{HF}	0.0004 ± 0.0005	0.0012 ± 0.0005
μ_{mp} (Am^2) [b]	$3.03 \cdot 10^{-17}$	$5.71 \cdot 10^{-17}$
	After magnetization	
$< \omega_B > /2\pi$ (Hz)	3.16 ± 0.05	0.307 ± 0.002
σ	0.520 ± 0.001	0.333 ± 0.011
$\chi_{LF} + \chi_{HF}$	0.0640 ± 0.0004	0.096 ± 0.001
χ_{HF}	0.00033 ± 0.0001	0.00067 ± 0.00002
μ_{mp} (Am^2) [b]	$4.19 \cdot 10^{-17}$	$8.37 \cdot 10^{-17}$

[a] Obtained from (5.9) with $\eta = 1.074$ mPa s and $T = 295.5$ K.

[b] Obtained from (5.8) with the particle concentrations from Table 5.1. The relative error of the dipole moment is not known, due to an unknown error in N_{mp}/V. However, the values here agree within 2% with the values obtained from the field-amplitude dependent measurements whose interpretation is not depending on a value for N_{mp}/V.

silica particles. Measurements are presented in Figure 5.7. As expected from (5.15), the susceptibility decreases when the magnetic field amplitude increases, which further confirms that the microparticles have a permanent magnetic moment in contrast to microparticles that only have an induced magnetic moment, which increases with the magnetic field, leading to an increase of the initial magnetic susceptibility [113, 114]. The cobalt ferrite-doped magnetic silica particles can gain an induced magnetic moment as well, but to see the corresponding increase of the magnetic susceptibility, the magnetic field amplitude would have to be higher than here (more than 1 kA/m). The magnetic moment of Sample 1 before magnetic treatment determined from Figure 5.7 is $\mu_{\mathrm{mp}} = 3.08 \cdot 10^{-17}$ Am^2 ($\alpha/H = 0.095$ m/A). After magnetic treatment, the particles have gained a larger dipole moment as seen also in the frequency-dependent susceptibility spectra. At low fields (< 300 A/m), the measured susceptibility decreases faster with the applied field with $\alpha/H = 0.0131$ m/A, which corresponds to a dipole moment $\mu_{\mathrm{mp}} = 4.25 \cdot 10^{-17}$ Am^2. These values are in good agreement with the dipole moments obtained from the frequency-dependent spectra, which confirms that the number concentration in Table 5.1 had been determined accurately. Surprisingly, at higher fields

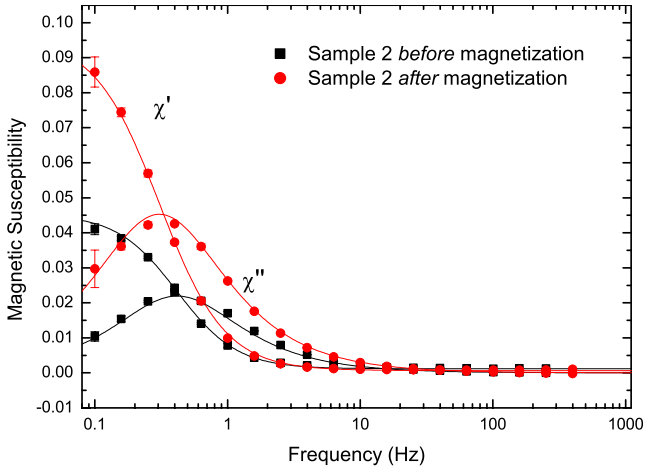

Figure 5.6. Complex magnetic susceptibility spectra of Sample 2 before and after magnetic treatment at 2 T. The value of χ_{LF} increases by a factor 2.16 after magnetic treatment, which corresponds to an increase of the permanent microsphere dipole moment by 47 %. The theoretical fits are shown as full lines.

($>$ 300 A/m), the amplitude dependence of the measured susceptibility for the magnetized sample is no longer described by (5.15). The only difference between the two measurements is the magnetic dipole moment of the particles; any chemical change of the sample on the timescale of the measurements is unlikely. Therefore, this effect at higher fields could be related to the appearence of dipolar structures that break up as the field amplitude is decreased. Another possibility is that the polydispersity of the microsphere dipole moment is larger after the magnetic treatment (the Langevin equation (5.3) assumes a monodisperse system).

The results in Figure 5.7 indicate that even when measuring at fields as low as 100 A/m, there is a measurable deviation from the low-field approximation. A comparison of two frequency-dependent susceptibility spectra of Sample 1, measured at $H = 57$ A/m and 731 A/m respectively, is presented in Figure 5.8. In the low-frequency limit, for instance at 0.1 Hz, the measured susceptibility decreases with the applied field amplitude as in Figure 5.7. However, the characteristic frequency shifts from $\sim$ 4 Hz at 57 A/m to $\sim$ 7 Hz at 731 A/m and above 10 Hz, the measurements at the two different amplitudes in Figure 5.8 overlap. It is interesting to compare these results to the observations made by Fannin *et al.* [114]. They observed an increase of the absorption peak frequency upon increasing the strength of a DC field superimposed on the AC-field. In that case, the field-amplitude dependence was ascribed to a gradual size-dependent immobilization of polydisperse nanoparticles, where the largest particles were slowed down first. In our case, the microspheres have a narrow size distribution, hence the same explanation cannot hold.

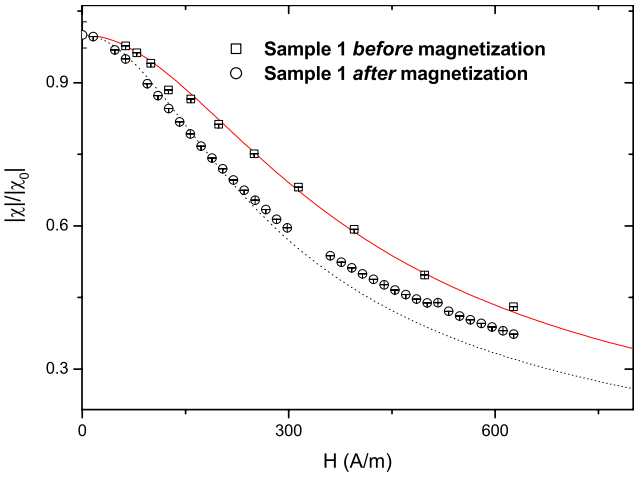

Figure 5.7. Measured susceptibility at 1 Hz of Sample 1 before and after magnetic treatment as a function of the amplitude of the applied magnetic field. The solid line through the data points is the expression in (5.15) with the fit parameter $\alpha/H = 0.095$ m/A, which corresponds to a microsphere dipole moment, $\mu_{\mathrm{mp}} = 3.08 \cdot 10^{-17}$ Am^2 and the dotted line is (5.15) with the fit parameter $\alpha/H = 0.0131$ m/A, which corresponds to a microsphere dipole moment $\mu_{\mathrm{mp}} = 4.25 \cdot 10^{-17}$ Am^2. The decrease in measured susceptibility as a function of field confirms of that the microspheres have a permanent dipole moment. For the particles with a larger dipole moment, at fields higher than 300 A/m the data can no longer be described by (5.15).

At low amplitude, the alternating field probes the rotational diffusion of the particles without having a major effect on the particle motion. However, at high amplitude, the magnetic torque on the particles is no longer negligible, but it speeds up their rotational motion, which leads to a shift of the absorption resonance to a higher frequency [115, 116]. Empirically, the amplitude dependence of the measured spectra can be fitted fairly well based on the following formulas:

$$\chi' = \chi_0' F\left[H_1 \frac{\omega_0^2}{\omega_0^2 + \omega^2}\right] \tag{5.18}$$

$$\chi'' = \chi_0'' F\left[H_2 \frac{\omega_0^2}{\omega_0^2 + \omega^2}\right] \tag{5.19}$$

where $F(x) = L(x)/(x/3)$ and χ_0', χ_0'' and ω_0 are the low-amplitude values of χ', χ'' and ω_B. However, a good fit requires using field amplitudes H_1 and H_2 that differ from the experimental values ($H_1 = 550$ A/m and $H_2 = 1200$ A/m whereas $H_{exp} = 731$ A/m). Moreover, at amplitudes above the weak-field limit, a full analysis should also include higher-order harmonic terms [115].

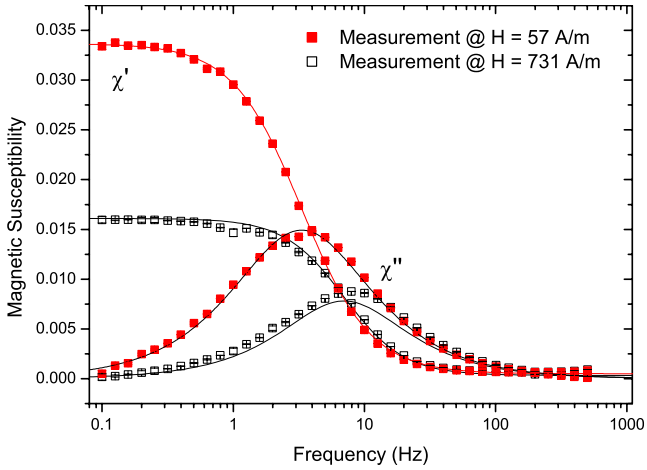

Figure 5.8. Susceptibility spectra of Sample 1 measured at $H = 57$ A/m and 731 A/m, respectively. In the latter case, the spectra are no longer measured in the low-field limit and the measured susceptibility is therefore lower than at 57 A/m in agreement with Figure 5.7 at low frequencies. At higher frequencies, the measured susceptibility is the same for both field amplitudes.

5.5. Discussion

The measurements clearly show that silica microparticles with embedded cobalt ferrite nanoparticles have a permanent magnetic dipole moment. The magnetic moment depends on the magnetic field-treatment history of the sample, which affects the orientation of the blocked nanoparticle dipoles. Before discussing the effect of magnetic treatment, we examine the theoretical case of randomly oriented dipoles. Finally, the interactions between the microspheres are discussed.

Randomly oriented nanoparticle dipoles

In zero field, the magnetization of a dispersion of particles with a permanent magnetic dipole moment is zero. For every dipole oriented one way, another dipole is present that is oriented in the opposite direction, so that oppositely oriented dipoles cancel each other's contributions to the total magnetic moment. However, when magnetic nanoparticles are embedded in a single microsphere, the number of embedded nanoparticle dipoles is limited and they do not cancel statistically.

To calculate the magnetic moment of a microparticle, the magnitude of the vector sum of the individual dipoles must be determined. The vector sum of N randomly oriented unit vectors is on average equal to $\sqrt{N}$. Therefore, if all the nanodipoles inside the microparticles were randomly oriented, the average dipole moment of one microparticle would be $\sqrt{N}\mu_1$, where μ_1 is the magnetic dipole moment of a nanoparticle. Random orientation of the nanodipoles inside a microparticle means that all orientations are equally probable, but it does not mean that exactly the same number of dipoles is oriented in opposite directions. A direct analog is the effect of a random

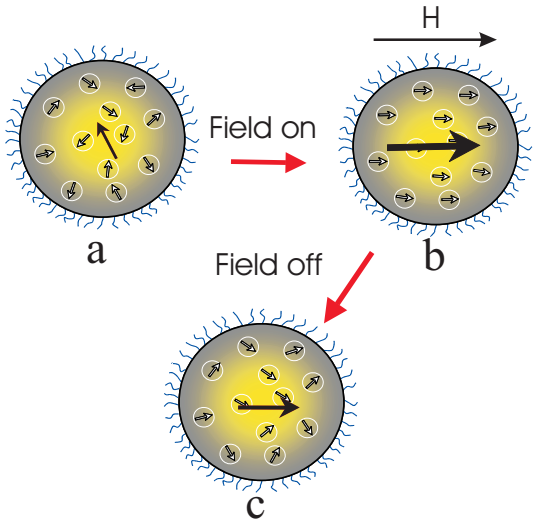

Figure 5.9. Schematic illustration showing silica microspheres with embedded cobalt ferrite nanoparticles: (a) as synthesized, exposed only to the earth magnetic field, (b) while exposed to a strong external magnetic field, causing all individual dipole moments of the nanoparticles to align in the field direction, resulting in a large induced microsphere dipole moment and (c) after removing the external magnetic field, upon which the nanoparticle dipole moments relax back to the easy axis closest to the direction of the applied magnetic field, resulting in a microsphere dipole moment which is smaller than in (b) but larger than in (a).

walk: displacement is equally probable in all directions, but nevertheless the average displacement from the starting point is not zero but scales with the square root of the number of steps.

The results from our measurements on Sample 1 show that the average number of nanoparticles per microparticle is approximately N=900. The corresponding microsphere dipole moment in zero field is expected to be on the order of $\sqrt{900} \cdot \mu_1 = 30 \cdot \mu_1$ if all the nanoparticle dipoles are randomly oriented, assuming that all the nanoparticles have blocked dipole moments. The actual magnetic moment of the as-synthesized microspheres was found to be about $190 \cdot \mu_1$, more than six times the random-orientation value. During the synthesis, care was taken not to expose the particles to an external magnetic field other than the earth magnetic field, which is approximately 40 A/m and has a negligible interaction $\mu_0 \mu H$ of about $2 \cdot 10^{-3}$ $k_B T$ with the nanoparticles. One possible explanation for the magnetic moment of the microparticles being larger than the random-orientation value is interaction between the nanoparticle dipole moments. The dipole-dipole interaction between two d =10 nm cobalt ferrite particles in head-to-tail configuration at contact is about 1.3 $k_B T$, calculated using

$$V = -\frac{\mu_0 \mu_1^2}{2\pi d^3} \tag{5.20}$$

where d is the diameter of the core of a nanoparticle. This interaction is sufficiently strong to block the dipole orientations if each nanoparticle interacts with more than one neighbour. Moreover, larger particles in the size distribution will experience much stronger dipole-dipole interactions than the average value of 1.3 k_BT. Strong dipolar interactions between the larger nanoparticles can be present already during the synthesis of the microspheres, which might lead to nanoparticles forming aggregates before they attach to the silica surface. Consequently, within these aggregates, the nanoparticle dipole moments will not have a random orientation. It can be concluded that significant dipolar coupling occurs between the nanoparticles inside the microspheres.

Effect of magnetic field treatment

When a magnetic field is applied, the microparticles gain an induced magnetic dipole moment and when the magnetic field is sufficiently strong, the zero-field magnetic dipole moment is changed as illustrated in Figure 5.9. Before magnetic treatment, the as-synthesized particles have a permanent magnetic moment as discussed in section 5.5. During treatment in a strong magnetic field, for instance at 2 T, all the nanoparticle dipoles are aligned. Once the field is removed, the dipoles which are thermally blocked in zero field relax to an easy axis of magnetization. Before such magnetic treatment, the vector components of the dipoles along the field direction can have random signs, but after magnetic treatment, that vector component is in the direction of the field instead of the opposite direction, at least in the limit case. This is because when the strong magnetic field is removed, the dipoles are expected to relax to the easy-axis direction that is closest to the field direction. The expected dipole moment would now be approximately $2N\mu_1/3$ as found from numerical calculations of the average sum of N vectors whose orientation is random except for all the x-components being given equal signs.

From the low-field limit of the complex magnetic susceptibility spectrum of Sample 1, the calculated dipole moment of the magnetically treated particles is $260 \cdot \mu_1$ instead of the expected value of $2 \cdot 900 \cdot \mu_1/3$=600 $\cdot\mu_1$. Even though the magnetic moment of the microparticles has increased, the limiting case is not reached. Moreover, in the magnetization curves of dry Sample 1 (Figure 5.3) the remanence (M_r/M_s) is not $2/3 = 0.667$ but 0.305 for the Sample 1 particles. This is lower than 0.425 for the dry nanoparticles that are not embedded in microparticles. The remanence is higher for the nanoparticles than for the microparticles, probably due to dipole-dipole interactions. The dry nanoparticles are present in a compact 3D network, while on the silica particles, the cobalt ferrite particles are spread over a (2D) surface as observed with electron microscopy.

Dipolar and hydrodynamic interactions

From the permanent dipole moments of the magnetic silica particles, the dipole-dipole interactions between the particles can be estimated. The maximum magnetic interaction between two composite particles using (5.20) with $d = 2R_h = 468$ nm is about 0.4 k_BT for the microparticles in Sample 1 and 0.8 k_BT for magnetically treated Sample 1. For doublets or larger dipolar structures in zero field, the head-to-tail dipolar pair interaction energy should exceed 2 k_BT [8,9,27]. Clearly, no dipolar structures are expected in the magnetic silica dispersions. Their absence is confirmed by the complex susceptibility spectra, in which dipolar structures would not just show the Brownian rotation of single microparticles but also that of dipolar structures, with several times lower characteristic frequencies for Brownian rotation than for single microspheres [106]. Moreover, the susceptibility would not become constant just below the characteristic frequency for single microparticle rotation. It is noted that equation 5.20 is not strictly applicable to the microparticles because they are not point dipoles. It only gives an estimate of the interaction between composite microparticles. The magnetic material is in a shell near the surface of the spheres. The dipolar interaction between two magnetic microparticles in this case might therefore be stronger than it would have been if all the nanoparticles were embedded at the center of the microparticles. This point will be discussed in Chapter 6.

Although insufficient for aggregation, interactions of 1 k_BT or less between microparticles can still affect the Brownian rotation in a detectable way. In the complex magnetic susceptibility spectra of Samples 1 and 2 (see Figures 5.5 and 5.6), the characteristic frequencies are slightly shifted to lower frequencies after increasing the dipole moment by treatment in a strong magnetic field. Since the concentration of particles was constant, this indicates a decreasing rotation rate due to dipolar interactions. In other experiments, the same decrease in the rotation rate could be due to adsorption of molecules at the surface of the microparticles, which increases the hydrodynamic radius of the particles. The latter effect can be used to develop highly sensitive biomolecular sensing procedures, as was demonstrated by Astalan *et al.*. [117]. The interaction of the microspheres with even larger objects could drastically slow down the motion of the microspheres. The rotational dynamics of microspheres with a permanent magnetic moment are examined as a function of particle concentration in Chapter 6.

5.6. Conclusions

Magnetic silica microparticles with embedded cobalt ferrite nanoparticle have a permanent magnetic dipole moment. This is revealed by a relaxation in the complex magnetic susceptibility spectrum at the frequency corresponding to Brownian rotation of the microparticles. The magnetic moment of the magnetic composite particles can

be calculated from the initial magnetic susceptibility, if the concentration of the dispersion is known. Alternatively, the initial susceptibility can be measured as a function of the magnetic field amplitude. The susceptibility decreases with increasing magnetic field amplitude, due to the non-linearity of the Langevin equation, and from that the microparticle dipole moment can be calculated without knowing the particle concentration. The magnetic moment of the microparticles before and after magnetization in a strong magnetic field can be understood in terms of the orientations of the embedded nanoparticle dipoles, along an easy axis of magnetization in the absence of an external field. Even if the dipoles had random orientations, the vector sum of the nanoparticle dipoles of each microparticle would be non-zero and, in our case, dipolar coupling between the nanoparticles also affects the orientation of the as-synthesized particles before exposure to a strong magnetic field. The permanent magnetic moment of the microparticles increases further after exposure to a strong magnetic field, since the dipole orientations do not relax to a random distribution when the field is removed.

Acknowledgements

This work was performed together with Emile Bakelaar and Bonny Kuipers, who provided intensive technical support and many helpful discussions. The SEM pictures were made by Stefano Sacanna.

6

Rotational Dynamics of Magnetic Silica Spheres Studied with Complex Magnetic Susceptibility Measurements

Abstract

The weak permanent magnetic dipole moment of cobalt ferrite-doped colloidal silica spheres was increased by exposure to a saturating magnetic field. The resulting change of the rotational dynamics of the magnetic microspheres in a weak alternating field was measured from low to high volume fraction in ethanol, using a frequency-dependent complex magnetic susceptibility setup. At low volume fractions, the increased dipolar attraction slows down Brownian rotation. At higher volume fractions, however, rotation is no longer slowed down as rapidly with increasing concentration, likely due to dipolar coupling between the particles which accelerates their partial alignment with the alternating field. This explanation is supported by the unexpected finding that salt addition accelerates particle rotation rather than slowing it down. At the highest volume fraction, colloidal crystals and glasses were formed in which only a small fraction of the spheres exhibit rotational mobility.

6.1. Introduction

A widely applied experimental approach to determine the particle size *in situ* in colloidal dispersions is to measure the characteristic time or frequency of translational or rotational diffusion of the particles. This is usually done with optical techniques such as dynamic light scattering (DLS) [118], depolarised dynamic light scattering (DDLS) [101,110,119], time-resolved phosphorescence anisotropy (TPA) [102,120,121], and polarized fluorescence recovery after photo-bleaching (pFRAP) [103]. These techniques usually require particles which are nearly refractive index matched with their dispersion medium. Particles with a permanent electric [122] or magnetic dipole moment are usually highly light absorbing and cannot be optically matched in common solvents. With techniques like TPA and pFRAP, optical problems in more concentrated systems are avoided with so-called tracer particles, *i.e.*, particles that are labelled with dye and which are dispersed in a more concentrated dispersion of non-labelled particles (hosts). In practice, synthesizing two different batches of particles that are chemically and physically identical, except for the dye, is difficult and for the interpretation, a difference in size between tracer and host particles must be taken into consideration [123]. Here, we make use of a magnetic technique to study the concentration dependence of the rotational diffusion of interacting dipolar colloidal spheres dispersed in a liquid.

The expected trends for the qualitative effects of hydrodynamic and electrostatic interactions on the rotational diffusion of spheres have been well established in other publications [110–112,119]. In very dilute dispersions, the spheres do not influence each other, but when the concentration is increased, rotational diffusion is slowed down by hydrodynamic interaction: the rotation of one particle locally causes flow of the solvent around it, and this flow hinders the free rotation of neighbouring colloidal particles. The extent to which hydrodynamic interaction affects rotation depends on the total pair interaction potential of the spheres. Attraction locally causes spheres to approach each other, hence hydrodynamic interaction is increased and rotation slows down, whereas repulsion keeps the spheres apart and hydrodynamic interaction is counteracted. The quantitative relationship between pair potential and rotational diffusion coefficient is not straightforward. Our aim is to gain new insight into that relationship by experimentally studying the effect of increasing attraction between dispersed colloidal spheres in an original and highly selective way.

Previously, systematic studies of the experimental factors affecting rotational diffusion always involved changes in the chemical composition of the colloidal dispersion. For example, the salt concentration was varied to affect the electrostatic repulsion [102]. In the present work, we study the rotational diffusion of recently developed colloidal silica spheres with embedded cobalt ferrite nanoparticles [46]. The spheres have a magnetic dipole moment in zero magnetic field and it can be permanently increased by

exposure to a saturating magnetic field [124]. In this way, the attractive component of the total interaction potential is changed selectively, without any other change in the chemistry or physics of the system. This makes it possible to ascribe any resulting change in the rotation rate unambiguously to enhanced dipolar attraction. We present an experimental investigation of particle rotation in a colloidal system with repulsive as well as attractive interactions and qualitatively discuss the observed trends.

In Section 6.2, a theoretical background is given to the rotational diffusion of spheres, interaction potentials and the complex magnetic susceptibility technique. After a description of experimental methods in Section 6.3, a study of rotational dynamics is presented in Section 6.4, based on complex magnetic susceptibility spectra. A general discussion of the results follows in Section 6.5, leading to final conclusions in Section 6.6.

6.2. Theory

Rotational diffusion and interaction potentials

For a free single spherical particle in a solvent with viscosity η_0, the rotational diffusion coefficient D^r is given by the Stokes-Einstein-Debye relation (SED) :

$$D_0^r = \frac{k_B T}{8\pi\eta_0 R_h^3}, \tag{6.1}$$

where $k_B T$ is the thermal energy and R_h the hydrodynamic radius of the particle. At infinite dilution, the rotating colloids only experience the viscous drag by the solvent as quantified by (6.1). As the concentration of particles is increased, interactions with neighbouring particles come into play and the rotational diffusion coefficient is no longer described by the SED-relation (6.1). For hard spheres, several theoretical studies of the concentration dependence of the rotational diffusion coefficient have been presented [110, 112, 125]. Cichocki *et al.* [125] proposed an expression for the decrease of the rotational diffusion coefficient with increasing volume fraction ϕ:

$$D^r(\phi)/D_0^r = 1 - 0.631\phi - 0.726\phi^2. \tag{6.2}$$

For highly charged spheres, in deionized suspensions, Watzlawek and Nägele [111] proposed the following:

$$D^r(\phi)/D_0^r = 1 - 1.28\phi^{1.99}. \tag{6.3}$$

These expressions manifest that Brownian rotation slows down as the concentration of particles increases and that this decay is slower for repulsive particles. The colloidal systems studied in this work consist of charged silica particles with weak magnetic dipolar interactions. In contrast to experiments with optical measuring techniques, the silica particles are dispersed in a non-matching solvent and van der Waals interactions

should therefore be taken into account. The overall interaction potential for the particles used in our study may be represented as:

$$U(r) = U_{HS}(r) + U_{vdW}(r) + U_{dip}(r) + U_{el}(r). \tag{6.4}$$

The first term is the hard-sphere potential, which prevents particle overlap:

$$U_{HS}(r) = \begin{cases} \infty & ; r < 2R \\ 0 & ; r > 2R \end{cases}, \tag{6.5}$$

$U_{vdW}(r)$ is the attractive van der Waals interaction:

$$U_{vdW}(r) = -\frac{H}{12}\left[\frac{1}{(r/2R)^2-1} + \frac{1}{(r/2R)^2} + 2ln\left(\frac{(r/2R)^2-1}{(r/2R)^2}\right)\right], \tag{6.6}$$

where H is the Hamaker constant, R the particle radius and r the centre-to-centre distance between two spheres.

The interaction between two permanent magnetic point dipoles in arbitrary orientations is given by:

$$U_{dip}(r) = \frac{\mu_0\mu_1\mu_2}{4\pi r^3}\left[\hat{\mu}_1 \cdot \hat{\mu}_2 - 3(\hat{\mu}_1 \cdot \hat{r})(\hat{\mu}_2 \cdot \hat{r})\right], \tag{6.7}$$

where $\mu_0 = 4\pi \cdot 10^{-7}$ JA^{-2}m^{-1}, μ_1 and μ_2 are the magnetic dipole moments of spheres 1 and 2, $\hat{\mu}_1$ and $\hat{\mu}_2$ are unit vectors pointing along the directions of the dipoles of particles 1 and 2 and $\hat{r}$ is a unit vector that points in the direction from the centre of particle 1 to that of particle 2. When the prefactor $\mu_0\mu_1\mu_2/4\pi r^3$ is small compared to k_BT and $\mu_1 = \mu_2 = \mu$, the Boltzmann-weighted average of U_{dip} is given by:

$$< U_{dip}(r) >= -\frac{2(\mu_0\mu^2)^2}{3k_BT(4\pi)^2r^6} \tag{6.8}$$

The Boltzmann weights $exp[-U_{dip}/(k_BT)]$ depend on the orientation according to (6.7), which is the classic formula for the pair potential of permanent dipoles [126]. In (6.8) it is assumed that only a weak statistical preference exists for the head-to-tail dipole-dipole configuration and that the interaction can be treated as an isotropic attraction.

The electrostatic term for the interaction between colloidal spheres with a constant surface charge Ze is:

$$U_{el}(r) = \frac{(Ze)^2}{\epsilon_0\epsilon_r}\left[\frac{exp(\kappa R)}{1+\kappa R}\right]^2 \frac{exp(-\kappa R)}{r} \tag{6.9}$$

in which the inverse Debye screening length κ for a monovalent salt is given by:

$$\kappa = \sqrt{\frac{2e^2c_s}{\epsilon_0\epsilon_r k_BT}}, \tag{6.10}$$

where e is the elementary charge, ϵ_0 the vacuum permittivity, ϵ_r the dielectric constant of the solvent (for ethanol, $\epsilon_r = 25.3$ [105]) and c_s is the salt concentration given in number of cations or anions per volume.

Complex magnetic susceptibility

To monitor the rotational diffusion in a colloidal system of isotropic particles, these must be anisotropically labelled. For DDLS, the particles should have an optically anisotropic crystalline core and the relaxation of the labels is measured by monitoring the evolution of the depolarised component of the scattered intensity [119]. With techniques such as TPA or pFRAP, an anisotropic label is created by illuminating fluorescent particles with a polarized light beam. The decay of the polarized phosphorescence or the fluorescence emission is ascribed to orientational relaxation of the particles and is measured in time [103, 120].

For complex magnetic susceptibility spectroscopy, an anisotropic probe is present in the form of a permanent magnetic dipole moment inside the colloids. With the highly sensitive setup used here, particles with a low magnetic content can be studied at low concentrations. The magnetic nanoparticles embedded inside the microparticles act as a probe to measure the diffusive reorientation.

The complex magnetic susceptibility as a function of the radial frequency, ω, is defined as:

$$\chi(\omega) = \frac{M(\omega)}{H(\omega)}, \tag{6.11}$$

where $H(\omega)$ is the applied alternating magnetic field and $M(\omega)$ is the resulting harmonic magnetization. For colloidal particles with a permanent magnetic dipole moment, frequency-dependent measurements of χ at low $H(\omega)$ field amplitude yield the rotational diffusion rate of the particles [124]. The characteristic frequency ω_B is obtained from spectra of the real and imaginary components of the complex susceptibility:

$$\chi'(\omega) = \chi_{HF} + \chi_{LF}\frac{\omega_B^2}{\omega_B^2 + \omega^2} \tag{6.12}$$

$$\chi''(\omega) = \chi_{LF}\frac{\omega_B\omega}{\omega_B^2 + \omega^2} \tag{6.13}$$

Here, χ_{HF} is the high-frequency limit and χ_{LF}+χ_{HF} is the low-frequency limit of the susceptibility. Whereas χ_{HF} is due to nanoparticles whose magnetic moment is not blocked inside the nanocrystals, χ_{LF} scales with the volume fraction, ϕ of magnetic silica particles and the square of their dipole moment μ_{mp}:

$$\chi_{LF} = \frac{N_{mp}}{V}\frac{\mu_0(\mu_{mp})^2}{3k_BT} = \frac{\phi}{V_pV}\frac{\mu_0(\mu_{mp})^2}{3k_BT}, \tag{6.14}$$

where $\omega = 2\pi f$ is the angular frequency in s^{-1}, f is the cycle frequency in Hz, N_{mp} is the number of microparticles per sample volume, V is the volume of the entire sample and V_p is the volume of a single microparticle. With this technique, the magnetic contribution of the microparticles, χ_{HF}, is separated from other contributions to the susceptibility such as the field-induced alignment of nanoparticle dipoles that are not blocked or of free nanoparticles, which are not embedded in microparticles. Néel as well

as Brownian relaxation of single nanoparticles occur at much higher frequencies than the frequency of Brownian rotation of the microspheres [124].

The characteristic frequency, ω_B, is directly related to the rotational diffusion coefficient of the particles [107]:

$$\omega_B = 2D^r \tag{6.15}$$

Polydispersity is taken into account by fitting the results to a lognormal distribution of the characteristic frequency:

$$P(\omega_B) = \frac{1}{\sigma\omega_B\sqrt{2\pi}} exp[\frac{-ln^2(\omega_B/\omega_0)}{2\sigma^2}] \tag{6.16}$$

Here, σ^2 is the variance and ω_0 is the value of ω_B at the maximum of the distribution. Measurement of the susceptibility in the low-frequency limit on a sample with a known concentration N_{mp}/V allows calculation of μ_{mp}, which means that the average dipole-dipole interaction potential in the system can be estimated, based on the obtained value of μ_{mp} in (6.14) [124].

6.3. Experimental

Two samples of silica colloids were studied, both with embedded cobalt ferrite magnetic nanoparticles: in one sample the particles have a thin $\sim$ 10 nm silica layer around the magnetic particles and in the other this layer is $\sim$ 30 nm. It is expected that a thicker silica layer will reduce the magnetic interaction between spheres at particle contact. In the limiting case that the magnetic contact attraction is much weaker than k_BT, the magnetic core will only serve as a probe for measuring the Brownian rotation of the microparticles, whereas for particles with a thin layer of silica, the dipole-dipole interactions can still influence the rotational diffusion of the particles.

Sample preparation

The chemical synthesis of silica colloids with embedded magnetic nanoparticles has been described in detail in Chapter 2. In brief, cobalt ferrite nanoparticles were prepared in a coprecipitation step [45] and attached to Stöber silica particles [50] provided with thiol surface groups. The resulting silica-ferrite composites were coated with an outer silica shell, and the particle surface was grafted covalently with 3-(trimethoxysilyl)propyl methacrylate (TPM). The particle dispersions were purified by repeated sedimentation under gravity and redispersion in ethanol. The particle radius, R_{TEM} and the silica shell thickness, ΔR_{Si}, were obtained from image analysis of electron microscopy pictures (see Figure 6.1). The magnetic dipole moment of the silica-cobalt ferrite particles can be increased permanently by magnetic treatment (see Table 6.2) in a strong magnetic field (see Chapter 5). After susceptibility measurements on the as-synthesized magnetic silica particles, they were magnetized in a homogeneous field of

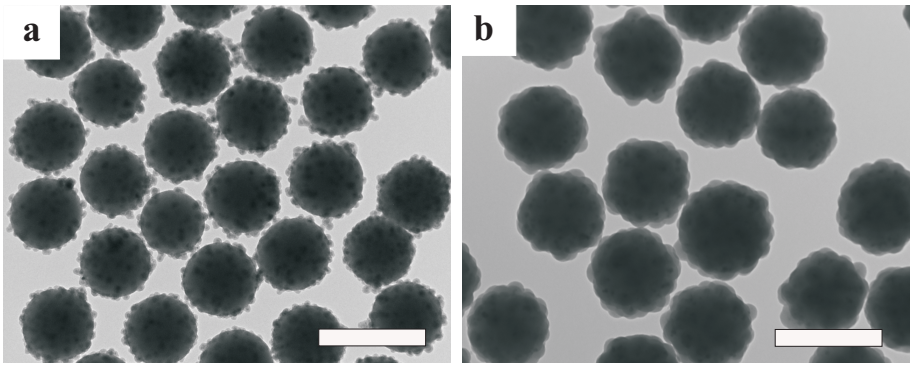

Figure 6.1. Transmission electron microscopy pictures of the studied particles: (a) silica-cobalt ferrite microspheres (Sample A) with a silica shell thickness of $\sim$ 10 nm and (b) silica-cobalt ferrite microspheres (Sample B) with a silica shell thickness of $\sim$ 30 nm. The scale bars correspond to 500 nm.

2 T using a Bruker BE 25v electromagnet, after which the susceptibility measurements were repeated. The magnetized sample was also measured after redispersion in ethanol with 10 mM $LiNO_3$.

A small amount of each dispersion with known weight m_{disp} and volume V_{disp} was dried to obtain the weight of dry particles, m_p. V_{disp} was obtained by measuring the height of the dispersion with a cathetometer inside a calibrated tube with a known volume-height relation. Together with the solvent density, $\rho_s = 0.789$ g/mL [105], the mass density, of the particles, ρ_p was calculated from:

$$\rho_p = \frac{m_p}{V_{disp} - \left(\frac{m_{disp} - m_p}{\rho_s}\right)} \tag{6.17}$$

The sample volume, V, was obtained in the same way as described above and the volume fraction, ϕ, of particles in stock dispersions of all samples was calculated:

$$\phi = \frac{\phi_m m_{disp}}{V \cdot \rho_p}, \tag{6.18}$$

where ϕ_m is the mass fraction of a stock dispersion. The measured value of χ_{HF} is directly proportional the number of Neél-relaxing particles in the sample. Since the ratio between the number of microparticles and the number of Neél-particles is constant for particles from the same synthesis batch, χ_{HF} can be used as an *in situ* measure for the volume fraction (see Section 6.4, Figure 6.6). The samples were diluted by stepwise addition of small aliquots of ethanol, followed by thorough homogenisation. Conductivity measurements in the supernatant after sedimentation as well as in a semi-dilute dispersion of both samples A and B showed a salt concentration of approximately 0.2 mM, which corresponds to a Debye length $\kappa^{-1} \approx 12$ nm (6.10). Salt was added to the magnetized sample A by repeated centrifugation of the particles and redispersion

in ethanol with 10 mM $LiNO_3$. This salt concentration decreases the Debye length to 1.7 nm.

Table 6.1. Characteristics of the magnetic silica dispersions

Sample Code	Sample A	Sample B
Physical radius, R_{TEM} (nm)	187 ± 34	207 ± 12
Hydrodynamic radius, R_h (nm) [a]	230 ± 30	286 ± 47
Silica shell thickness, ΔR_{Si} (nm)	~ 10	~ 30
Particle mass density, ρ_p (g/mL)	2.5	1.8

[a] calculated from (6.15) and (6.1) at the lowest measured concentration.

Complex magnetic susceptibility measurements

At each concentration, a frequency-dependent complex magnetic susceptibility spectrum was measured. For the fully sedimented samples, the spectra were measured starting from 500 Hz down to 0.1 Hz. However, for the diluted samples, for which the characteristic frequency is found at higher frequencies, the spectra were measured from 500 Hz down to 1 Hz. This was done to shorten the measurement time, thereby limiting the effect of sedimentation on the spectrum. Control spectra were also measured the other way around, from 1 to 500 Hz, to verify that the characteristic frequency remained the same, which was the case.

Complex magnetic susceptibility measurements were performed using a setup consisting of a differential transformer with two concentric multilayered cylindrical copper coils, with primary layers through which an applied alternating current flows and secondary layers in which an alternating voltage is induced. Secondary coils were used with a maximized number of layers beyond which the signal would no longer increase but decrease due to capacitance and absorption effects. An AC current is applied to the primary coils using a Yokogawa FG120 function generator, and the voltage induced in the secondary coils is measured using a 7265 Perkin-Elmer differential lock-in amplifier in the 0.1 Hz to 1 kHz range. When a sample is introduced into the coils, the change in the measured alternating voltage is proportional to the complex susceptibility of the sample. The amplitude of the alternating magnetic field is very low. The measurements here were performed at 57 A/m if not specified otherwise. A more detailed description of the setup will be presented elsewhere [108]. The coils with the sample were kept inside an isolated box with a constant temperature, T = 295.5 K.

For the highest volume fractions, the aspect ratio of the sample in the tube was of order 1, resulting in a demagnetisation of $\sim 10\%$. The measured absolute values of χ were corrected for demagnetisation effects using [127]:

$$\chi_{real} = \frac{\chi_{meas}}{1 - N_f \chi_{meas}} \tag{6.19}$$

N_f is a correction factor obtained from [127] which depends on the aspect ratio of the cylindrical sample. This correction is only approximate, since the cylindrical sample tube had a rounded bottom. The measured value of the characteristic frequency is not influenced by demagnetisation effects.

6.4. Results

A selection of the complex magnetic susceptibility spectra measured on dispersions of magnetic silica particles is shown in Figures 6.2 and 6.3. The solid lines in these figures are least-squares fits of the spectra based on Eqs. (6.12), (6.13) and a lognormal distribution of the characteristic frequency ω_B around a value of ω_0 with a variance σ^2 (6.16) [109].

Table 6.2. Properties of the magnetic silica dispersions before and after magnetization at 2 T.

	Sample A		Sample B	
	Before mag.	*After* mag.	*Before* mag.	*After* mag.
Dipole moment, μ (Am^2)	$2.5 \cdot 10^{-17}$	$3.6 \cdot 10^{-17}$	$2.7 \cdot 10^{-17}$	$3.1 \cdot 10^{-17}$
Max. dipole-dipole int.(6.7), U_{max} (k_BT)	0.59	1.2	0.49	0.65
Interaction with 57 A/m AC-field, $\mu_0\mu H$ (k_BT)	0.44	0.63	0.47	0.54

In Figure 6.2, susceptibility spectra are shown for samples A and B at the same concentration before and after magnetization of the sample. For the particles with a thin silica shell (A), the increase of dipole moment results in a slight shift of the characteristic frequency to lower frequencies, ω_0, and hence to a lower rotational diffusion coefficient D_r. For the particles with a thicker silica shell (B), this effect is not observed, as a consequence of the thicker silica shell in combination with a smaller increase in dipole moment.

In Figure 6.3 an example is shown of how the susceptibility spectrum changes upon dilution of a sample. At low concentrations, the spectra show a narrow distribution of ω_B and thus a narrow distribution of D_r (see Eqn 6.15). For the fully sedimented and partially crystalline samples, this distribution is broadened and the mean characteristic frequency and rotational diffusion coefficient are significantly lower. The broadening of the spectra at higher volume fractions is probably due to a polydispersity effect that becomes more important as the particles come closer together. In an ordered structure of particles, a small particle will be more free to rotate than its larger neighbours. This gives, averaged over a whole sample volume, a larger distribution of ω_0.

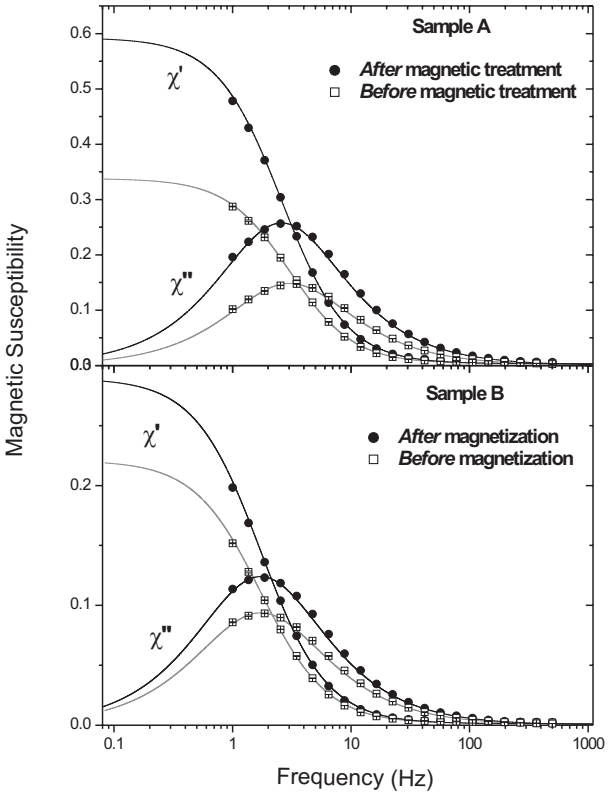

FIGURE 6.2. Frequency-dependent complex magnetic susceptibility spectra at moderate concentrations for samples A ($\phi = 0.12$) and B ($\phi = 0.13$) before and after magnetization of the sample at 2 T. The solid lines are least-squares fits of the spectra. The increase of χ_{LF} shows that the permanent dipole moment of the microparticles has been increased.

The rotational diffusion coefficients obtained from the susceptibility spectra are displayed in Figure 6.4 as a function of the volume fraction. The corresponding widths of the distributions of the characteristic frequency can be found in Figure 6.5. In the most dilute regime of sample A, the characteristic frequency is $\omega_0/(2\pi) \approx 3.7$ Hz before and after magnetization. This value decreases rapidly up to $\phi \sim 0.01$ for the magnetized sample.

At concentrations $\phi > 0.01$, the decrease in ω_0 as a function of ϕ is slower and parallel for sample A before and after magnetization. Finally, at the highest concentrations, where the particles are fully sedimented and form partially a colloidal crystal and partially a colloidal glass, there is again a drop in $\omega_0(\phi)$, accompanied by a steep increase of the distribution width of ω_B as the particles become restricted in their motion. A similar result is obtained when a colloidal glass phase is created by centrifugation of a dispersion at 20 g. Since the only difference between these two measurement series is the increase of the microparticle dipole moment, obtained by treatment in an external magnetic field, the difference in the two $\omega_0(\phi)$-profiles must be explained in terms of

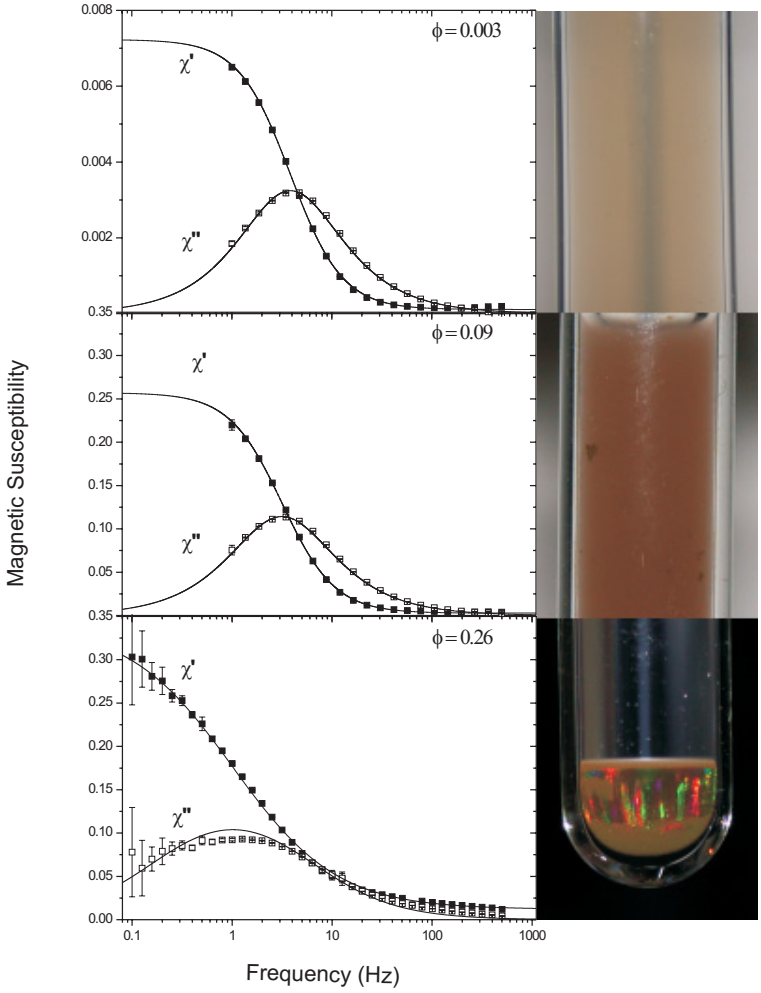

Figure 6.3. Frequency-dependent complex magnetic susceptibility spectra and photographs of the dispersion of sample A from high dilution ($\phi = 0.003$) to partially crystalline sediment ($\phi = 0.26$). For the sediment, the characteristic frequency is shifted to a lower value and the distribution of ω_B is broadened compared to the diluted samples.

increasing dipolar attractions as will be discussed in Section 6.5. Figure 6.4 also shows the data obtained for the magnetized sample A after addition of 10 mM $LiNO_3$, which at low concentration leads to faster rotation than without added salt.

Figure 6.6 shows how the low-frequency limit of the susceptibility spectrum, χ_{LF}, increases linearly with the susceptibility in the high-frequency limit, χ_{HF}. χ_{LF} is proportional to the number concentration of single microparticles (6.14) and χ_{HF} is proportional to the number of Néel relaxing particles. The deviation from linearity at the two highest concentrations indicates that a fraction of the microspheres is no longer as free to rotate and therefore no longer contributes to χ_{LF}. In Figure 6.7, a susceptibility spectrum is shown before and after a full removal of solvent by evaporation. The particles in the dry powder are not moving and as a result only the χ_{HF}-component

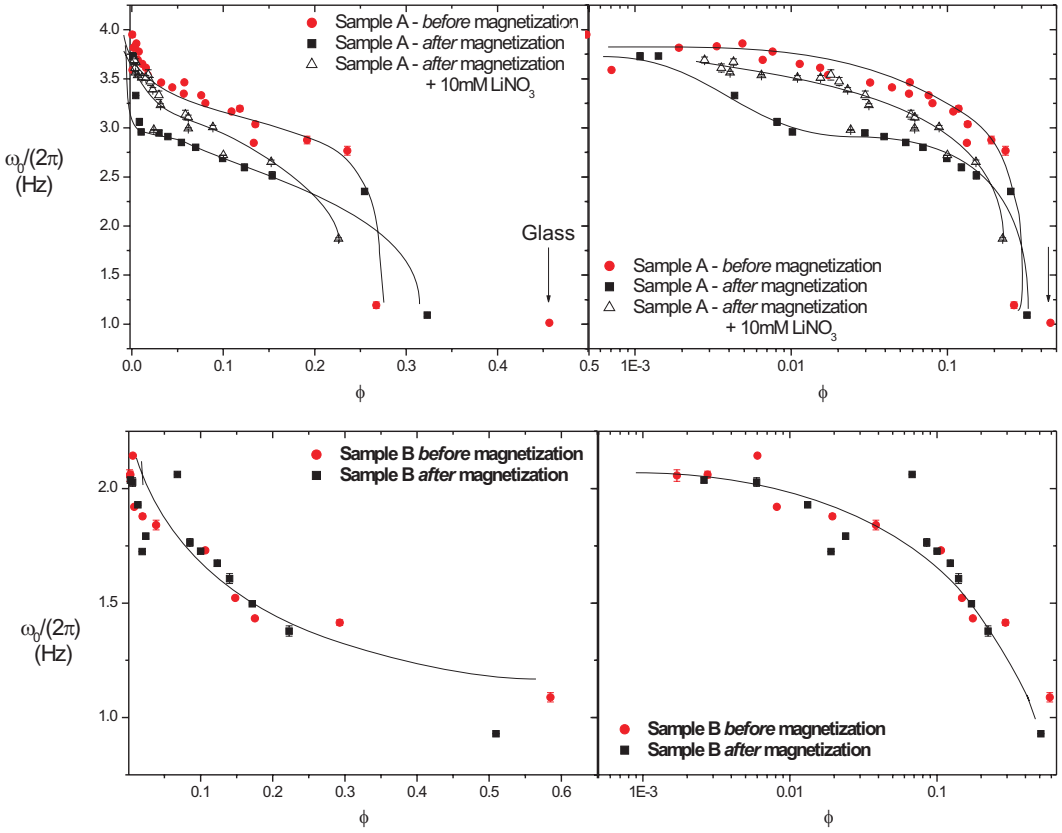

FIGURE 6.4. The characteristic frequency, $\omega_0/(2\pi)$ as a function of volume fraction for samples A and B. Left: linear scale, Right: logarithmic scale. The arrow indicates a point measured on a colloidal glass of the particles in sample A before magnetization, obtained by sedimentation in a centrifuge at 20 g. The solid curves are a guide to the eye.

of the complex magnetic susceptibility remains. This confirms that the characteristic frequencies displayed in the previous figures correspond to rotation of the colloidal particles.

6.5. Discussion

Magnetic properties and magnetic interactions

The rotational diffusion of the magnetic silica spheres is clearly affected by their interaction potential: exposure of the particles to a saturating magnetic field increases their magnetic moment and decreases the characteristic frequency, ω_0 (see Figure 6.4). Two questions arise concerning the magnetic dipole interaction between the type of composite particles used in our experiments: (a) Is the interaction sufficiently weak that it can be treated as an effectively isotropic interaction and (b) what is the influence of

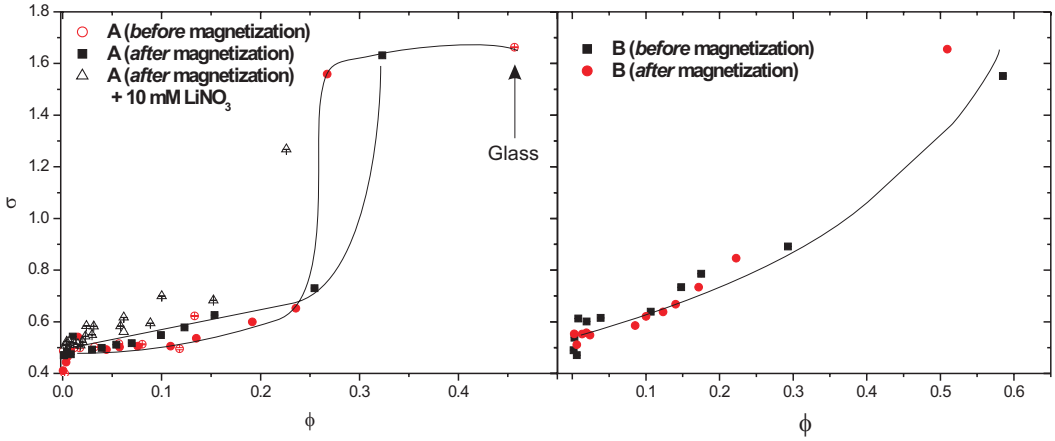

Figure 6.5. The distribution width, σ of the characteristic frequency as a function of volume fraction (6.16). The solid curves are a guide to the eye.

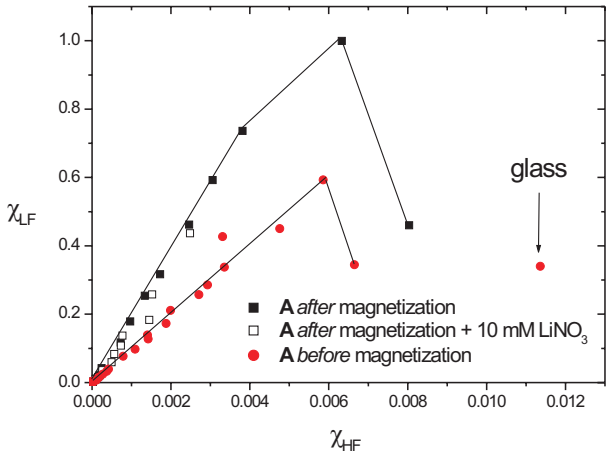

Figure 6.6. The low-frequency limit of the susceptibility spectrum, χ_{LF} as a function of the susceptibility in the high-frequency limit, χ_{HF} which is proportional to ϕ. The deviation from linearity at the two highest concentrations indicates that a fraction of the microspheres is no longer free to rotate and therefore does not contribute to χ_{LF}. The solid lines are a guide to the eye, and the arrow indicates the point measured on the particles from sample A in a glassy state obtained by centrifugation at 20 g.

the fact that the particles are not point dipoles but instead have a shell of magnetic nanoparticles?

Attractive magnetic dipole interactions. The interaction between two permanent magnetic point dipoles in arbitrary orientations is given by (6.7). When the prefactor $\mu_0\mu^2/(4\pi r^3)$ exceeds k_BT, the head-to-tail configuration starts to dominate, especially at high concentrations, and experiment and theory indicate the formation of dipolar chains consisting of two or more particles [27, 62, 128].

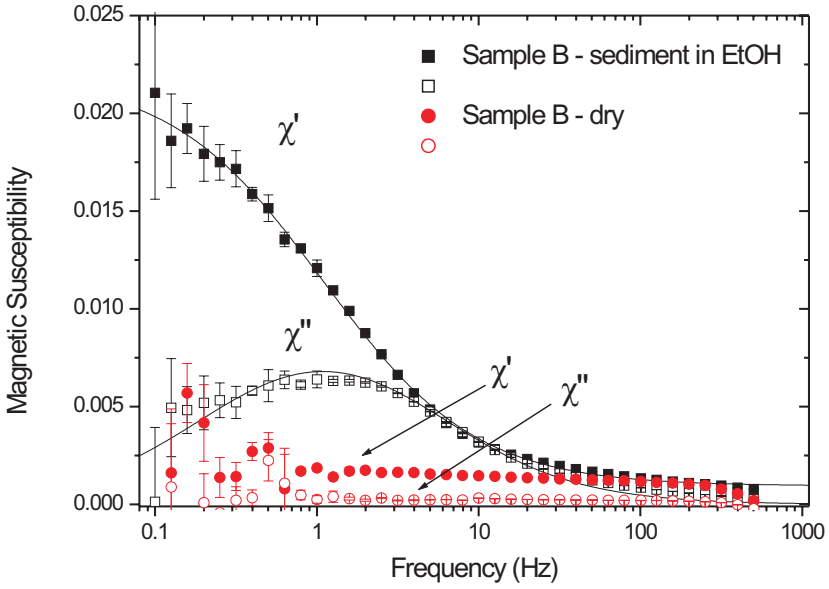

Figure 6.7. Frequency-dependent complex magnetic susceptibility spectra for the sedimented particles in sample B and the same sample as a dry powder after evaporation of the solvent. In the sediment of sample B, a fraction of the particles is restricted from moving, as was shown in Figure 6.6. However, it is clear that the sediment still has a much higher susceptibility than when the particles are not moving at all as in the dry powder. The microparticles in the powder no longer exhibit Brownian motion and as a result, only the Néel-relaxing nanoparticles are detected, with a much weaker frequency dependence, since the characteristic frequency of the Néel relaxation is much higher.

The maximum dipolar interaction energy is achieved when two particles are in contact and when the particle dipole moments are aligned in the head-to-tail configuration: $U_{max} = \mu_0\mu^2/(2\pi d^3)$ (6.7). For our particles, U_{max} lies clearly below $2k_BT$, even after treatment in a saturating magnetic field (Table 6.2), indicating that long-lived dipolar structures are absent. Furthermore, from the characteristic frequencies of the order of 4 Hz, the formation of dipolar structures that exist longer than about 40 ms can be excluded based on the experimental susceptibility spectra. The smallest dipolar structures would be doublets, whose rotational diffusion can be approximated by that of a spherocylinder of aspect ratio $L/d = 2$, leading to a characteristic frequency lower than that of a single sphere by a factor of 5 [106]. In Figure 6.8, calculated complex magnetic susceptibility spectra are shown for a simple shift of the characteristic frequency without doublet formation (Figure 6.8 A) and for the appearance of doublets at the cost of single particles (6.8 B). These can be compared to the experimentally obtained spectra, of which one example is given in Figure 6.8 C. In the experiments, the characteristic frequency remains around the value expected for single sphere rotation (Eqns 6.1 and 6.15) and the shifts in ω_B are simple shifts similar to what is shown in Figure 6.8 A.

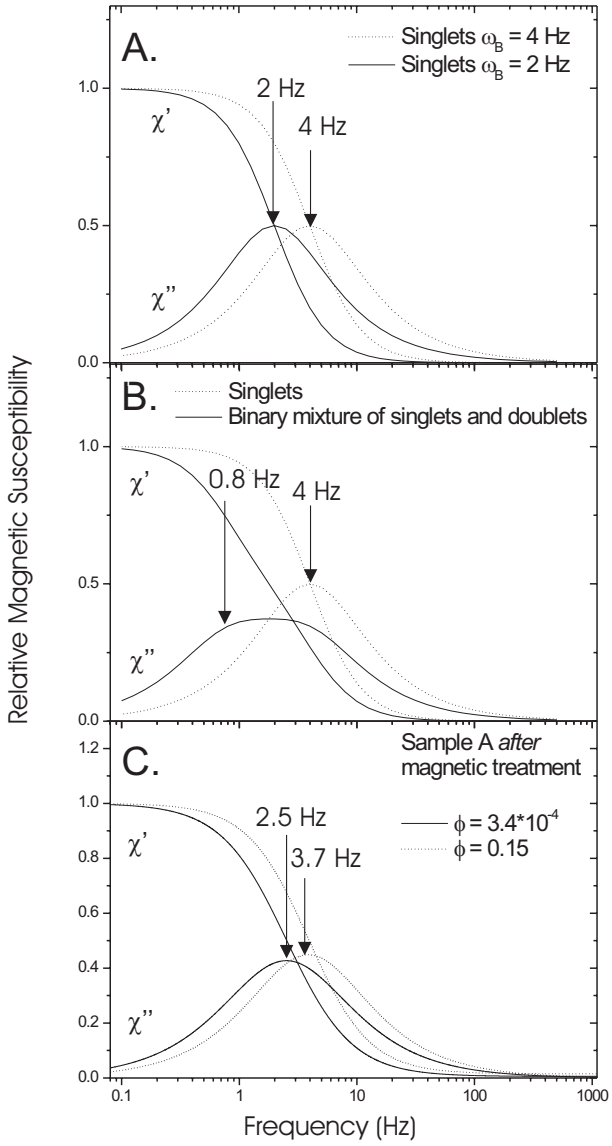

Figure 6.8. The effect of (A) a simple shift of the characteristic frequency of a susceptibility spectrum of single particles of $R_h = 230$ nm without formation of doublets, (B) the effect on the susceptibility spectrum upon formation of doublets at the expense of singlets and (C) experimentally obtained spectra for dilute sample A before magnetic treatment and at $\phi = 0.15$ for the same particles after magnetic treatment. In the experimental curves, the shift to lower frequencies at the higher concentration is not large enough to correspond to doublets or larger structures.

We conclude that long-lived dipolar structures, *i.e.*, structures that would rotate as new entities rather than as separate spheres, are absent in our colloidal dispersions. It therefore seems reasonable to assume that the magnetic interaction can be treated as an isotropic attraction whose distance dependence is given by (6.8).

Effect of position of the magnetic nanoparticles inside the microspheres. The second issue affecting magnetic dipole attraction between the silica spheres is that they are not

point dipoles but have a shell of magnetic nanoparticles. The magnetic dipole moment of a silica particle is given by the vector sum of the dipoles in the magnetic shell [124]. In the case of two silica dipolar particles with all nanoparticle dipoles parallel to each other in the head-to-tail configuration, it can be seen qualitatively why the attraction is stronger when the nanoparticles are in a shell (Figure 6.9 A) rather than at the centre of the particle (Figure 6.9 B). Compared to the case where the nanodipoles are at the centre of the microparticles, the weak attractions between far removed dipoles are more than compensated by the strong interactions between nearby nanoparticle dipoles, due to the r^{-3}-dependence of the interaction between dipoles (6.7).

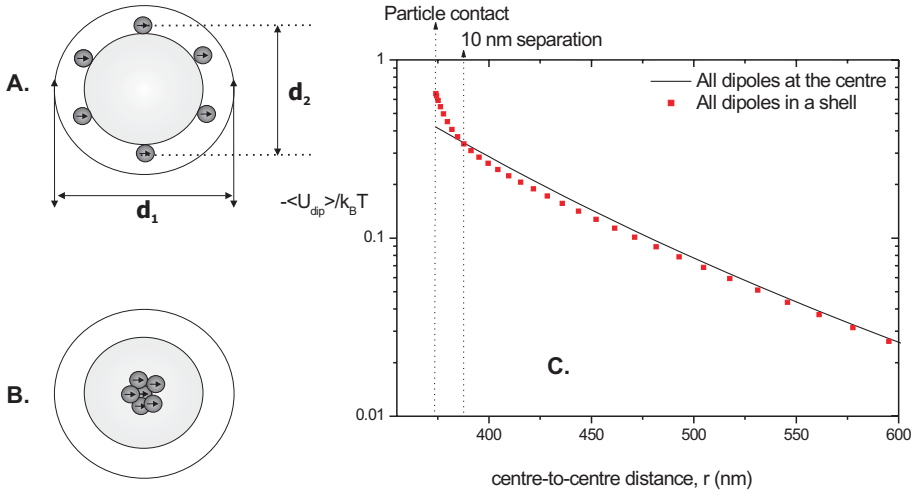

Figure 6.9. Left: Schematic illustration to compare the attraction between composite colloidal particles of diameter d_1 with magnetic nanoparticles embedded (A) in a shell of diameter d_2 and (B) at the centre. Right: Numerically calculated dipolar interaction potentials $< U_{dip} > /k_BT$ as a function of centre-to-centre distance between composite spheres as sketched in 6.9 A and B. The total diameter was chosen as $d_1 = 375$ nm and the diameter of the shell of magnetic nanoparticles with 342 evenly distributed parallel magnetic dipoles adding up to a microparticle magnetic moment of $4 \cdot 10^{-17}$ Am^2 was chosen as $d_2 = 355$ nm and $d_2 = 0$ respectively. At a particle separation of >10 nm, the interaction potential for the silica particles with a shell of magnetic nanoparticles closely approximates the interaction potential for point-dipoles.

Numerical calculations were performed of the dipolar interaction between composite spheres as in Figure 6.9 A with an outer diameter $d_1 = 375$ nm, a microparticle dipole moment of $4 \cdot 10^{-17}$ Am^2 and 342 parallel magnetic nanoparticle dipoles evenly distributed on an inner shell of diameter $d_2 = 355$ nm. This roughly corresponds to the particle in sample A, where the outer silica shell is only ~ 10 nm. The weighted average interaction $< U_{dip} >$ was calculated with Boltzmann weights $exp[-U_{dip}/(k_BT)]$ by adding the contributions of all pair interactions between nanoparticle dipoles, taking into account their orientations and spatial positions. At each distance between the microparticles, the weighted average interaction was calculated by integration across

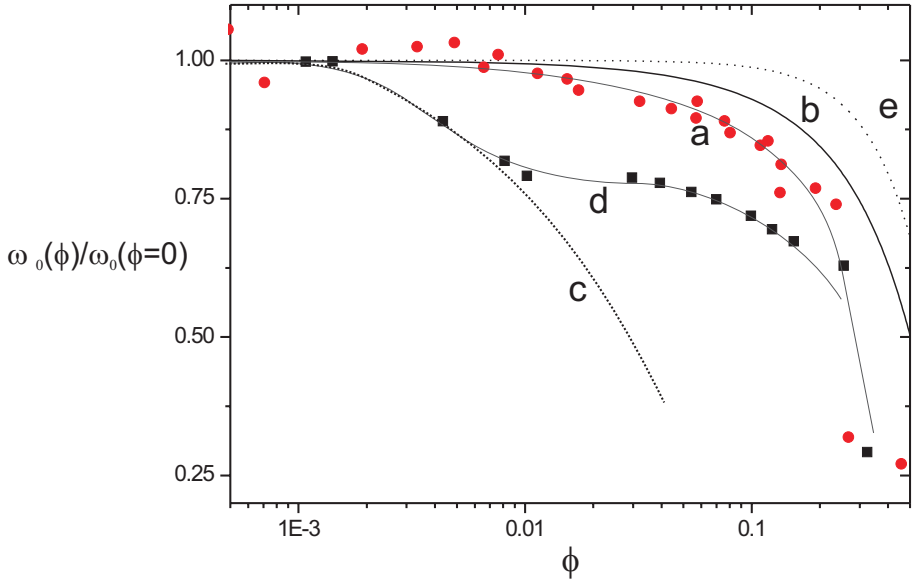

Figure 6.10. Comparison of experimental results of magnetic silica particles in sample A, before (a) and after (d) increasing the dipole moment, with calculated values for hard spheres (b, Eqn. (6.2)) and charged spheres (e, Eqn. (6.3)). Curve c is a hypothetical curve for the expected $\omega_0(\phi)$-profile due to dipole-dipole interactions only.

all possible orientations of both microparticles. The result is shown in Figure 6.9 C. A control of the calculation is that for $d_2 = 0$ (all nanoparticles at the center, as in Figure 6.9 B), the numerical calculation agrees with (6.8) for point dipoles. A control of the sampling of configurations during numerical integration over different orientations is that the unweighted average interaction was found to be zero within digital accuracy. For a separation of the magnetic shells of $r = 10$ nm, the result for $d_2 = 355$ nm is almost indistinguishable from the calculation for $d_2 = 0$. Since already the thickness of the outer silica layer of the studied particles exceeds 10 nm, we can conclude that it is a good assumption to treat the microparticle dipoles as point dipoles.

Influence of dipolar interactions on rotational diffusion

A clear result of our experiments is that the characteristic rotational frequency depends on the dipolar interactions between the particles (Figure 6.4). When the permanent dipole moment of the particles is increased by magnetic treatment, the dipole-dipole interactions are enhanced and particle rotation slows down. However, two remarkable observations deserve discussion: the rotational retardation after dipole moment enhancement is only a weak function of the volume fraction above $\phi = 0.01$, and salt addition does not decelerate rotation but accelerates it.

Before increasing the dipole moment of the microparticles (see Figure 6.10, curve a), rotational diffusion is already somewhat slower than for hard spheres (see Figure 6.10, curve b). If the increased dipole moments would only lead to further attraction between the particles, the rotational diffusion is expected to decrease more and more rapidly as

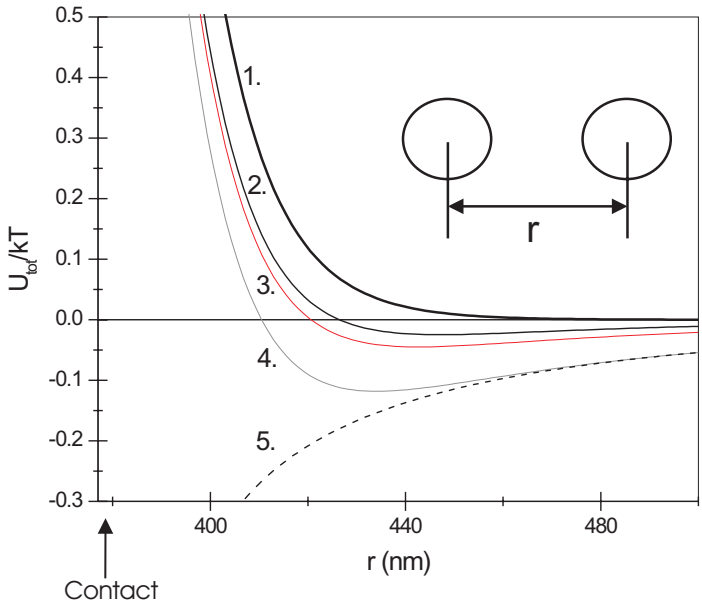

FIGURE 6.11. Calculated overall interaction potentials, U/k_BT, as a function of the interparticle centre-to-centre distance, r, based on Eqs 6.4, 6.6, 6.8 and 6.9 for particles with $Z = 1500$ [48], $\kappa^{-1} = 12$ nm, $H \approx 3 \cdot 10^{-21}$ J and $R = 187$ nm: 1) Electrostatic repulsion; 2) electrostatic repulsion and van der Waals attractions; 3) and 4) electrostatic repulsion and van der Waals attractions in combination with dipole-dipole interaction for $\mu = 2.5 \cdot 10^{-17}$ Am^2 and $\mu = 3.6 \cdot 10^{-17}$ Am^2. Curve 5 is the same as in 4, but with a Debye-length of 2 nm, illustrating the effect of dispersing the particles in a 10 mM monovalent salt solution.

a function of volume fraction (curve c Figure 6.10). What is observed, however, is a fast initial retardation below a volume fraction of $\phi = 0.01$, above which the rotation rate is no longer a strong function of volume fraction (curve d in Figure 6.10). This result cannot be accounted for only on the basis of increased hydrodynamic interaction due to attraction-induced shortening of interparticle distances. One tempting explanation would be that above $\phi = 0.01$, the decrease of the time-averaged distance between neighbouring particles at increasing the volume fraction is counteracted by electrostatic repulsion. This would set a minimum distance between interacting particles and thus limit retardation of rotation due to dipolar attraction. However, at a volume fraction of $\phi = 0.01$, the average centre-to-centre interparticle distance is still of the order of $0.01^{-1/3} \sim 5$ particle diameters, whereas the Debye length in our systems without added salt is only $\sim 3\%$ of one particle diameter (see Section 6.3).

The length scales of the interactions are illustrated in Figure 6.11, calculated on the basis of Eqs (6.4), (6.6), (6.8) and (6.9), using a particle radius of 187 nm and the measured ion concentrations in our system before and after salt addition. Typical values of the charge per surface area of TPM-coated Stöber-silica spheres in ethanol [48]

were used and a Hamaker constant of silica in ethanol was estimated from an approximate expression given in Ref. [129]. Figure 6.11 illustrates that it is difficult to ascribe the relatively abrupt change in rotational dynamics around $\phi = 0.01$ to electrostatic repulsion, when the average interparticle distance is still far below values where the electrostatic double layers of neighbouring particles are overlapping. Moreover, if electrostatic repulsion were to favour rapid rotation, salt addition should diminish that effect and lead to slower rotation due to the much increased attraction between the particles. Our experiments, contradict this expectation: addition of salt not only fails to slow down the rotation of particles, but even slightly enhances it.

It is concluded that at concentrations above $\phi = 0.01$, an effect is present that accelerates particle rotation at increasing colloidal concentration and that counteracts the retardation that is due to increasing hydrodynamic and dipolar interaction. On a microscopic level, there is apparently a mechanism by which the rotation of one particle facilitates that of its neighbours as the particles come closer together. To understand this, we propose that not only dipole-dipole interactions should be taken into account, but also the interaction of the particle dipoles with the applied alternating magnetic field that probes the rotational motion of the particles.

Figure 6.12 sketches the time dependence of the orientation of the external magnetic field and of the dipolar particles. The applied field is up or down and its magnitude varies sinusoidally. The equipment measures the resulting magnetization of the sample, which depends on the orientations of the dipolar particles. Even when the strength of the applied field passes a maximum, particle alignment is only partial, since a weak magnetic field amplitude is used. When the field passes zero, the dipoles start to rotate towards the steady state orientation distribution that corresponds to the instantaneous applied field. In Table 6.2, values are given for the maximum dipolar interaction between the particles, U_{max}, and the interaction energy, $\mu\mu_0 H$ for the dipoles with the applied field. For the studied particles, the interaction with the field is on the order of $\mu\mu_0 H =$ 0.4-0.6 $k_B T$. Interaction with the field is only negligible when $\mu\mu_0 H << k_B T$, which is not the case. The alignment of the particle dipoles with the applied field can therefore not be regarded as purely diffusive.

The cooperative alignment of dipolar particles above a threshold concentration could be explained if doublets were formed. The interaction with the external field would be twice as strong as for single particles. This would explain why the increase in particle concentration (decrease in average distance between the particles) and addition of salt (decrease in distance of nearest approach) both lead to an acceleration of the particle rotation. However, as discussed in the previous section, the dipole-dipole interactions are not strong enough to form long-lived doublets or larger anisotropic structures. Nevertheless, the maximum dipole-dipole interaction for the particles in sample A is far from negligible: $\sim 0.6\ k_B T$ before and $\sim 1.2\ k_B T$ after magnetic treatment at 2 T.

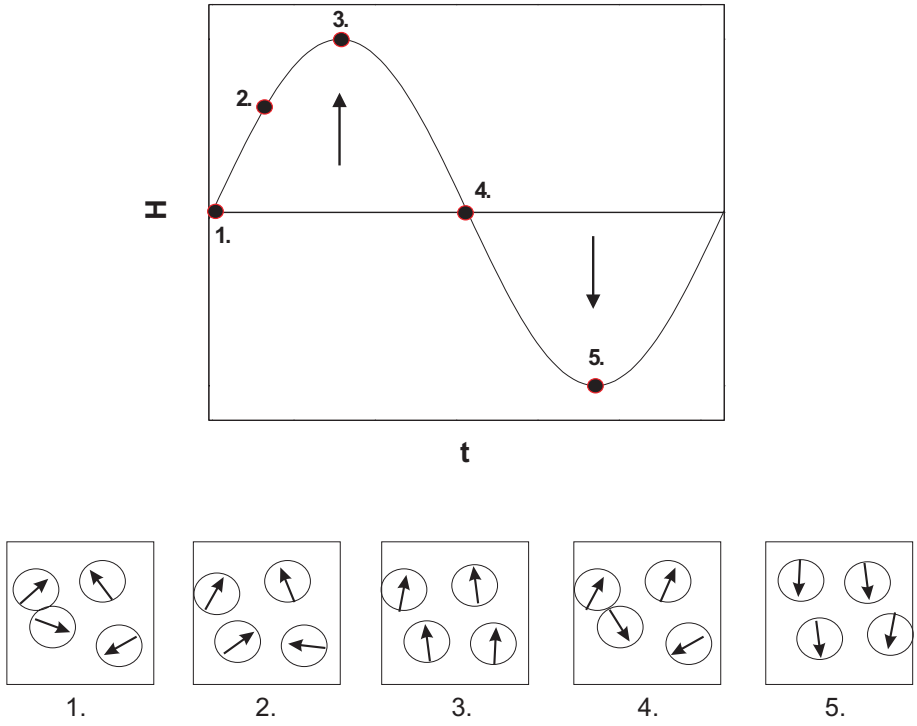

Figure 6.12. Illustration of the time dependence of the orientation of the external magnetic field and of the dipolar particles during complex magnetic susceptibility measurements. The equipment measures the resulting magnetization of the sample, which depends on the orientations of the dipolar particles. Even when the strength of the applied field passes a maximum, particle alignment is only partial, since a weak magnetic field amplitude is used.

Although not strong enough to form long-lived doublets, these particles could form short-lived doublets as they come into contact with each other while diffusing around. The life-time of such short-lived doublet can be roughly estimated based on the time that it takes for the particles to diffuse approximately one particle diameter apart after particle encounter. Particles with an attractive interaction potential of $\sim 1k_BT$ then have a doublet life-time on the order of 10 ms. This is long enough to assist alignment with the field during half a period of the sinusoidally alternating field, leading to an enhanced particle rotation rate.

At the lowest concentrations, particle contact and formation of short-lived doublets is much less frequent than at higher concentrations. The long-ranged dipole-dipole interactions can slow down the rotational diffusion and shorten the average distance between the particles, thereby enhancing the hydrodynamic interactions in the system.

Our explanation implies that particle rotation is no longer purely diffusive in our systems above $\phi = 0.01$, but that it is assisted by the external field and by dipole-dipole interactions. Below $\phi = 0.01$, the concentration is low enough for the rotation of particles to be purely diffusive. In future applications, when the objective is to

measure the rotational diffusion rate at high concentrations of the magnetically labelled particles ($\phi > 0.01$), the magnetic interaction should remain weaker than in system A after magnetic treatment. This suggests that the head-to-tail contact interaction energy should be kept well below k_BT to use the particles as probes of rotational diffusion at high concentrations. To realize this, lower amounts of or less strongly magnetic material should be used and the magnetic nanoparticles should be embedded far enough below the surface of the microparticles to avoid enhanced dipolar interaction (Figure 6.9). Moreover the magnitude of the alternating magnetic field could be decreased even further as long as the signal-to-noise ratio remains sufficiently high.

6.6. Conclusions

We have demonstrated that frequency-dependent complex magnetic susceptibility measurements can be employed as a new experimental method to study rotational diffusion in colloidal systems, provided that the particles are labelled with thermally blocked magnetic dipoles and that the particle dipole moment remains small (head-to-tail contact interaction $<< k_BT$). This method has the advantage that it can be applied to colloidal particles of various shapes and in the size range of 5-500 nm in radius, without refractive index matching. Even materials that strongly absorb or scatter light can be studied. The technique allows direct measurements of the rotational diffusion coefficient and the width of its distribution over the full range of volume fractions without using host-tracer systems. Moreover, colloidal particles with attractive dipolar and/or van der Waals interactions can be studied, since this magnetic technique is not sensitive to optical scattering or absorption. This opens up possibilities to examine the rotational diffusion of a variety of complex colloidal systems such as anisotropic and/or dipolar particles as well as particles in various solvents or confined geometries.

Using this technique we have been able to perform an experimental study of the concentration dependence of the Brownian rotation for charged colloidal silica spheres with an intrinsic, permanent dipole moment. The results show that dipolar interactions between the particles lead to a faster initial decay of the rotational diffusion coefficient as a function of the volume fraction than for hard spheres or charged spheres. At volume fractions $\phi > 0.01$, magnetic coupling between the dipole moments accelerated particle rotation in the alternating external field, and rotation was no longer purely diffusive.

We have also shown that a slightly thicker outer shell partially screens the magnetic interactions, which means that by growing an outer non-magnetic layer, the particles eventually behave as charged spheres and the magnetic particles are only acting as a probe for the rotational diffusion measurements.

7

Light Scattering from Silica-Iron Oxide Core-Shell Colloids

Abstract

Static light scattering measurements have been performed on colloidal dispersions of silica particles with two concentric shells one of which contains light-absorbing iron oxide nanoparticles with a high refractive index. For inhomogeneous spherical particles in the RGD approximation, the angular scattering intensity profiles as a function of the optical contrast yield information about particle size and particle refractive index. Here we investigate to what extent the contrast variation method based on RGD theory can be applied to silica spheres with an internal iron oxide shell.

7.1. Introduction

For sufficiently small, non-absorbing particles the angular static light scattering profile can be calculated within the so-called Rayleigh-Gans-Debye approximation instead of using the full, complex Mie-theory for light scattering [118]. The RGD approximation is valid when the phase shift of light in a particle is sufficiently small. Also for larger particles, with a diameter comparable to the wavelength of light, the RGD approximation may hold, provided that the difference in refractive index between the particle and the surrounding medium, often referred to as the optical contrast, is small. For optically inhomogeneous particles in the RGD approximation, measurements of the angular scattering intensity profiles as a function of optical contrast are useful to determine the average refractive index of colloidal particles [53,71,130]. Moreover, contrast variation experiments also provide information about the internal refractive index profile, as demonstrated for colloidal spheres with a core-shell morphology [53, 71].

The core-shell particles described in this thesis contain a layer of magnetic iron oxide nanoparticles which not only have a high refractive index but also absorb light. The layer thickness is small compared to the overall particle size but, nevertheless, the question is justified whether or not the iron oxide-containing silica spheres can be adequately analysed within the RGD approximation.

In this Chapter we report on contrast variation experiments to explore the applicability of the RGD theory to our magnetic silica spheres. Topics to be investigated are the change in the angular scattering intensity profiles as a function of optical contrast, the possibility of determining the particle size from iso-scattering points and the determination of the average particle refractive index.

7.2. Theoretical background

The scattering of light from a homogeneous spherical particle was first described by Gustav Mie [131] who solved Maxwell's equations for the interaction between an electromagnetic wave and a sphere. The Mie-theory was extended by Aden and Kerker [132] to inhomogeneous particles with a core-shell structure. However, for sufficiently small spheres or spheres with a low optical contrast these rather extensive Mie-calculations can be simplified within the so-called Rayleigh-Gans-Debye (RGD) approximation. For such particles it has previously been described how contrast variation in static light scattering can be applied to optically inhomogeneous spheres with a core-shell morphology, usually silica or latex particles with adsorbed stabilizing polymer layers [71, 130], to obtain the average particle size and refractive index.

Below, we first review the relevant equations for light scattering contrast variation applied to a colloidal sphere and extend them to spheres containing a core and two

concentric shells. More detailed contrast variation theory can be found in refs [71, 118, 133–135].

The average refractive index of a sphere with total radius R and volume V is

$$n_p = \frac{1}{V}\int_0^R n(r)4\pi r^2 dr, \tag{7.1}$$

where $n(r)$ is the refractive index at a distance r from the centre of the sphere. When the sample is illuminated by vertically polarized light, the intensity of the scattered light is expressed in terms of the Rayleigh ratio, $R(k)$, via:

$$R(k) = \frac{2\pi^2 c}{\lambda_0^4 \rho V} n_s^2 B^2(k) S(k), \tag{7.2}$$

where c is the mass concentration of particles, ρ is the particle mass density and V is the particle volume. $S(k)$ is the structure factor, equal to unity for a dilute dispersion and $B(k)$ is the scattering amplitude. The wave vector k is defined as:

$$k = \frac{4\pi n_s}{\lambda_0} sin\left(\frac{\theta}{2}\right), \tag{7.3}$$

where n_s is the solvent refractive index, θ is the scattering angle and λ_0 is the wavelength of the incident light *in vacuo*.

The average optical contrast, $n_p - n_s$, is the difference in average refractive index between particle and solvent. The difference $n(r) - n_s$ will be referred to as the local contrast. Within the Rayleigh-Gans-Debye (RGD) approximation, *i.e.*, when

$$\frac{4\pi R}{\lambda} \mid n_p - n_s \mid \ll 1, \tag{7.4}$$

the Fourier transform of $n(r) - n_s$ is the scattering amplitude, $B(k)$ [118]:

$$B(k) = \int_0^R (n(r) - n_s)\frac{sin(kr)}{kr} 4\pi r^2 dr. \tag{7.5}$$

This scattering amplitude can, as proposed in Ref. [71], be divided into the scattering contribution from a homogeneous sphere, $B_0(k)$, and the scattering contribution arising from inhomogeneities inside the sphere, $\varepsilon(k)$:

$$B(k) = B_0(k) + \varepsilon(k) \tag{7.6}$$

For a homogeneous sphere, $n(r) = n_p$, and the scattering amplitude for a homogeneous sphere is found from 7.5 to be:

$$B_0(k) = \frac{4\pi}{k^3}(n_p - n_s)[sin(kR) - (kR)cos(kR)] \tag{7.7}$$

The particle radius of homogeneous spheres can be obtained from the minima in the corresponding scattering intensity profile, according to Eqn 7.5 located at the solutions of $tan(kR) = kR$, namely $kR = 4.4935$, 7.7253 etc.

For inhomogeneous spheres, the locations of scattering intensity minima may shift considerably as a function of the average optical contrast and, consequently, the particle

radius cannot be calculated directly from the intensity minima. As discussed elsewhere in more detail [71], contrast variation experiments may nevertheless form a valuable tool to determine for instance the size and average particle refractive index of inhomogeneous spheres. The scattering curves will shift upon changing the contrast, but at certain k-values k_m for which $B_0(k)$=0, iso-scattering points will appear in $B(k)$, which will only depend on the inhomogeneities $\varepsilon(k)$ which are independent of the optical contrast [71]:

$$\varepsilon(k) = \int_0^R \Delta n(r) \frac{sin(kr)}{kr} 4\pi r^2 dr \tag{7.8}$$

$$\varepsilon(k) \approx -\frac{k^2}{6} \int_0^R (n(r) - n_p) 4\pi r^4 dr \tag{7.9}$$

Here $\Delta n(r) = n_r - n_p$ is the local fluctuation of the refractive index around the average n_p. Eqn 7.9 is first term in the small-k expansion of Eqn 7.8. The iso-scattering points are located at wave vectors for which $B_0(k) = 0$ such that $k_m R = 4.4935$, 7.7253 etc. Hence, the total radius of inhomogeneous particles can in principle be determined from these iso-scattering points as confirmed by studies on silica [71] and latex spheres [130].

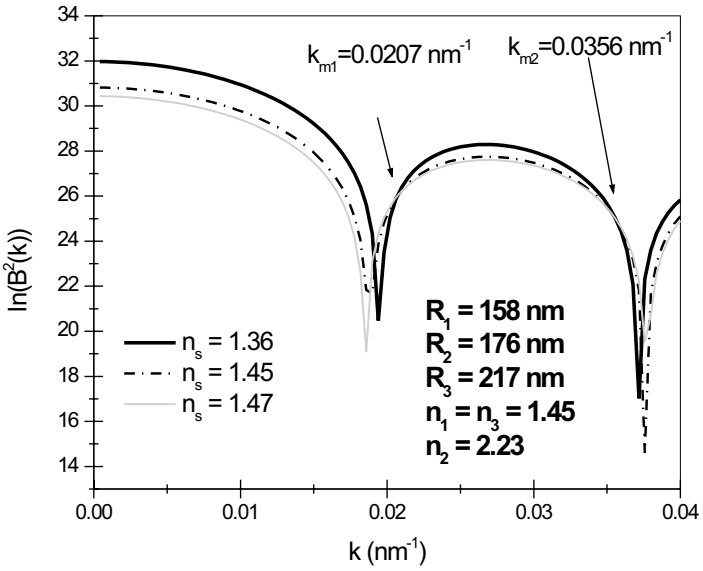

Figure 7.1. Scattering intensities at three different optical contrasts calculated using RGD-theory for inhomogeneous particles with two concentric shells (Eqn. 7.14), consisting of a silica core, an iron oxide containing shell and an outer silica shell. The particle profile (see Figure 7.2) was chosen as $R_1 = 158$ nm, $R_2 = 176$ nm and $R_3 = 217$ nm and the refractive index profile as $n_1 = n_3 = 1.45$ and $n_2 = 2.23$. The arrows indicate the first and second intersection point, which correspond to the total particle radius, 217 nm.

Contrast variation can be also used to determine the average refractive index of particles [71]. For a dilute system, it can be assumed that $S(K) = 1$ and Eqn 7.2 can

be rewritten as:

$$B(k) = \frac{1}{n_s}\sqrt{R(k)\frac{\lambda_0^4 \delta V}{2\pi^2 c}} \tag{7.10}$$

Substituting for $B(k) = B_0(k) + \varepsilon(k)$, Eqs 7.6 and 7.7 lead to the following expression for n_p when $B(k) = 0$:

$$n_s = n_p + \frac{k^3 \varepsilon(k)}{4\pi[sin(kR) - (kR)cos(kR)]}, \tag{7.11}$$

From this expression it follows that indeed for homogeneous particles ($\varepsilon(k) = 0$), $B(k)$ $= 0$ when the particle and the solvent refractive refractive indices are matched, *i.e.* n_p $= n_s$, independent of k.

For inhomogeneous particles, $\varepsilon(k) \neq 0$ and the average particle refractive index n_p equals n_s only when $k = 0$, which is not experimentally accessible. However, by extrapolation of B(k) to zero (Eqn. 7.10), one can obtain the solvent refractive index, n_0, for which $B(k) = 0$ also for inhomogeneous particles. From Eqs 7.10, 7.9 and 7.11, it follows that for sufficiently small k:

$$n_0 = n_p - \frac{k^2}{6V}\int_0^R (n_p - n(r))4\pi r^4 dr. \tag{7.12}$$

The average particle refractive index, n_p, can therefore be obtained from a plot of n_0 as a function of k^2 by extrapolation to $k = 0$, for which $n_0 = n_p$.

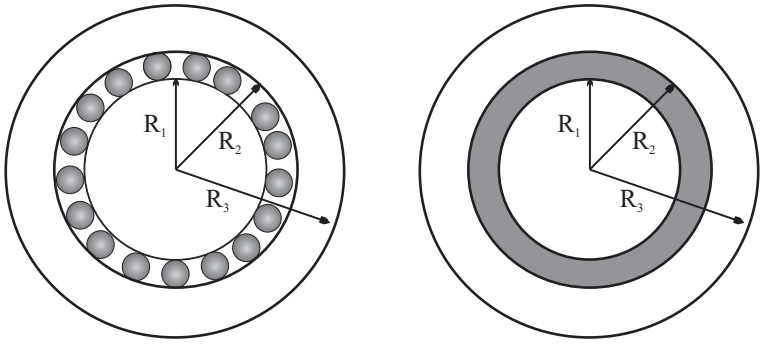

Figure 7.2. Left: Schematic picture of the concentric shell type of particle studied in this work: an inner core decorated with iron oxide nanoparticles followed by a continuous outer shell. Right: The second layer is assumed to be a continuous layer with the same refractive index as of the nanoparticles.

In this work, contrast variation experiments are carried out on silica spheres with a layer of iron oxide particles embedded in an outer silica shell at a well-defined distance from the particle centre as depicted in Fig 7.2. Assuming that the iron oxide layer is

homogeneous, the refractive index profile of such a particle will be:

$$n(r) = \begin{cases} n_1 & ; 0 < r \leq R_1 \\ n_2 & ; R_1 < r \leq R_2 \\ n_3 & ; R_2 < r \leq R_3 \\ n_s & ; r > R_3 \end{cases} \tag{7.13}$$

with the corresponding scattering amplitude

$$B(k) = \frac{4\pi}{k^3}[(n_1 - n_2)f(kR_1) + (n_2 - n_2)f(kR_2) + (n_3 - n_s)f(kR_3)] \tag{7.14}$$

where

$$f(kR_n) = sin(kR_n) - (kR_n)cos(kR_n). \tag{7.15}$$

Scattering from iron oxide-silica particles at the matching point of silica

One particular case of a concentric particle is when core and outer shell both consist of a material with the same refractive index, which is the case for our silica iron oxide particles. If the solvent refractive index equals that of the inner core and outer shell, light is only scattered from the first shell, in our case the iron oxide shell. Under such conditions, when $n_1 = n_3 = n_s$ the scattering amplitude in Eqn 7.14 reduces to:

$$B(k) = \frac{4\pi}{k^3}(n_2 - n_s)[f(k(R_2 - R_1)) - f(kR_1)] \tag{7.16}$$

When the shell thickness is small compared to the core radius, R_1, *i.e.*, if $R_2 - R_1 << R_1$ the scattering amplitude from Eqn. 7.16 approaches that of a hollow sphere [136] (in our case an "iron oxide bubble"):

$$B(k) = 4\pi(n_2 - n_s)(R_2 - R_1)R_1^2\frac{sin(kR_1)}{kR_1} \tag{7.17}$$

Note that the magnitude of this amplitude at k=0,

$$B(k = 0) = 4\pi(n_2 - n_s)(R_2 - R_1)R_1^2, \tag{7.18}$$

depends on the volume of the thin ferrite shell. At finite wave vectors, the scattering from the "bubble" amplitude is zero at $kR_1 = n\pi$ with $n = 1, 2, 3, ...$ Thus from these minima in the angular intensity profile, one can in principle obtain the core radius, R_1.

Turbidity and absorption

The particles in the investigated systems contain cobalt ferrite and maghemite, which are both light-absorbing materials. As a complement to the static light scattering measurements, the turbidity of these particles was measured with a UV-vis spectrophotometer to see whether the particles absorb significantly at the wavelength at which the angular scattering profiles are measured with SLS. The turbidity, τ , in principle contains the same information as static light scattering, but instead of an angular intensity profile, the forward transmission after scattering is measured as a function of

wavelength. Turbidity also includes the absorbance. The intensity of the transmitted light I_t is measured relative to the intensity of the incident light beam, I_0 and the tubidity is obtained from:

$$ln\frac{I_t}{I_0} = -\tau L, \tag{7.19}$$

where L is the optical path length and the turbidity is related to the Rayleigh ratio via:

$$\tau = 2\pi \int_0^\pi R(k) sin\theta d(\theta), \tag{7.20}$$

if the turbidity is only due to light scattering, with no significant contribution from light absorption.

7.3. Experimental system

Contrast variation experiments were performed on dispersions of silica colloids with a diameter $d \sim 300 - 500$ nm with embedded cobalt ferrite and maghemite nanoparticles with an average diameter of $d \sim 20$ nm and $d \sim 10$ nm respectively. These nanoparticles, prepared with a coprecipitation method [42, 43, 45], were chemically bound to the surface of thiol-functionalized Stöber-silica [50]. The core-shell composite particles were encapsulated in an outer silica shell by seeded growth. A detailed description of the particle synthesis can be found in Chapter 2 of this thesis. Silica spheres with embedded cobalt ferrite particles will be referred to here as SiCoF and the spheres with maghemite as SiMag. The composite particles where imaged with a Philips Tecnai12 transmission electron microscope (see Fig 7.3 and Table 7.1).

Table 7.1. Characterization data of the particle dispersions

Particle profile [a]	SiCoF	SiMag
$R_{1,TEM}(nm)$ [b]	158 ± 7	135 ± 9
$R_{2,TEM}(nm)$ [b]	176 ± 20	144 ± 20
$R_{3,TEM}(nm)$ [b]	217 ± 15	153 ± 20
n_1, n_3	1.455 [c]	1.455 [c]
n_2 [d]	2.23[e]	2.63[f]

[a] as in Figure 7.2
[b] Radii obtained from analysis of TEM images.
[c] See Ref. [71]
[d] Assuming a continuous shell of iron oxide nanoparticles.
[e] Obtained from dn/dc measurements (see text).
[f] See Ref. [105]

The refractive index of the cobalt ferrite particles was determined by measuring the refractive index as a function of concentration with an Optilab DSP Interferometric refractometer (Wyatt Technology), operating at $T = 27.5$ ° C and $\lambda = 633$ nm. The

particle refractive index of cobalt ferrite, n_{CoF}, was then calculated from $dn/dc = (n_{CoF} - n_s)/\rho_{CoF}$, with the solvent refractive index, $n_s = 1.33$, and the mass density of n_s cobalt iron oxide, $\rho_{CoF} = 4.91$ g/mL [38]. The experimentally obtained $dn/dc =$

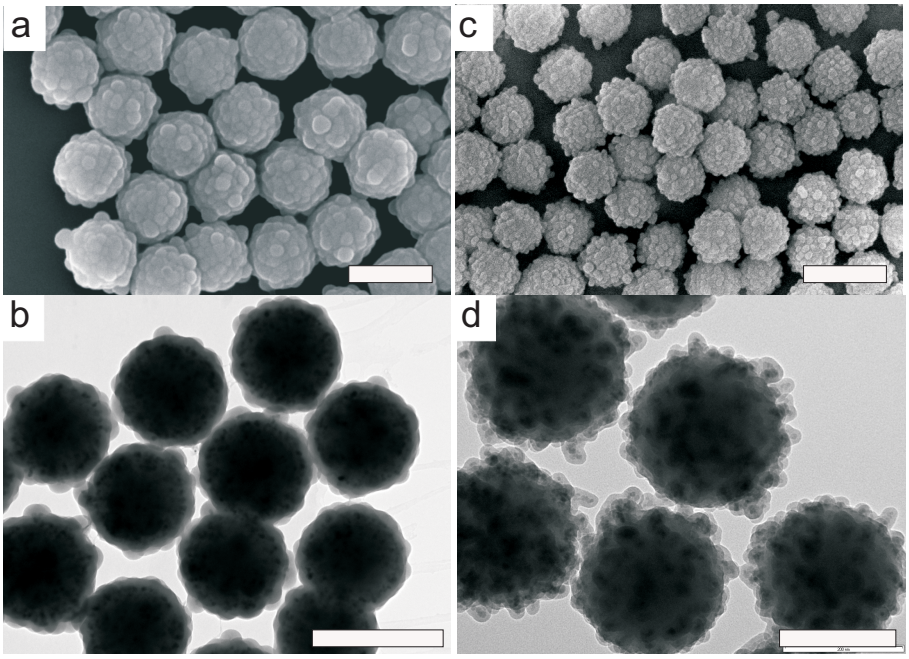

FIGURE 7.3. SEM and TEM micrographs showing the particles from SiCoF (a-b) and SiMag (c-d). The scale bars correspond to 500 nm (a-c) and 200 nm (d).

0.1827 ± 0.0027 mL/g, gives a refractive index for the cobalt iron oxide particles, $n_{CoF} = 2.23$. This refractive index is in the same range as that of other iron oxides, such as maghemite ($n = 2.63$) and nickel ferrite ($n = 2.3$) found in [105].

Series of dilute samples of composite particles in various mixtures of ethanol ($n_{(546.1nm, 25°C)} = 1.361$) and dimethyl sulfoxide, DMSO ($n_{(589nm,25°C)} = 1.478$) [105] were prepared to vary the optical contrast. The particle concentration was kept constant within one series of measurements. The sample preparation was carried out in a dust-free hood, using only glass vials, pipet-tips, and cuvettes, which had been cleaned with ethanol, ultrasonicated, and flushed with distilled acetone prior to use such that no dust or other impurities would be present in the samples. A concentrated dispersion of the silica-ferrite particles in ethanol was filtered through a 5 μm Mitex filter into a glass vial. Thereafter, 15 mL of each solvent mixture was filtered in the same way and 20 μL of the filtered dispersion of silica-iron oxide particles was added to 5 mL of each solvent mixture.

For all measurements, the same quartz cuvette was used, marked such that in each experiment the cuvette was identically positioned in the sample holder to avoid influence of any impurities in the cuvette glass on the angular scattering profile. Figure 7.4a shows scattering curves measured under the same conditions, only varying the position

of the cuvette. This reveals that the position of the cuvette can have a significant influence on the scattering intensity. After placing the cuvette in the sample holder, it was left for 15 minutes to stabilize the temperature inside the cuvette at 27.5 °C. The refractive index of each solvent mixture (after letting the particles sediment completely) was measured with a Jena bench top refractometer. Static light scattering experiments were performed at T = 27.5 °C using a homebuilt automatic setup, equipped with a Hg-lamp which can irradiate the sample with vertically polarized light of wavelengths λ= 435.8, 546.1, and 578 nm. The scattered intensity was measured at 111 angles from 15° to 140°.

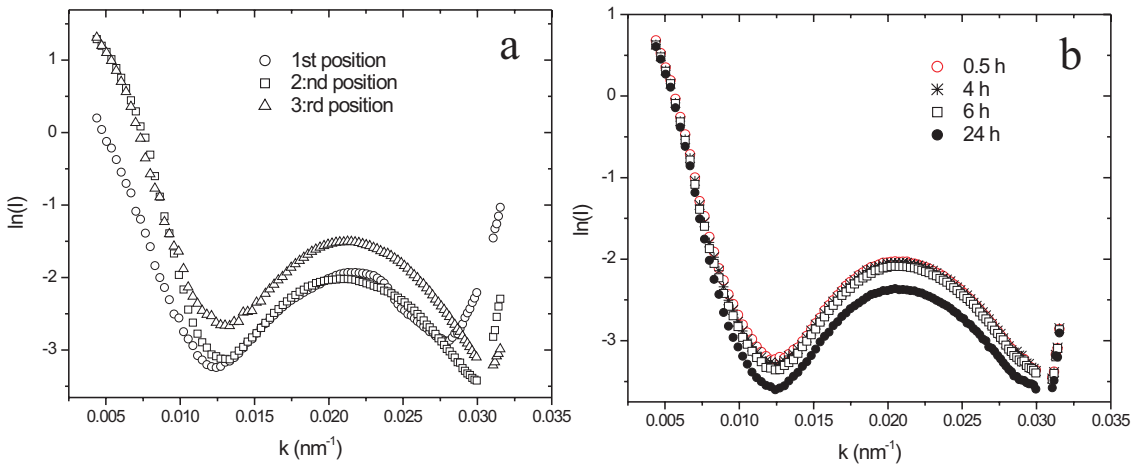

Figure 7.4. a) Scattering curves of SiCoF measured at $\lambda = 546.1$ nm varying the position of the cuvette in the sample holder. b) Scattering curves of SiCoF measured at $\lambda = 546.1$ nm at different times after placing the cuvette in the sample holder. After 4 h a slight decrease in the scattered intensity is observed due to sedimentation of particles. The measurements show that sedimentation will not influence the scattered intensity on the timescale of the measurements ($\sim$ 1 hour).

To ensure that the sedimentation of particles would not influence the measurements on the timescale of the experiments (approximately 1 hour when measuring at several wavelengths), the scattered intensity was measured several times during 24 h with the sample remaining in the same position. These measurements showed a decrease in the scattered intensity only after 4-6 h (see Figure 7.4b).

UV-vis spectroscopy contrast variation experiments were performed on samples of SiCoF with a Varian Cary 1E UV-vis spectrophotometer using a quartz cuvette with an optical path length $L = 10$ mm. The samples were just as for the SLS measurements prepared with the same particle concentration but with a different optical contrast. From a concentrated dispersion of particles in ethanol, 80 μL was added to 5 mL of solvent mixture.

7.4. Results & discussion

Contrast variation experiments with static light scattering

The scattering intensity profiles from the contrast variation experiments are shown for SiCoF in Figure 7.5 and for SiMag in Figure 7.6. As predicted for particles with a refractive index profile as the one for silica-ferrite particles (see Figure 7.2), a shift is observed of the minima in the scattering curves upon varying the optical contrast. Furthermore, the scattering curves have a common intersection point at $k_m = 1.9 \times 10^7$ m^{-1} for the SiCoF-particles and $k_m = 2.8 \times 10^7$ m^{-1} for the SiMag-particles. In the Rayleigh-Gans-Debye approximation, such iso-scattering points give the total radius of the particles from $k_m R_3 = 4.4935$ (see Eqs 7.6 and 7.7). For SiCoF, the intersection point corresponds to a total particle radius of $R_3 = 240$ nm and for SiMag $R_3 = 160$ nm. In both cases the radius found from k_m is in a reasonable agreement with the average radius determined from TEM-images (see Table 7.1). Radii obtained from

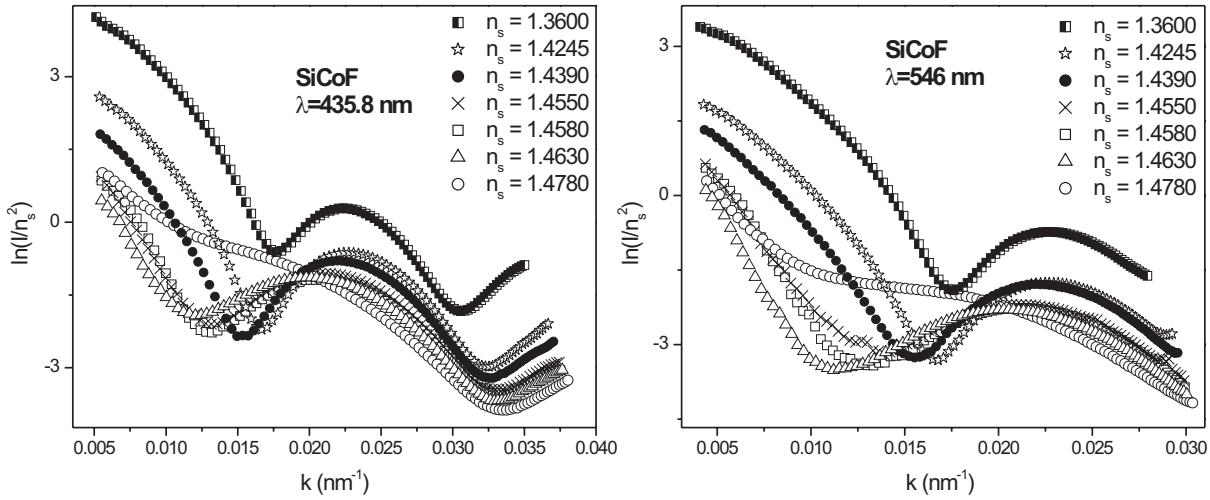

Figure 7.5. Scattering curves, $ln(I/n_s^2)$ vs k, for dilute samples with the same concentration of SiCoF at various optical contrasts measured at $\lambda = 435.8$ nm (left) and at $\lambda = 514.1$ nm (right). Except at $n_s = 1.3600$, *i.e.*, relatively far from the matching point of silica (n=1.455), the curves have a common intersection point at $\approx 1.9 \times 10^7$ m^{-1}, in agreement with light scattering theory for inhomogeneous spheres and results from TEM image analysis.

light scattering measurements are known to be larger than the corresponding radii from image analysis of TEM pictures. One reason for this is in the case of silica that the slightly porous particles tend to shrink in the high vacuum of the electron microscope. Another reason for the difference in particle size is that a volume-averaged radius is measured with SLS compared to the number-averaged sphere radius from image analysis of TEM pictures. For the particles studied here, the difference between the number-averaged and the volume-averaged sphere radius, $< R^3 > / < R >^3 = 1 + 3\sigma^2$ [4], should be on the order of 1 %, whereas for the radii obtained here from iso-scattering points the differences are on the order of 10 %. However, one should keep in mind

here that the rough surface of SiCoF and SiMag particles complicates the definition of the particle radius in the TEM-image analysis. Furthermore, it can be excluded that a shift of the intensity curves is caused by the scattering from dumbbell-shaped particles (two particles fused together), since the scattering profile of dumbbells deviates from spherical particles only at very low k-values [137].

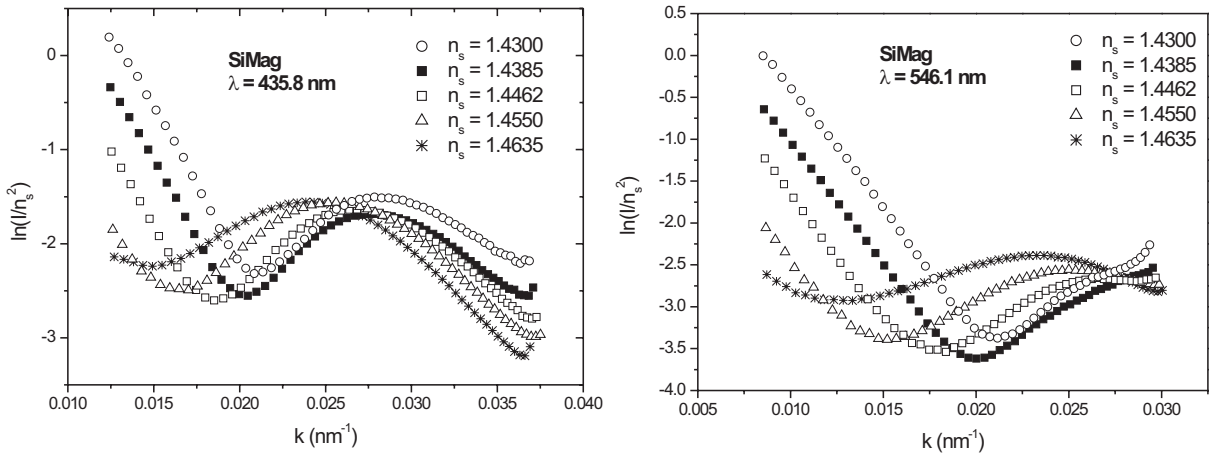

FIGURE 7.6. Scattering curves, $ln(I/n_s^2)$ vs k, for dilute samples with identical concentration of SiMag at various optical contrasts measured at (a) $\lambda = 435.8$ nm and (b) at $\lambda = 514.1$ nm . The curves have a common intersection point (at $k \approx 1.9 \times 10^7$ m^{-1}), in agreement with light scattering theory for inhomogeneous spheres and results from TEM image analysis. As also observed in Figure 7.5 for $n_s = 1.43$, far from the matching point of silica, the scattering curve does not intersect with the rest.

In agreement with Eqns (7.11) and (7.12), it was found that $1/(n_s\sqrt{I})$ varies linearly with the solvent refractive index (see Figure 7.7), except for low k-values, possibly due to larger impurities in the sample, which contribute more to the scattering intensity at low k. The n_0-values are obtained from extrapolation of $\frac{1}{n_s}\sqrt{I} \rightarrow 0$. As explained in Section 7.2, the average particle refractive index can be obtained from contrast variation by extrapolating $n_0(k)$ to k=0. For the SiCoF particles, an average particle refractive index $n_p = 1.49$ was found from the plot in Figure 7.8a and for SiMag $n_p = 1.48$ was extracted from the plot in Figure 7.8b. These values are lower than the expected values (~ 1.6 for both samples) based on the refractive index profiles given for the studied particles in Table 7.1. A possible explaination for the lower refractive index is that the iron oxide shell is not continuous as assumed in Figure 7.2

Optical contrast variation measurements performed with UV-vis spectroscopy are shown for SiCoF in Figure 7.9. These spectra show that when the optical contrast between the solvent and the silica in the particles is relatively high, there is a slow decay of the absorption upon increasing the wavelength. However, as the refractive index of the solvent approaches that of silica, there is an abrupt change of the shape of the spectrum and the absorption at low wavelengths increases, suggesting that scattering

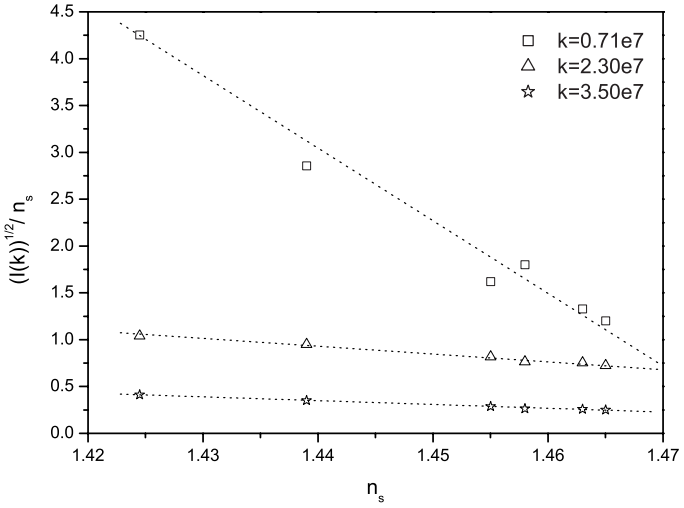

FIGURE 7.7. Examples of $\frac{1}{n_s}\sqrt{I}$ as a function of the solvent refractive index plotted for three different k-values. $I(k)$ has been obtained from the measurements of SiCoF at $\lambda = 435.8$ nm in Figure 7.5.

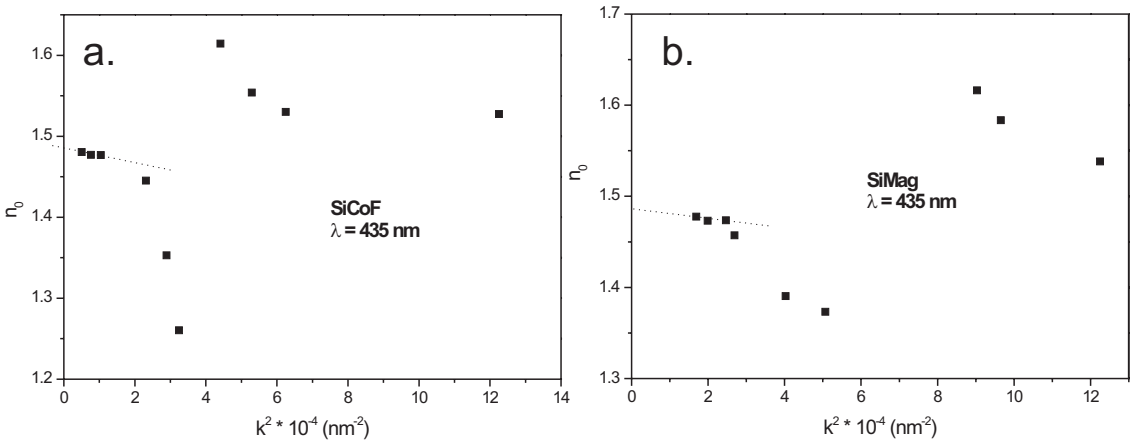

FIGURE 7.8. Plot of n_0-values as a function of k^2 for SiCoF (left) and SiMag (right). The dotted line indicates the initial slope at small k, from which the average particle refractive index, n_p is determined by extrapolation to $k = 0$. From these plots it was found that for SiCoF $n_p = 1.49$ and for SiMag $n_p = 1.48$.

by silica reduces the absorption by the embedded cobalt ferrite particles. The same trend can be noted in the SLS measurements. Close to the matching point of silica, the intensity minima become shallower. The absorption maximum, however, occurs at shorter wavelengths than at which the angle-dependent light scattering measurements were performed.

Mie-scattering theory takes absorption into account via the imaginary part of the complex refractive index, $n = n' - in''$. Contributions of light absorption then cause a fill-up of the intensity minima, which indeed is observed to some extent in the measured scattering curves (see Figures 7.5 and 7.6). This is one indication that RGD-theory does

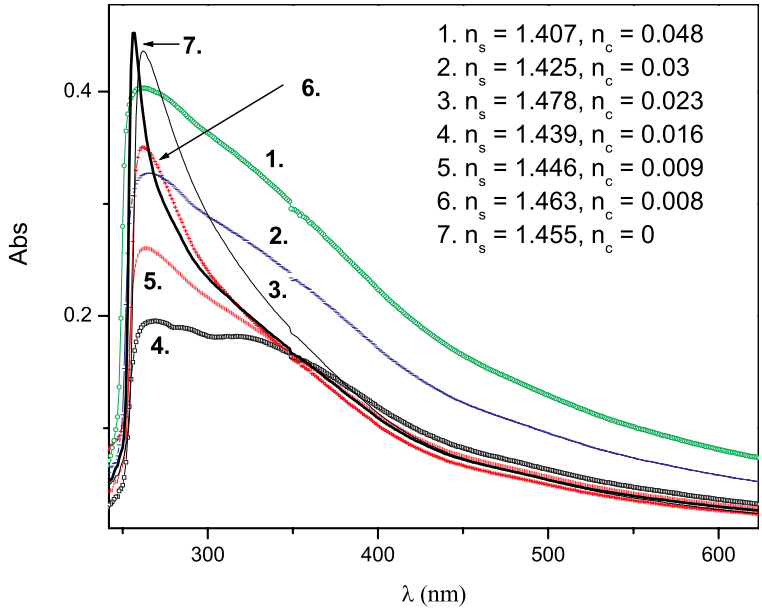

Figure 7.9. UV-vis spectra of silica-cobalt ferrite composite particles at various optical contrasts. Here n_c indicates the optical contrast with respect to the silica in the particles.

not capture all details of the angular scattering profile, even though features such as the location of the iso-scattering points agree reasonably well with with the RGD prediction. The particle radii obtained from the contrast variation experiments measurements are somewhat larger than expected from analysis of TEM pictures.

Core-radius from angular intensity profile at the matching point of silica

We also investigated the possibility of obtaining the core radius of the SiCoF particles from the scattering curve measured at $n_s = 1.455$, i.e. the refractive index that matches the silica core and outer shell, such that only scattered intensity from the iron oxide sphere remains (see Figure 7.10). According to Eqs 7.17 and 7.18, the radius of the core can be obtained from the intensity minima when $n_1 = n_3 = n_s$ using $R_1 = \pi/k$ for the first minimum, $R_1 = 2\pi/k$ for the second minimum etc. For SiCoF, the first minimum at $k = 1.31 \times 10^7$ corresponds to $R_1 = 240$ nm and the second minimum at $k = 3.30 \times 10^7$ to $R_1 = 190$ nm. The core radius determined from TEM on the bare silica core was only 158 nm. The three values of R_1 are quite different and it must be concluded that the ferrite shell thickness probably is too large compared to the core radius to assume an infinitely thin shell. Moreover the influence of absorption appearently obstructs obtaining R_1 using RGD-theory.

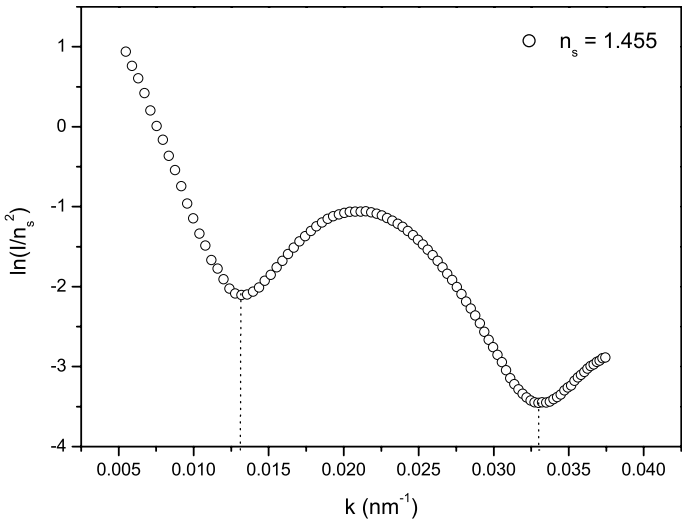

Figure 7.10. Scattering intensity profile mainly due to an iron oxide layer only measured near to the optical matching point of silica ($n_s = 1.455$).

7.5. Conclusions

Static light scattering measurements were performed on colloidal silica particles with two concentric shells, the inner one containing metal oxide nanoparticles. Upon changing the optical contrast by varying the solvent refractive index, a shift is observed of the intensity minima in the scattering curves. In accordance with light scattering theory within the RGD approximation, the scattering curves measured at various optical contrasts intersect at an iso-scattering point. The radius calculated from this intersection point is only slightly larger than the radius obtained from analysis of TEM images. The square root of the scattered intensity at a given wave vector was found to vary linearly with the solvent refractive index as expected from contrast variation in the RGD approximation. Nevertheless, RGD theory does not capture all details of the angular scattering profiles. The light absorption by the metal oxide particles, for example, increases as the surrounding silica is nearly matched, resulting in more shallow intensity minima. A quantitative analysis of such features requires Mie-scattering theory for spheres with an embedded light-absorbing shell. In case this shell is comparable to the iron oxide shell in our silica spheres, the results in this Chapter show that size and average refractive index of such colloids can be determined fairly well from light scattering within the RGD approximation. Empirically, it can be concluded that for colloidal particles containing a relatively thin shell of light absorbing nanoparticles, optical contrast variation measurements can be applied to obtain information about the size and the average refractive index of the particles.

Acknowledgements

We thank Emile Bakelaar and Karel Planken for assistance with the UV-vis spectra. Prof. dr. Kees de Kruif has contributed with helpful discussions. Dr. Arnout Imhof and Job Thijssen at the Soft Condensed Matter group, Utrecht, are acknowledged for valuable inputs on Mie-theory and scattering from dumbbell-shaped colloidal particles.

Bibliography

[1] A. Vrij, E. A. Nieuwenhuis, H. M. Fijnaut, and W. G. M. Agterof. Application of modern concepts in liquid state theory to concentrated particle dispersions. *Faraday Discuss. Chem. Soc.*, 65:101, 1978.

[2] W. Poon. Colloids as big atoms. *Science*, 304:830, 2004.

[3] T. Sugimoto, editor. *Fine particles : Synthesis, characterization, and mechanisms of growth*, volume 92 of *Surfactant science series*. Dekker, New York, 2000.

[4] A. P. Philipse. Particulate colloids: Aspects of preparation and characterization. In J. Lycklema, editor, *Fundamentals of interface and colloid science*, volume IV. Academic Press, London, 2005.

[5] C. Burda, X. Chen, R. Narayanan, and M.A. El-Sayed. Chemistry and properties of nanocrystals of different shapes. *Chem. Rev.*, 105:1025, 2005.

[6] D. H. Everett. *Basic principles of colloidal science*. The Royal Society of Chemistry, Cambridge, 1988.

[7] D. F. Evans and H. Wennerström. *The colloidal domain*. Wiley-VCH, New York, 1999.

[8] K. Butter, P. H. Bomans, P. M. Frederik, G. J. Vroege, and A. P. Philipse. Direct observation of dipolar chains in iron ferrofluids by cryogenic electron microscopy. *Nat. Mater.*, 2:88, 2003.

[9] M. Klokkenburg, C. Vonk, E. M. Claesson, J. D. Meeldijk, B. H. Erné, and A. P. Philipse. Direct imaging of zero-field dipolar structures in colloidal dispersions of synthetic magnetite. *J. Am. Chem. Soc.*, 126:16706, 2004.

[10] B. Berkovski and V. Bashtovoy, editors. *Magnetic fluids and applications handbook*. Begell House Inc., New York, 1996.

[11] S. S. Papell. U.S. patent no 3 215 572, 1965.

[12] R.E. Rosensweig. Magnetic fluids. *Scientific American*, 247:136, 1982.

[13] S. Sun and C.B. Murray. Synthesis of monodisperse cobalt nanocrystals and their assembly into magnetic superlattices. *J. Appl. Phys.*, 85:4325, 1999.

[14] K. Butter, A. P. Philipse, and G. J. Vroege. Synthesis and properties of iron ferrofluids. *J. Magn. Magn. Mater.*, 252:1, 2002.

[15] V. F. Puntes, K. M. Krishnan, and P. Alivisatos. Colloidal nanocrystal shape and size control: The case of cobalt. *Science*, 291:2115, 2001.

[16] Shouheng Sun, C. B. Murray, Dieter Weller, Liesl Folks, and Andreas Moser. Monodisperse FePt nanoparticles and ferromagnetic FePt nanocrystal superlattices. *Science*, 287:1989, 2000.

[17] T. Hyeon. Chemical synthesis of magnetic nanoparticles. *Chem. Commun.*, 34:927, 2003.

[18] T. Hyeon, S.S. Lee, J. Park, Y. Chung, and H.B. Na. Synthesis of highly crystalline and monodisperse maghemite nanocrystallites without a size-selection process. *J. Am. Chem. Soc.*, 123:12798, 2001.

[19] S. Sun and H. Zeng. Size-controlled synthesis of magnetite nanoparticles. *J. Am. Chem. Soc.*, 124:8204, 2002.

[20] A. P. Philipse, M.P.B van Bruggen, and C. Pathmamanoharan. Magnetic silica dispersions: Preparation and stability of surface modified silica particles with a magnetic core. *Langmuir*, 10:92, 1994.

[21] L. N. Donselaar. *Silica-magnetite colloids and magnetic fluids*. PhD-thesis, Utrecht University, 1998.

[22] G. A. van Ewijk, G.J. Vroege, B.W.M. Kuipers, and A.P. Philipse. Thermodynamic (in)stability of ferrofluid-polymer mixtures. *J. Magn. Magn. Mater.*, 252:32, 2002.

[23] G. van Ewijk. *Phase behaviour of mixtures of magnetic colloids and non-adsorbing polymer*. PhD-thesis, Utrecht University, The Netherlands, 2001.

[24] C. Pathmamanoharan and A. P. Philipse. Preparation and properties of monodisperse magnetic cobalt colloids grafted with polyisobutene. *J. Colloid and Interface Sci*, 205:340353, 1998.

[25] C. Pathmamanoharan. *Preparation and characterization of model colloids*. PhD-thesis, Utrecht University, The Netherlands, 1998.

[26] K. Butter. *Iron(oxide) ferrofluids: Synthesis, structure and catalysis*. PhD-thesis, Utrecht University, The Netherlands, 2003.

[27] M. Klokkenburg, R. P. A. Dullens, W. K. Kegel, B. H. Erné, and A. P. Philipse. Quantitative real-space analysis of self-assembled structures of magnetic dipolar colloids. *Phys. Rev. Lett.*, 96:0372031, 2006.

[28] Q. A. Pankhurst, J. Connolly, S. K. Jones, and J. Dobson. Applications of magnetic nanoparticles in biomedicine. *J. Phys. D: Appl. Phys.*, 36:R167, 2003.

[29] U. O. Hafeli. Magnetically modulated therapeutic systems. *International Journal of Pharmaceutics*, 277:19, 2004.

[30] A. S. Lubbe, C. Alexiou, and C. Bergemann. Clinical applications of magnetic drug targeting. *Journal of Surgical Research*, 95:200, 2001.

[31] M. Everaars. Océ's mono component, magnetic, conductive colour toner. *IS & T's NIP:21 International conference on digital printing technologies*, 21:637, 2005.

[32] I. E. M. Severens. *DEM simulations of toner behavior in the development nip of the Océ direct imaging process*. PhD-thesis, Technische Universiteit Eindhoven, The Netherlands, 2005.

[33] N. T. S. Phan, C. S. Gill, J. V. Nguyen, Z. J. Zhang, and C. W. Jones. Expanding the utility of one-pot multistep reaction networks through compartmentation and recovery of the catalyst. *Angew. Chem. Int. Ed.*, 45:2209, 2006.

[34] R. Langer. Drugs on target. *Science*, 293:58, 2001.

[35] A. J. Rosengart, M. D. Kaminski, H. Chen, P. L. Caviness, A. D. Ebner, and J. A. Ritter. Magnetizable implants and functionalized magnetic carriers: A novel approach for noninvasive yet targeted drug delivery. In *Journal of Magnetism and Magnetic Materials Proceedings of the Fifth International Conference on Scientific and Clinical Apllications of Magnetic Carriers*, 293:633, 2005.

[36] C. Alexiou, R.J. Schmid, R. Jourgons, M. Kremer, G. Wanner, C. Bergemann, E. Huenges, T. Nawroth, W. Arnold, and F. G. Parak. Targeting cancer cells: Magnetic nanoparticles as drug carriers. *Eur Biophys J*, 35:446, 2006.

[37] A. S. Lubbe, C. Bergemann, H. Riess, F. Schriever, P. Reichardt, K. Possinger, M. Matthias, B. Dorken, F. Herrmann, R. Gurtler, P. Hohenberger, N. Haas, R. Sohr, B. Sander, A.-J. Lemke, D. Ohlendorf, W. Huhnt, and D. Huhn. Clinical experiences with magnetic drug targeting: A phase I study with 4'-epidoxorubicin in 14 patients with advanced solid tumors. *Cancer Res*, 56:4686, 1996.

[38] R. E. Rosensweig. Heating magnetic fluid with alternating magnetic fields. *J. Magn. Magn. Mater.*, 252:370, 2002.

[39] S. Mornet, S. Vasseur, F. Grasset, P. Veverka, G. Goglio, A. Demourgues, J. Portier, E. Pollert, and E. Duguet. Magnetic nanoparticle design for medical applications. *Prog. Solid State Chem.*, 34:237, 2006.

[40] A. Ito, M. Shinkai, H. Honda, and T. Kobayashi. Medical application of functionalized magnetic nanoparticles. *Journal of Bioscience and Bioengineering*, 100:1, 2005.

[41] A. M. Schmidt. Induction heating of novel thermoresponsive ferrofluids. *J. Magn. Magn. Mater.*, 289:5, 2005.

[42] R. Massart. Preparation of aqueous magnetic liquids in alkaline and acidic media. *IEEE Trans. Magn.*, MAG-17:1247, 1981.

[43] A. Bee, R. Massart, and S. Neveu. Synthesis of very fine maghemite particles. *J. Magn. Magn. Mater.*, 149:6, 1995.

[44] R. Massart, E. Dubois, V. Cabuil, and E. Hasmonay. Preparation and properties of monodisperse magnetic fluids. *J. Magn. Magn. Mater.*, 149:1, 1995.

[45] F. A. Tourinho, R. Franck, and R. Massart. Aqueous ferrofluids based on manganese and cobalt ferrites. *J. Mater. Sci.*, 25:3249, 1990.

[46] E. M. Claesson and A.P. Philipse. Monodisperse magnetizable composite silica spheres with tunable dipolar interactions. *Langmuir*, 21:9412, 2005.

[47] A. van Blaaderen and A. Vrij. Synthesis and characterization of colloidal dispersions of fluorescent, monodisperse silica spheres. *Langmuir*, 8:2921, 1992.

[48] A.P. Philipse and A. Vrij. Preparation and properties of nonaqueous model dispersions of chemically modified, charged silica spheres. *J. Colloid Interface Sci.*, 128:121, 1989.

[49] P. Radstake. *Synthesis and characterization of magnetic cobalt nanoparticles.* Bachelor thesis, Utrecht University, 2004.

[50] W. Stöber, A. Fink, and E. Bohn. Controlled growth of monodisperse silica spheres in the micron size range. *J. Colloid Interface Sci.*, 26:62, 1968.

[51] V. Cabuil, R. Massart, J-C Bacri, R. Perzynski, and D. Salin. Ionic ferrofluids: Towards fractional distillation. *J. Chem. Res.*, page 130, 1987.

[52] S. Lefebure, E. Dubois, V. Cabuil, S. Neveu, and R. Massart. Monodisperse magnetic nanoparticles: Preparation and dispersion in water and oils. *J. Mater. Res.*, 13:2975, 1998.

[53] A. K. van Helden, J.W. Jansen, and A. Vrij. Preparation and characterization of spherical monodisperse silica dispersions in non-aqueous solvents. *J. Colloid Interface Sci.*, 81:354, 1981.

[54] G. H. Bogush, M. A. Tracy, and C. F. Zukoski IV. Preparation of monodisperse silica particles: Control of size and mass fraction. *J. Non-Cryst. Solids*, 104:95, 1988.

[55] Y. Zhu, H. Da, X. Yang, and Y. Hu. Preparation and characterization of core-shell monodispersed magnetic silica microspheres. *Colloids Surf., A*, 231:123, 2003.

[56] F. Caruso. Nanoengineering of particle surfaces. *Adv. Mater.*, 13:11, 2001.

[57] C.D. Bain, E.B. Troughton, Y-T. Tao, J. Evall, G.M. Whitesides, and R.G. Nuzzo. Formation of monolayer films by the spontaneous assembly of organic thiols from solution onto gold. *J. Am. Ceram. Soc.*, 111:321, 1989.

[58] N. Fauconnier, J. N. Pons, J. Roger, and A. Bee. Thiolation of maghemite nanoparticles by dimercaptosuccinic acid. *J. Colloid Interface Sci.*, 194:427, 1997.

[59] N. Hebalkar, S. Kharrazi, A. Ethiraj, J. Urban, R. Flink, and S. K.Kulkarni. Structural and optical investigations of SiO_2-CdS core-shell particles. *J. Colloid Interface Sci.*, 278:107, 2004.

[60] A. R. Cestari and C. Airoldi. Chemisorption on thiolsilicas: Divalent cations as a function of pH and primary amines on thiolmercury adsorbed. *J. Colloid Interface Sci.*, 195:338, 1997.

[61] L. N. H. Arakaki, V. L. S. Augusto Filha, J. G. P Espinola, M. G. da Fonseca, S. F. de Oliveira, T. Arakaki, and C. Airoldi. New thiol adsorbent grafted on silica gel: Synthesis, characterization and employment for heavy metal adsorptions. *J. Environ. Monit.*, 5:366, 2003.

[62] A.P. Philipse and D. Maas. Magnetic colloids from magnetotactic bacteria: Chain formation and colloidal stability. *Langmuir*, 18:9977, 2002.

[63] J. Wagner, T. Autenrieth, and R. Hempelmann. Core shell particles consisting of cobalt ferrite and silica as model ferrofluids [$CoFe_2O_4$ - SiO_2 core shell particles]. *J. Magn. Magn. Mater.*, 252:4, 2002.

[64] J. Smids and G. van Ewijk. *Unpublished results*, Van 't Hoff Laboratory, Utrecht, 2002.

[65] E. P. Plueddemann. *Silane coupling agents*. Plenum Press, New York, 1982.

[66] H. Giesche. Synthesis of monodispersed silica powders I. particle properties and reaction kinetics. *J. Eur. Ceram. Soc.*, 14:189, 1994.

[67] H. Giesche. Synthesis of monodispersed silica powders II. controlled growth reactions and continous production processes. *J. Eur. Ceram. Soc.*, 14:205, 1994.

[68] A. P. Philipse. Preparation of boehmite-silica colloids: Rods, spheres, needles and gels. *Colloids and Surfaces A: Physicochemical and Engineering Aspects*, 80:203, 1993.

[69] A. Imhof, M. Megens, J.J. Engelberts, D.T.N. de Lang, R.Sprik, and W. L. Vos. Spectroscopy of fluorescein (FITC) dyed colloidal silica spheres. *J. Phys. Chem. B*, 103:1408, 1999.

[70] A. van Blaaderen and A. Vrij. Synthesis and characterization of monodisperse colloidal organosilica spheres. *J. Colloid Interface Sci.*, 156:1, 1993.

[71] A. P. Philipse, C. Smits, and A. Vrij. A light scattering constrast variation study on nonaqueous suspensions of coated silica spheres. *J. Colloid Interface Sci.*, 129:335, 1989.

[72] L. Chu, M. W. Daniels, and L. F. Francis. Use of (glycidoxypropyl)trimethoxysilane as a binder in colloidal silica coatings. *Chem. Mater.*, 9:2577, 1997.

[73] M. Zayat and D. Levy. Surface organic modifications and the performance of sol-gel derived gel-glass dispersed liquid crystals (gdlcs). *Chem. Mater.*, 15:2122, 2003.

[74] C. Yang, H. Sheu, and K. Chao. Templated synthesis and structural study of densely packed metal nanostructures in mcm-41 and mcm-48. *Adv. Funct. Mater.*, 12:143, 2002.

[75] C. Graf and A. van Blaaderen. Metallodielectric colloidal core-shell particles for photonic applications. *Langmuir*, 18:524, 2002.

[76] A. Taguchi and F. Schüth. Ordered mesoporous materials in catalysis. *Microporous Mesoporous Mater.*, 77:1, 2005.

[77] S. G. J. M. Kluijtmans, J. K. G. Dhont and A. P. Philipse. A light scattering contrast variation of bicontinuous porous glass media. *Langmuir*, 13:4976, 1997.

[78] B. J. Rappoli and D. A. Rowley. The sorption kinetics of copper(II) on chemically modified controlled pore glass. *J. Colloid Interface Sci.*, 226:218, 2000.

[79] M.P.B van Bruggen. Preparation and properties of colloidal core-shell rods with adjustable aspect ratios. *Langmuir*, 14:2245, 1998.

[80] C. Graf, D. L. J. Vossen, A. Imhof, and A. van Blaaderen. A general method to coat colloidal particles with silica. *Langmuir*, 19:6693, 2003.

[81] M. Giersig and P. Mulvaney. Preparation of ordered colloid monolayers by electrophoretic deposition. *Langmuir*, 9:3408, 1993.

[82] M. S. Fleming and D. R. Walt. Stability and exchange studies of alkanethiol monolayers on gold-nanoparticle-coated silica microspheres. *Langmuir*, 17:4836, 2001.

[83] M. L. Anderson, C. A. Morris, R. M. Stroud, C. I. Merzbacher, and D. R. Rolison. Colloidal gold aerogels: Properties, and characterization. *Langmuir*, 15:674, 1999.

[84] A. M. Urmenyi, A. P. Philipse, R. G.H. Lammertink, and M. Wessling. Polymer-in-a-crust membranes: Macroporous materials with tunable surface functionality. *Langmuir*, 22:5459, 2006.

[85] C. Pathmamanoharan and A.P. Philipse. Preparation of small alkane-grafted silica particles (for SAXS and SANS studies) from aqueous commersial sols. *J. Colloid Interface Sci.*, 165:519, 1994.

[86] L. M. Liz-Marzán and A. P. Philipse. Synthesis and optical properties of gold-labeled silica particles. *J. Colloid Interface Sci.*, 176:459, 1995.

[87] L. M. Liz-Marzán, M. Giersig, and P. Mulvaney. Synthesis of nanosized gold-silica core-shell particles. *Langmuir*, 12:4329, 1996.

[88] P. T. Anastas and J. C. Warner. *Green chemistry: Theory and practice*. Oxford University Press, New York, 1998.

[89] F. R. Hartley. *Supported metal complexes*. Kluwer Academic, Dordrecht, 1985.

[90] J. M. Thomas and R. Raja. Catalytic significance of immobilized organometallic compounds: Economically and environmentally important examples. *J. Organomet. Chem.*, 689:4110, 2004.

[91] P. McMorn and G. J. Hutchings. Heterogeneous enantioselective catalysts: Strategies for the immobilisation of homogeneous catalysts. *Chem. Soc. Rev.*, 33:108, 2004.

[92] D. Brunel, N. Bellocq, P. Sutra, A. Cauvel, M. Laspras, P. Moreau, F. Di Renzo, G. Anne, and F. Franois. Transition-metal ligands bound onto micelle-templated silica surface. *Coord. Chem. Rev.*, 178-180:1085, 1998.

[93] J. H. Clark and D. J. Macquarrie. Catalysis of liquid phase organic reactions using chemically modified mesoporous inorganic solids. *Chem. Commun.*, 8:853, 1998.

[94] S-W. Kim, M. Kim, W. Y. Lee, and T. Hyeon. Fabrication of hollow palladium spheres and their successful application to the recycable heterogeneous catalyst for suzuki coupling reactions. *J. Am. Chem. Soc.*, 124:7642, 2002.

[95] D. K. Yi, S. S. Lee, and J. Y. Ying. Synthesis and applications of magnetic nanocomposite catalysts. *Chem. Mater.*, 18:2459, 2006.

[96] A-H. Lu, W-C. Li, A. Kiefer, W. Schmidt, E. Bill, G. Fink, and F. Schüth. Fabrication of magnetically separable mesostructured silica with an open pore system. *J. Am. Chem. Soc.*, 126:8616, 2004.

[97] M. E. van der Boom and D. Milstein. Cyclometalated phosphine-based pincer complexes: Mechanistic insight in catalysis, coordination, and bond activation. *Chem. Rev.*, 103:1759, 2003.

[98] M. Albrecht and G. van Koten. Platinum group organometallics based on pincer ligands: Sensors, switches, and catalysts. *Angew. Chem. Int. Ed.*, 40:3750, 2001.

[99] J. M. Longmire, X. Zhang, and M. Shang. Synthesis and x-ray crystal structures of palladium(II) and platinum(II) complexes of the pcp-type chiral tridentate ligand (1r,1'r)-1,3-bis[1-(diphenylphosphino)ethyl]benzene. *Organometallics*, 17:4374, 1998.

[100] N. C. Mehendale, R. J. M. Klein Gebbink, and G. van Koten. *manuscript in preparation*.

[101] R. Piazza and V. Degiorgio. Single-particle dynamics in a colloidal crystal. *Phys. Rev. Lett.*, 67:3868, 1991.

[102] G. H. Koenderink, M. P. Lettinga, and A. P. Philipse. Rotational dynamics of charged colloidal spheres: Role of particle interactions. *J. Chem. Phys.*, 117:7751, 2002.

[103] M. P. Lettinga, G. H. Koenderink, B. W. M. Kuipers, E. Bessels, and A. P. Philipse. Rotational dynamics of colloidal spheres probed with fluorescence recovery after photobleaching. *J. Chem. Phys.*, 120:4517, 2004.

[104] B. H. Erné, E. M. Claesson, S. Sacanna, M. Klokkenburg, I. A. Bakelaar, and B. W. M. Kuipers. Low-frequency complex magnetic susceptibility of magnetic composite microspheres in colloidal dispersion. *J. Magn. Magn. Mater.*, 311:145–149, 2007.

[105] D.R Lide, editor. *Handbook of chemistry and physics*. CRC press, Boca Raton, 81 edition, 2000.

[106] B. H. Erné, K. Butter, B. W. M. Kuipers, and G. J. Vroege. Rotational diffusion in iron ferrofluids. *Langmuir*, 19:8218, 2003.

[107] P.C. Fannin. Wideband measurement and analysis techniques for the determination of the frequency-dependent, complex susceptibility of magnetic fluids. *Adv. Chem. Phys.*, 104:181, 1998.

[108] B. W. M. Kuipers, I. A. Bakelaar, M. Klokkenburg, and B. H. Erné. *manuscript in preparation*.

[109] B. H. Erné, E van der Pol, G. J. Vroege, T. Visser, and H. H. Wensink. Size-fractionation in a phase-separated colloidal fluid. *Langmuir*, 21:1802, 2005.

[110] V. Degiorgio, R. Piazza, and R. B. Jones. Rotational diffusion in concentrated colloidal dispersions of hard spheres. *Phys. Rev. E*, 52:2707, 1995.

[111] M. Watzlawek and G. Nägele. Diffusion of colloids at short times. *Prog. Colloid Polym. Sci.*, 104:168, 1997.

[112] M. H. J. Hagen, D. Frenkel, and C. P. Lowe. Rotational diffusion in dense suspensions. *Phys. A*, 272:376, 1999.

[113] P. C. Fannin, L. Cohen-Tannoudji, E. Bertrand, A. T. Giannitsis, C. Mac Oireachtaigh, and J. Bibette. Investigation of the complex susceptibility of magnetic beads containing maghemite nanoparticles. *J. Magn. Magn. Mater.*, 303:147, 2006.

[114] P. C. Fannin, S. W. Charles, C. M. Oireachtaigh, and S. Odenbach. Investigation of possible hysteresis effects araising from frequency- and field-dependent complex magnetic susceptibility. *J. Magn. Magn. Mater.*, 302:1, 2006.

[115] B. U. Felderhof and R. B. Jones. Nonlinear response of a dipolar system with rotational diffusion to an oscillating field. *J. Phys.: Condens. Matter*, 15:S1363, 2003.

[116] C. Caizer. The effect of the external magnetic field on the thermal relaxation of magnetization in systems of aligned nanoparticles. *J. Phys.: Condens. Matter*, 17:2019, 2005.

[117] A. P. Astalan, F. Ahrentorp, C. Johansson, K. Larsson, and A. Krozer. Biomolecular reactions studied using changes in brownian rotation dynamics of magnetic particles. *Biosens. Bioelectron.*, 19:945, 2004.

[118] M. Kerker. *Scattering of light and other electromagnetic radiation*. Academic Press, New York, 1969.

[119] R. Piazza, V. Degiorgio, M. Corti, and J. Stavans. Rotational and translational self-diffusion of interacting spherical brownian particles. *Phys. Rev. B*, 42:4885, 1990.

[120] M. P. Lettinga, C. M. van Kats, and A. P. Philipse. Rotational diffusion of tracer spheres in packings and dispersions of colloidal spheres studied with time-resolved phosphorescence anisotropy. *Langmuir*, 16:6166, 2000.

[121] M. P. Lettinga, M. A. M. J. van Zandvoort, C. M. van Kats, and A. P. Philipse. Phosphorescent colloidal silica spheres as tracers for rotational diffusion studies. *Langmuir*, 16:6156, 2000.

[122] A. Sashchiuk, L. Amirav, M. Bashouti, M. Krueger, U. Sivan, and E. Lifshitz. PbSe nanocrystal assemblies: Synthesis and structural, optical, and electrical characterization. *Nano Lett.*, 4, 2004.

[123] H. Zhang and G. Nägele. Tracer-diffusion in binary colloidal hard-sphere. *J. Chem. Phys.*, 117:5908, 2002.

[124] E. M. Claesson, B. H. Erné, E. Bakelaar, and B. M. W. Kuipers. Measurement of the particle magnetic dipole moment of magnetizable composite silica spheres. *J. Phys.: Condens. Matter*, 19:036105, 2007.

[125] B. Cichocki, M. L. Ekiel-Jezewska, and E. Wajnryb. Lubrication corrections for three-particle contribution to short-time self-diffusion in colloidal dispersions. *J. Chem. Phys.*, 111:3265, 1999.

[126] P. W. Atkins. *Physical chemistry*. Oxford University Press, Oxford, 6 edition, 1998.

[127] D-X. Chen, J. A. Brug, and R. B. Goldfarb. Demagnetizing factors for cylinders. *IEEE Trans. Magn.*, 27:3601, 1991.

[128] M. Klokkenburg, B. H. Erné, J. D. Meeldijk, A. Wiedenmann, A. V. Petukhov, R. P.A . Dullens, and A. P. Philipse. In situ imaging of field-induced hexagonal columns in magnetite ferrofluids. *Phys. Rev. Lett.*, 97:185702, 2006.

[129] H. E. Bergna, editor. *The colloid chemistry of silica*, volume 234 of *Advances in chemistry series*. American Chemical Society, Washington, DC, 1994.

[130] G. Bryant, T. Mortensen, S. Henderson, S. Williams, and W. van Megen. Optical contrast variation study of nonaqueous suspensions of polymer particles. *J. Colloid and Interface Sci*, 216:401, 1999.

[131] G. Mie. Beiträge zur Optik trüber Medien, speziell kolloidaler Metallösungen. *Ann. Phys.*, 25:337, 1908.

[132] A. L. Aden and M. Kerker. Scattering of electromagnetic waves from two concentric spheres. *J. Appl. Phys.*, 22, 1951.

[133] J. W. Jansen, C. G. de Kruif, and A. Vrij. Attractions in sterically stabilized silica dispersions III. *J. Colloid Interface Sci.*, 114, 1986.

[134] A. J. Banchio, G. Nägele, and A. Ferrante. Optical polydispersity and contrast variation effects in colloidal dispersions. *J. Colloid and Interface Sci*, 208:487, 1998.

[135] I. Livsey and R.H. Ottewill. Light scattering by concentric sphere particles. *Adv. Colloid Interface Sci*, 36:173, 1991.

[136] R. Pecora and S. R. Aragón. Theory of light scattering from hollow spheres. *Chem. Phys. Lipids*, 13:1, 1973.

[137] P. M. Johnson, C. M. van Kats, and A. van Blaaderen. Synthesis of colloidal silica dumbbells. *Langmuir*, 21:11510, 2005.

Summary

This thesis deals with the preparation and properties of magnetic silica core-shell colloids and related functionalized silica structures. The core-shell particles are composed of functionalized amorphous silica spheres decorated with a layer of irreversibly bound magnetic nanoparticles, in some cases supplied with an additional silica coating. Developing and optimising synthesis procedures for well-defined core-shell colloids in a stable suspension form an important part of this thesis. Moreover, physical properties of these colloids are investigated, such as the magnetic dipole moment, dipolar structure formation and rotational dynamics of the magnetic silica spheres. Core-shell colloids with a controlled composition, size and morphology are essential for such investigations. In addition to the study of preparation methods and physical properties, attention is paid to applications, such as functionalization of commercial silica sols and membranes as well as functionalization of magnetic silica with a catalyst.

In Chapter 2, the chemical synthesis is described of silica particles that contain a shell of magnetic nanoparticles at an adjustable distance below the sphere surface. Colloidal monodisperse silica spheres are coated with a thiol-containing silane coupling agent, allowing magnetic nanoparticles of either maghemite or cobalt ferrite from aqueous ferrofluids to be irreversibly attached to the surface of the silica core. These core-shell particles are covered with an outer silica shell which can be modified to stabilize the particles in a variety of solvents. The same type of particles were also prepared with fluorescent silica cores to enable observation with confocal scanning laser microscopy. Both electron and confocal scanning laser microscopy show that these magnetizable silica colloids form dipolar chains when exposed to a homogeneous magnetic field, depending on the thickness of the outer silica shell.

The method to synthesize silica composites via thiol-functionalization is extended in Chapter 3 to other types of silica sols, such as commercially available silica nanoparticles, and porous silica grains to form composites with gold nanoparticles. Additionally, membranes of polyethersulfone were functionalised after first having been encapsulated in a crust of silica nanoparticles.

The possibility to manipulate magnetic colloids with an external magnetic field makes them interesting for many technical applications. An illustrative example is given in Chapter 4, where a proof-of-principle experiment is presented in which magnetic silica particles are coated with a catalyst. Without applied magnetic field, the catalytic particles remain dispersed in the reaction mixture, which is crucial for effective catalysis.

The particles, and by that the catalyst, can easily be separated from the solution with a small magnet due to their large induced dipole moment. Silica colloids with embedded maghemite nanoparticles are used, since their induced dipole moment is lost upon removing the magnet and the particles can be redispersed to use the catalyst again.

The magnetic properties of the magnetic silica spheres are investigated in Chapter 5 by measuring magnetization curves and the complex magnetic susceptibility as a function of both frequency and field amplitude. In this chapter it is demonstrated that silica microparticles with embedded cobalt ferrite nanoparticles have a permanent magnetic moment. This is revealed by susceptibility spectra of magnetic silica particles dispersed in ethanol, which show a characteristic frequency that corresponds to Brownian rotation of the microparticles, whereas the spectra of silica particles with maghemite only show contributions from Néel relaxation inside the nanoparticles. It is argued that the microspheres with cobalt ferrite should have a permanent magnetic dipole moment even when the nanoparticles are oriented at random. This is expected since the vector sum of randomly oriented unit vectors is non-zero. The permanent magnetic moment was increased after treatment in a strong, saturating magnetic field, because once the field is removed, a large fraction of the dipoles does not relax to random orientations, but to the nearest preferred crystallographic axes. Being able to quantify the dipole moment of the composite particles enables estimation of the maximum interaction energy between the particles, which for the particles studied here is on the order of 0.5 to 1 k_BT.

In Chapter 6, frequency-dependent complex magnetic susceptibility spectra were measured of dispersions of silica spheres with embedded cobalt ferrite as a function of the concentration. In this way, the nearly diffusive rotation of dipolar particles is investigated in a weak alternating field. Compared to optical techniques used to measure rotational diffusion, this technique is not hindered by multiple scattering or light absorption, giving the opportunity to study the particle rotation of attractive spheres.

Finally, in Chapter 7 the results from static light scattering of the magnetic silica particles at various optical contrasts are shown. We investigated to what extent the theory for static light scattering of optically inhomogeneous particles in the Rayleigh-Gans-Debye approximation can be applied to spherical composite particles containing a core and two concentric shells, of which one containing magnetic metal oxide nanoparticles with a high refractive index. Although not able to describe the entire scattering profiles, we find iso-scattering points corresponding to the radius of single particles as obtained from electron microscopy.

Samenvatting

Dit proefschrift beschrijft de synthese en eigenschappen van colloïdale magnetische silica kern-schil deeltjes en verwante silicastructuren. De kern-schil deeltjes bestaan uit silicabollen voorzien van een laagje magnetische nanodeeltjes, irreversibel gebonden via thiolgroepen, en een buitenste silicalaag. Een belangrijk deel van het proefschrift vormt het ontwerpen en optimaliseren van methoden voor de chemische synthese van nauwkeurig gedefinieerde kern-schil colloïden in stabiele suspensies. Bovendien zijn de fysische eigenschappen van de magnetische silicadeeltjes onderzocht, bijvoorbeeld het magnetische dipoolmoment, dipolaire structuurvorming en Brownse rotatiedynamiek. Kern-schil colloïden met een gecontroleerde chemische samenstelling, afmeting en morfologie zijn interessant voor fundamenteel colloïdchemisch onderzoek. Daarnaast wordt in dit proefschrift ook aandacht besteed aan toepassingen zoals het functionaliseren van commercieel verkrijgbare silicasolen of silicamembranen met geadsorbeerde nanodeeltjes en het functionaliseren van magnetische silicacolloïden met geadsorbeerde katalysatorverbindingen.

In hoofdstuk 2 wordt de chemische synthese beschreven van silicadeeltjes met ingesloten magnetische nanodeeltjes. Deze bevinden zich op een variabele afstand van het centrum van de silicabol. Het oppervlak van colloïdale, monodisperse silicabollen is gemodificeerd met een silaanverbinding welke voorzien is van een thiolgroep. Daarmee zijn magnetische nanodeeltjes van bijvoorbeeld cobaltferriet en maghemiet irreversibel vast te zetten op de silicabollen. De verkregen kern-schil deeltjes kunnen vervolgens voorzien worden van een uitwendige silicaschil waarvan het oppervalk zodanig kan worden gemodificeerd dat de deeltjes stabiel te dispergeren zijn in verschillende oplosmiddelen. In het midden van de silicabol kunnen ook fluorescerende kleurstoffen worden ingebouwd waardoor de bollen zichtbaar kunnen worden gemaakt met confocale optische microscopie. Zowel confocale microscopie als elektronenmicroscopie tonen aan dat deze magnetiseerbare silicadeeltjes, afhankelijk van de dikte van de buitenste silicaschil, dipolaire structuren vormen in een homogeen magneetveld.

De methode om nanodeeltjes vast te zetten op silica via thiolverbindingsgroepen wordt in hoofdstuk 3 uitgebreid naar commercieel verkrijgbare silica nanodeeltjes en poreuze silicakorrels. Om het succes van deze aanpak aan te tonen worden gouden nanodeeltjes op de silica vastgezet. De aanpak werkt ook met membranen van polyethersulfon die eerst voorzien zijn van een silicakorstje.

De mogelijkheid om magnetische colloïden te manipuleren met externe magneetvelden maakt ze geschikt voor vele technische toepassingen. Een voorbeeld is het magnetisch terugwinnen van katalysatoren zoals beschreven in hoofdstuk 4. Een katalysator is vastgezet aan het oppervlak van magnetische silicadeeltjes. Zonder magneetveld blijven de katalytische deeltjes gedispergeerd in het reactiemengsel, wat belangrijk is voor een effectieve katalyse. De deeltjes, en daardoor ook de katalysator, kunnen dankzij hun sterke magnetiseerbaarheid makkelijk gescheiden worden van het reactiemengsel met een magneet. Silicacolloïden waarin zich maghemietdeeltjes bevinden worden hier gebruikt omdat met maghemiet het geïnduceerde dipoolmoment van de composietdeeltjes verdwijnt als de magneet wordt verwijderd. Op deze manier kunnen de deeltjes opnieuw gedispergeerd worden voor hergebruik van de katalysator.

In hoofdstuk 5 worden de magnetische eigenschappen van de magnetische silicadeeltjes grondig bestudeerd op basis van metingen van de complexe magnetische susceptibiliteit als functie van zowel frequentie als amplitude. In dit hoofdstuk wordt aangetoond dat silicadeeltjes waarin zich cobaltferriet nanodeeltjes bevinden een permanent magnetisch dipoolmoment bezitten. Dit blijkt uit susceptibiliteitsspectra gemeten aan magnetische silicadeeltjes dispergeerd in ethanol, waarin de karakteristieke frequentie overeenkomt met de Brownse rotatiebeweging van de microdeeltjes. In een vergelijkbaar spectrum van silicadeeltjes met maghemiet wordt alleen maar de contributie van Nel relaxatie in de nanodeeltjes teruggevonden. Besproken wordt dat het permanent magnetisch moment van de microdeeltjes met cobaltferriet ook aanwezig zou zijn indien de nanodipolen willekeurig georinteerd waren. Dit komt omdat de vectorsom van willekeurig georinteerde eenheidsvectoren niet nul is. Een toename van het permanent magnetisch moment van de microdeeltjes werd gemeten nadat de deeltjes waren blootgesteld aan een sterk magneetveld. Nadat het veld is verwijderd relaxeert een groot deel van de nanodipolen niet naar willekeurige orintaties, maar naar de dichtstbijzijnde kristallografische voorkeursassen. De mogelijkheid om de dipoolmomenten van de microdeeltjes kwantitatief te bepalen biedt ook de mogelijkheid om de maximale interactie-energie tussen de microdeeltjes in te schatten. Voor de hier bestudeerde microdeeltjes ligt deze interactie-energie tussen 0.5 1 $k_B T$.

In hoofdstuk 6 worden frequentieafhankelijke complexe magnetische susceptibiliteitsspectra gemeten van dispersies van silicabollen met ingesloten cobaltferriet als een functie van de colloïdale concentratie. Op deze manier wordt de zo goed als diffusieve rotatie van dipolaire deeltjes bestudeerd. In vergelijking met optische meetmethoden, die vaak gebruikt worden om rotatiediffusie te meten, is het voordeel van een magnetische meetmethode dat deze ongevoelig is voor meervoudige verstrooiing of absorptie van licht. Dit biedt de mogelijkheid om de rotatie van deeltjes met een attractieve interactiepotentiaal te onderzoeken.

In hoofdstuk 7, tenslotte, worden de resultaten gepresenteerd van statische lichtverstrooiingsmetingen aan magnetische silicadeeltjes waarbij het optische contrast gevarieerd wordt door het oplosmiddel te veranderen. Hier is onderzocht in hoeverre de theorie voor statische lichtverstrooiing van optisch inhomogene deeltjes in de Rayleigh-Gans-Debye benadering toegepast kan worden op bolvormige composietdeeltjes met een kern en twee concentrische schillen, waarvan n schil magnetische nanodeeltjes bevat met een hoge brekingsindex. Alhoewel deze theorie niet het volledige verstrooiingspatroon verklaart, zien we dat de verstrooiingscurven gemeten bij de verschillende optische contrasten elkaar kruisen. De deeltjesstraal berekend aan de hand van dit kruispunt komt overeen met de straal gemeten met elektronenmicroscopie.

Curriculum Vitae

Maria Claesson was born on 3 January, 1978 in Mölndal, next to Gothenburg , Sweden. In 1997, she graduated from the Chemistry Science Program at Erik Dahlbergs Gymnasiet in Jönköping. Thereafter she studied chemistry at Lund University from which she obtained her MSc (fil. mag.) degree in 2002. In the final year of her studies she performed her master research project at the Van 't Hoff Laboratory for Physical and Colloid Chemistry at Utrecht University, The Netherlands, under supervision of Dr. Roel Dullens and Prof. Dr. Willem Kegel. This research resulted in a master's thesis entitled: "Study of Swollen, Crosslinked PMMA-particles in Good Solvents". During the summer breaks from the university, she worked as a researcher at the pharmaceutical company AstraZeneca in Lund. After her studies, she continued as a PhD-student at the Van 't Hoff Laboratory under supervision of Prof. Dr. Albert Philipse and Dr. Ben Erné. Her research on synthesis and characterization of magnetic core-shell colloids described in this thesis, was financially supported by OCÉ Technologies BV in Venlo, The Netherlands.

List of Publications

This thesis is based on the following papers:

E. M. Claesson and A.P. Philipse. Monodisperse magnetizable composite silica spheres with tunable dipolar interactions. *Langmuir*, 21:9412–9419, 2005. (Chapter 2)

E. M. Claesson and A. P. Philipse. Thiol-functionalized silica colloids, grains, and membranes for irreversible adsorption of metal(oxide) nanoparticles. *Colloids Surf., A*, 297:46–54 2007. (Chapter 3)

E. M. Claesson, N. C. Mehendale, R. J. M. Klein Gebbink, G. van Koten and A. P. Philipse. Magnetic Silica Colloids for Catalysis. *J. Magn. Magn. Mater.*, 311:41–45. (Chapter 4)

E. M. Claesson, B. H. Erné, I. A. Bakelaar, B. W. M. Kuipers and A. P. Philipse. Measurement of the Zero-Field Magnetic Dipole Moment of Magnetizable Colloidal Silica Spheres. *J. Phys.: Condens. Matter*, 19:036105 (16pp), 2007. (Chapter 5)

E. M. Claesson, B. H. Erné, I. A. Bakelaar, B. W. M. Kuipers and A. P. Philipse. Rotational Dynamics of Magnetic Silica Spheres Studied with Complex Magnetic Susceptibility Measurements *J. Phys.: Condens. Matter*, In Press, 2007. (Chapter 6)

E. M. Claesson and A.P. Philipse. Light Scattering from Silica-Iron Oxide Core-Shell Colloids. Manuscript in preparation (Chapter 7)

Other papers by the author:

B. H. Erné, E. M. Claesson, S. Sacanna, M. Klokkenburg, I. A. Bakelaar, and B. W. M. Kuipers. Low-frequency complex magnetic susceptibility of magnetic composite microspheres in colloidal dispersion. *J. Magn. Magn. Mater.*, 311:145–149, 2007.

M. Klokkenburg, C. Vonk, E. M. Claesson, J. D. Meeldijk, B. H. Erné, and A. P. Philipse. Direct imaging of zero-field dipolar structures in colloidal dispersions of synthetic magnetite. *J. Am. Chem. Soc.*, 126:16706–16707, 2004.

R. P. A. Dullens, M. Claesson, D. Derks, A. van Blaaderen, and W. Kegel. Monodisperse core-shell poly(methyl methacrylate) latex colloids. *Langmuir*, 19:5963 – 5966, 2003.

R. P. A. Dullens, M. Claesson, and W. Kegel. Preparation and properties of crosslinked fluorescent poly(methyl methacrylate) latex colloids. *Langmuir*, 20:658–664, 2004.